Schweizerische Eidgenossenschaft
Confédération suisse
Confederazione Svizzera
Confederaziun svizra

Federal Department of the Environment,
Transport, Energy and Communications DETEC

Swiss Federal Office of Energy
Energy Research and Cleantech

Interim report from 5 June 2026

BEACH

Bedretto Energy Storage and Circulation of Geothermal Energy

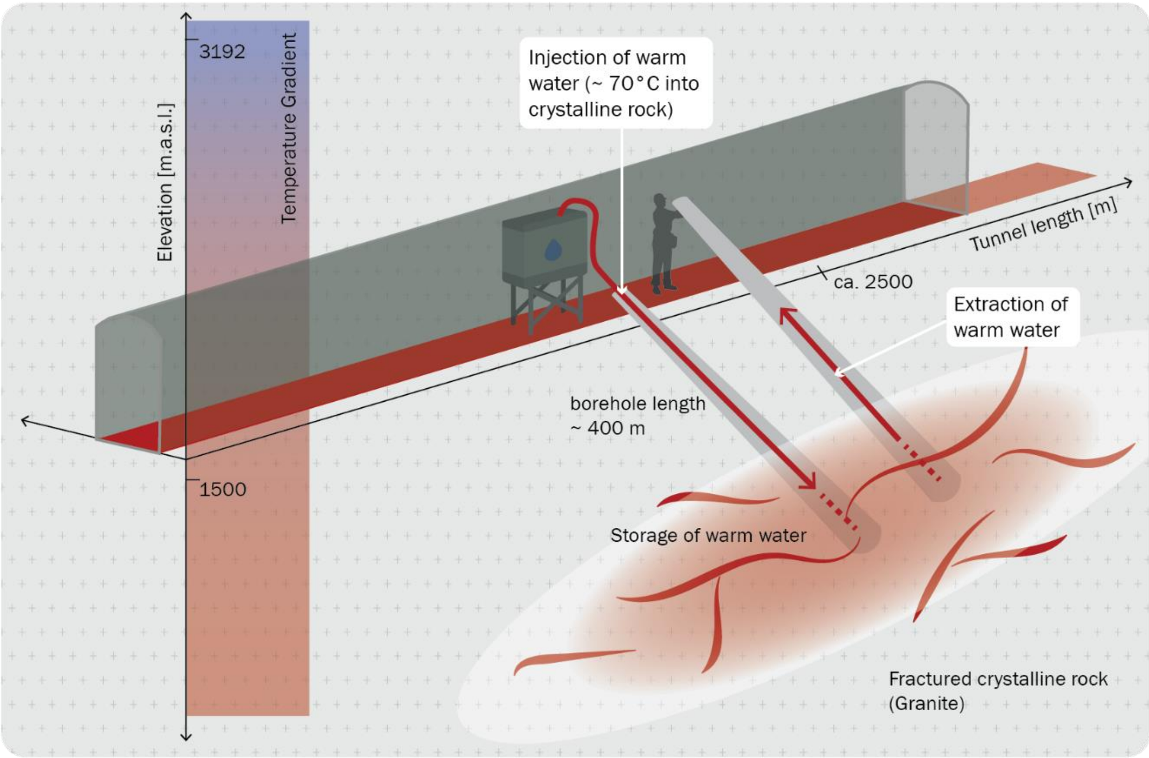

Publisher:
Swiss Federal Office of Energy SFOE
Energy Research and Cleantech
CH-3003 Berne
www.energy-research.ch

Subsidy recipients:
SUPSI
Scuola universitaria professionale della Svizzera italiana
Le Gerre, Via Pobiette 11
6928 Manno

GeoEnergie Suisse
Reitergasse 11
8004 Zürich

AET - Azienda Elettrica Ticinese
El Stradún 74
6513 Monte Carasso

Authors:

Valentin Gischig (valentin.gischig@eaps.ethz.ch), Marian Hertrich, Bruce Gee, Frédéric Massin, Liliana Vargas Meleza, Fridolin Staub, Alexandra Lightfoot, Beatrix Heinze, Hansruedi Maurer, Federica Lanza, Stefanie Zeller, ETH Zurich

Francisco Serbeto (f.serbeto@geo-energie.ch), Andres Alcolea, Peter Meier, Geo-Energie Suisse AG (GES)

Filippo Schenker (Filippo.Schenker@supsi.ch), Alessia Grignaschi, Simone Zavattoni, Giovanni Cutuli, Marco Belliardi, Maurizio Barbato, Scuola universitaria professionale della Svizzera italiana (SUPSI)

Nadine Haaf, Jerome Azzola, Karlsruher Institut für Technologie (KIT)

SFOE project coordinators:
Prof. Martin O. Saar, Prof. Hansruedi Maurer, saarm@ethz.ch
Filippo Schenker, Filippo.Schenker@supsi.ch
Peter Meier, p.meier@geo-energie.ch
Edy Losa, edy.losa@aet.ch

SFOE contract number: SI/502817-01

Summary

In the BEACH project, we address key challenges of the Swiss energy transition with demonstrating a novel subsurface energy storage technology: Fractured Thermal Energy Storage (FTES). This concept offers a potential solution for balancing seasonal mismatches between energy supply and demand, by storing excess, low-cost thermal energy during summer and recovering it as heat (or potentially electricity) during winter. The utilization of fractured crystalline reservoirs is particularly relevant for Switzerland, where large portions of the subsurface, especially in the Alpine region, include such formations at relatively shallow depths.

The objectives of the project are threefold: (1) to assess the techno-economic feasibility of the FTES concept (Phase I), (2) to experimentally evaluate the concept in a single borehole configuration and to confirm the techno-economic feasibility of FTES (Phase II), and (3) to investigate the performance of a cross-hole circulation system (Phase III) at the BedrettoLab in a scaled manner. The overarching objective is to address potential implementation scenarios and roll-out of the FTES for different cases, e.g. in Ticino.

In this document, we report the results of Phase II, including (1) experimental observations from single-borehole heat storage tests, (2) numerical models that reproduce the observed behaviour and extrapolate to different potentially more efficient operating conditions, and (3) the conceptual design of cross-hole experiments for Phase III.

The conducted heat storage experiment represents a downscaled analogue of ideal operational conditions, which would typically involve injection rates on the order of more than 100 L/min at temperatures of more than 60°C to achieve depth-dependent storage efficiencies of approximately 70% (see outcomes of Phase I). In the BedrettoLab, we injected water at 70°C at a constant flow rate of 12 L/min into an 18 m-long interval located between 132 and 150 m depth in a borehole equipped with a multi-packer system. Hot water injection was performed over two cycles, each exceeding two weeks in duration each, during which pressures reached up to 16 MPa. Each injection cycle was followed by a shut-in period (resting phase) and a production phase, during which flow rates of 3 L/min were achieved under atmospheric pressure conditions by opening the interval. Monitoring activities included pressure and deformation measurements in adjacent boreholes, noble gas analysis, high-resolution geochemical and microbiological sampling, as well as seismic monitoring integrated with an adaptive traffic-light system for seismic risk management.

In this first experiment, the borehole was not thermally insulated above the injection interval, leading to significant thermal losses along the wellbore prior to reaching the target zone. As a result, thermal recovery efficiencies at the interval level were limited to 6 and 10% for the first and second injection cycles, respectively. Importantly, despite this a prior known non-ideal insulation and the relatively short injection duration (2 weeks per cycle only), the second cycle exhibits a clear increase in thermal recovery compared to the first. This trend is consistent with the expected behaviour of FTES (and, in broad sense, underground thermal energy storage, UTES), in which storage efficiency improves progressively with repeated load–unload cycles as the reservoir thermal regime stabilizes. These results therefore provide encouraging evidence that performance gains can be achieved even under unfavourable design conditions and strongly suggest that substantially higher efficiencies are attainable with improved wellbore insulation and a more realistic longer-term cyclic operation. Ongoing work focuses on implementing these design improvements and extending the number of injection cycles to fully realize the storage potential of the system. The next phase, Phase III, will go ahead with a cross-hole heat storage configuration, for which an additional injection/production borehole is drilled and the monitoring is expanded to record the relevant parameters to further optimize the FTES concept.

Zusammenfassung

Im Rahmen des BEACH-Projekts gehen wir zentrale Herausforderungen der Schweizer Energiewende an, indem wir eine neuartige Technologie zur unterirdischen Energiespeicherung demonstrieren: die Fractured Thermal Energy Storage (FTES). Dieses Konzept bietet eine mögliche Lösung für den Ausgleich saisonaler Ungleichgewichte zwischen Energieangebot und -nachfrage, indem im Sommer überschüssige, kostengünstige Wärmeenergie gespeichert und im Winter als Wärme (oder potenziell als Strom) wiedergewonnen wird. Die Nutzung von kristallinen Reservoirs mit Rissstruktur ist für die Schweiz besonders relevant, da grosse Gebiete im Alpenraum solche Formationen in relativ geringer Tiefe aufweisen.

Das Projekt verfolgt drei Ziele: (1) die techno-ökonomische Machbarkeit des FTES-Konzepts zu bewerten (Phase I), (2) das Konzept in einer Einzelbohrloch-Konfiguration experimentell zu evaluieren (Phase II) und (3) die Leistungsfähigkeit eines Cross-Hole-Zirkulationssystems (Phase III) im Massstab des BedrettoLabs zu untersuchen. Das übergeordnete Ziel besteht darin, potenzielle Umsetzungsszenarien und die Einführung des FTES für verschiedene Anwendungsfälle, z. B. im Tessin, zu untersuchen.

In diesem Dokument tragen wir die Ergebnisse von Phase II zusammen, darunter (1) experimentelle Beobachtungen aus Wärmespeichertests mit einem einzelnen Bohrloch, (2) numerische Modelle, die das beobachtete Verhalten nachbilden und auf verschiedene potenziell effizientere Betriebsbedingungen extrapolieren, sowie (3) den konzeptionellen Entwurf von Cross-Hole-Experimenten für Phase III.

Das durchgeführte Wärmespeicher-Experiment stellt ein verkleinertes Modell idealer Betriebsbedingungen dar, die typischerweise Injektionsraten in der Grössenordnung von mehr als 100 l/min bei Temperaturen von über 60 °C beinhalten würden, um Speichereffizienzen von etwa 70 % zu erreichen (siehe Ergebnisse von Phase I). Im BedrettoLab injizierten wir Wasser mit einer Temperatur von 70 °C bei einer konstanten Durchflussrate von 12 l/min in einen 18 m langen Intervall in einer Tiefe zwischen 132 und 150 m in einem mit einem Multi-Packer-System ausgestatteten Bohrloch. Die Heisswasser-Injektionen erfolgten in zwei Zyklen von jeweils mehr als zwei Wochen Dauer, in denen Drücke von bis zu 16 MPa erreicht wurden. Auf jeden Injektionszyklus folgte eine Abschaltphase (Ruhephase) und eine Produktionsphase, in der durch Öffnen des Intervalls Durchflussraten von 3 l/min unter atmosphärischen Druckbedingungen erzielt wurden. Zum Überwachungskonzept gehörten Druck- und Verformungsmessungen in benachbarten Bohrlöchern, Edelgasanalysen, hochauflösende geochemische und mikrobiologische Probenahmen sowie seismische Überwachung, integriert in ein adaptives Ampelsystem als Teil des seismischen Risikomanagements.

In diesem ersten Experiment war das Bohrloch oberhalb des Injektionsintervalls nicht thermisch isoliert, was zu erheblichen Wärmeverlusten entlang des Bohrlochs führte, bevor die Zielzone erreicht wurde. Infolgedessen beschränkten sich die thermischen Rückgewinnungswirkungsgrade auf Intervallebene im ersten und zweiten Injektionszyklus auf 6 bzw. 10 %. Wichtig ist, dass trotz dieser bereits im Voraus bekannten nicht idealen Isolierung und der relativ kurzen Injektionsdauer (nur 2 Wochen pro Zyklus) der zweite Zyklus im Vergleich zum ersten eine deutliche Steigerung der thermischen Rückgewinnung aufweist.

Dieser Trend steht im Einklang mit dem erwarteten Verhalten von FTES (und im weiteren Sinne von unterirdischen Wärmespeichern), bei denen sich die Speichereffizienz mit wiederholten Lade- und Entladezyklen zunehmend verbessert, während sich das thermische Regime des Reservoirs stabilisiert. Diese Ergebnisse liefern daher ermutigende Hinweise darauf, dass Leistungssteigerungen auch unter ungünstigen Bedingungen erzielt werden können. Sie legen zudem nahe, dass mit einer verbesserten Bohrlochisolierung und einem realistischeren, längerfristigen zyklischen Betrieb wesentlich höhere Wirkungsgrade erreichbar sind. Die laufenden Arbeiten konzentrieren sich auf die Umsetzung dieser Systemverbesserungen und die Ausweitung der Anzahl der Einspeisezyklen, um das Speicherpotenzial des Systems voll auszuschöpfen. In der nächsten Phase, Phase III, wird eine Konfiguration mit querverlaufenden Wärmespeicherbohrungen umgesetzt, bei der ein zusätzliches Einspeise-/Förderbohrloch gebohrt und die Überwachung erweitert wird, um die relevanten Parameter aufzuzeichnen und das FTES-Konzept weiter zu optimieren.

Résumé

Dans le cadre du projet BEACH, nous relevons les principaux défis de la transition énergétique suisse en faisant la démonstration d'une technologie innovante de stockage souterrain de l'énergie : le stockage thermique par fracturation (FTES). Ce concept offre une solution potentielle pour compenser les déséquilibres saisonniers entre l'offre et la demande d'énergie, en stockant l'énergie thermique excédentaire et peu coûteuse en été pour la récupérer sous forme de chaleur (ou potentiellement d'électricité) en hiver. L'utilisation de réservoirs cristallins présentant une structure fissurée est particulièrement pertinente pour la Suisse, car de vastes zones de la région alpine possèdent de telles formations à une profondeur relativement faible.

Le projet poursuit trois objectifs : (1) évaluer la faisabilité technico-économique du concept FTES (phase I), (2) évaluer expérimentalement le concept dans une configuration à puits unique (phase II) et (3) étudier les performances d'un système de circulation inter-puits (phase III) à l'échelle du BedrettoLab. L'objectif global consiste à étudier les scénarios de mise en œuvre potentiels et l'introduction du FTES pour différents cas d'application, par exemple au Tessin.

Dans ce document, nous rassemblons les résultats de la phase II, notamment (1) les observations expérimentales issues des essais de stockage de chaleur avec un seul forage, (2) les modèles numériques qui reproduisent le comportement observé et l'extrapolent à différentes conditions d'exploitation potentiellement plus efficaces, ainsi que (3) la conception des expériences inter-forages pour la phase III.

L'expérience de stockage thermique réalisée constitue un modèle à échelle réduite des conditions d'exploitation idéales, qui impliqueraient généralement des débits d'injection de l'ordre de 100 l/min et plus à des températures supérieures à 60 °C afin d'atteindre des rendements de stockage d'environ 70 % (voir les résultats de la phase I). Au BedrettoLab, nous avons injecté de l'eau à une température de 70 °C à un débit constant de 12 l/min dans un intervalle de 18 m de long, à une profondeur comprise entre 132 et 150 m, dans un forage équipé d'un système Multi-Packer. L'injection de l'eau chaude s'est déroulée en deux cycles d'une durée de plus de deux semaines chacun, au cours desquels des pressions allant jusqu'à 16 MPa ont été atteintes. Chaque cycle d'injection a été suivi d'une phase d'arrêt (phase de repos) et d'une phase de production, durant laquelle des débits de 3 l/min ont été obtenus dans des conditions de pression atmosphérique grâce à l'ouverture de l'intervalle. Le concept de surveillance comprenait des mesures de pression et de déformation dans des puits voisins, des analyses de gaz rares, des prélèvements géochimiques et microbiologiques à haute résolution ainsi qu'une surveillance sismique, intégrée dans un système de feux tricolores adaptatif dans le cadre de la gestion des risques sismiques.

Dans cette première expérience, le puits n'était pas isolé thermiquement au-dessus de l'intervalle d'injection, ce qui a entraîné des pertes de chaleur considérables le long du puits avant que la zone cible ne soit atteinte. En conséquence, les rendements de récupération thermique au niveau de l'intervalle se sont limités à 6 % et 10 % respectivement lors des premier et deuxièmes cycles d'injection.

Il est important de noter que, malgré cette isolation non optimale connue d'avance et la durée d'injection relativement courte (seulement 2 semaines par cycle), le deuxième cycle présente une augmentation significative de la récupération thermique par rapport au premier.

Cette tendance est conforme au comportement attendu des FTES (et, plus largement, des accumulateurs de chaleur souterrains), dans lesquels l'efficacité de stockage s'améliore progressivement au fil des cycles répétés de charge et de décharge, tandis que le régime thermique du réservoir se stabilise. Ces résultats fournissent donc des indications encourageantes quant à la possibilité d'obtenir des gains de performance même dans des conditions défavorables. Ils suggèrent en outre qu'avec une meilleure isolation des puits et un fonctionnement cyclique plus réaliste et à plus long terme, des rendements nettement supérieurs peuvent être atteints. Les travaux en cours se concentrent sur la mise en œuvre de ces améliorations du système et l'augmentation du nombre de cycles d'injection afin d'exploiter pleinement le potentiel de stockage du système. Au cours de la phase suivante, la phase III, une configuration avec des puits de stockage de chaleur transversaux sera mise en œuvre : un puits d'injection/extraction supplémentaire sera foré et la surveillance sera étendue afin d'enregistrer les paramètres pertinents et d'optimiser davantage le concept FTES.

Inhaltsverzeichnis

List of figures

List of tables

List of abbreviations

SFOE	Swiss Federal Office of Energy
BEACH	Bedretto Energy Storage and Circulation of Geothermal Energy
FTES	Fractured Thermal Energy Storage
GTB	Geothermal Test Bed
CapEx	Capital Expenditures
OpwEx	Operating Expenses
GES	Geo-Energie Suisse AG
DAS	Distributed Acoustic Sensing
DSS	Distributed Strain Sensing
DTS	Distributed Temperature Sensing
FO	Fiber Optics
FBG	Fiber Bragg grating
CTPP	Cementable Tube Pore Pressure

1 Introduction

1.1. Context and motivation

The primary objective of the BEACH project is to demonstrate the feasibility, and to define the technical requirements for energy storage in fractured crystalline rocks through Fractured Thermal Energy Storage (FTES). This emerging technology holds significant potential to support the Swiss energy transition (Figure 1). Achieving the Swiss Federal Council's net-zero emissions target by 2050 (SFOE, 2021) will require not only the expansion of existing renewable energy sources, but also the deployment of new, enabling technologies. In this context, energy storage is an increasingly important topic in times of energy excess during certain periods and energy shortage during other periods (Energy Perspectives 2050+).

Seasonal subsurface heat storage in suitable geological formations at shallow, intermediate and greater depths offers a promising solution to address the intermittency of energy production. So far, in Switzerland, potential heat storage formations have primarily been identified in sedimentary formations of the Molasse Basin (e.g. Forsthaus in Bern, Link et al., 2020) and in unconsolidated gravel deposits within glacially overdeepened troughs (e.g. Flughafen, Zürich, Ebert and Sutter, 2023). Storage in fractured crystalline rocks, has been so far largely unexplored in experimental studies, although they constitute a large fraction of Switzerland's subsurface (especially in Alpine regions). Their potential has been discussed in recent literature (Hibbard et al., 2026, Gholizadeh et al., 2024), but most investigations of FTES systems are still limited to conceptual and numerical analyses, focusing on aspects such as fracture geometry, fracture–matrix interaction, storage capacity, and thermal breakthrough risks (De La Bernardie et al., 2018; Klepikova et al., 2021; Zhou et al., 2022; Knobloch et al., 2022).

Although the results of these conceptual studies are encouraging, a critical gap remains between theoretical potential and practical implementation. There is a clear need to (1) further quantify the physical feasibility of energy storage in fractured crystalline rocks, (2) to assess the associated economic constraints, and, most importantly, (3) to demonstrate the practical feasibility of a FTES under real field conditions.

The BEACH project directly addresses this gap by providing a comprehensive, experimentally grounded assessment of FTES. Its overarching goal is to answer the key question: **how can heat storage in fractured crystalline rocks contribute to achieving Switzerland's net-zero energy transition?**

Within the BEACH pilot and demonstration project, the possibilities to store heat in fractured crystalline rocks are investigated in three incrementally complex phases, each defined by clear and measurable objectives. In **Phase I**, numerical and conceptual studies were conducted to assess the techno-economical feasibility of FTES, including the conceptual design of the first experiments to be carried out at the BedrettoLab. **Phase II** has focused on the execution of first field experiments in a single-borehole configuration, while **Phase III** aims to extend the concept to a two-borehole system to evaluate the efficiency of heat storage under cross-hole circulation conditions. Here, we focus primarily on the results of Phase II.

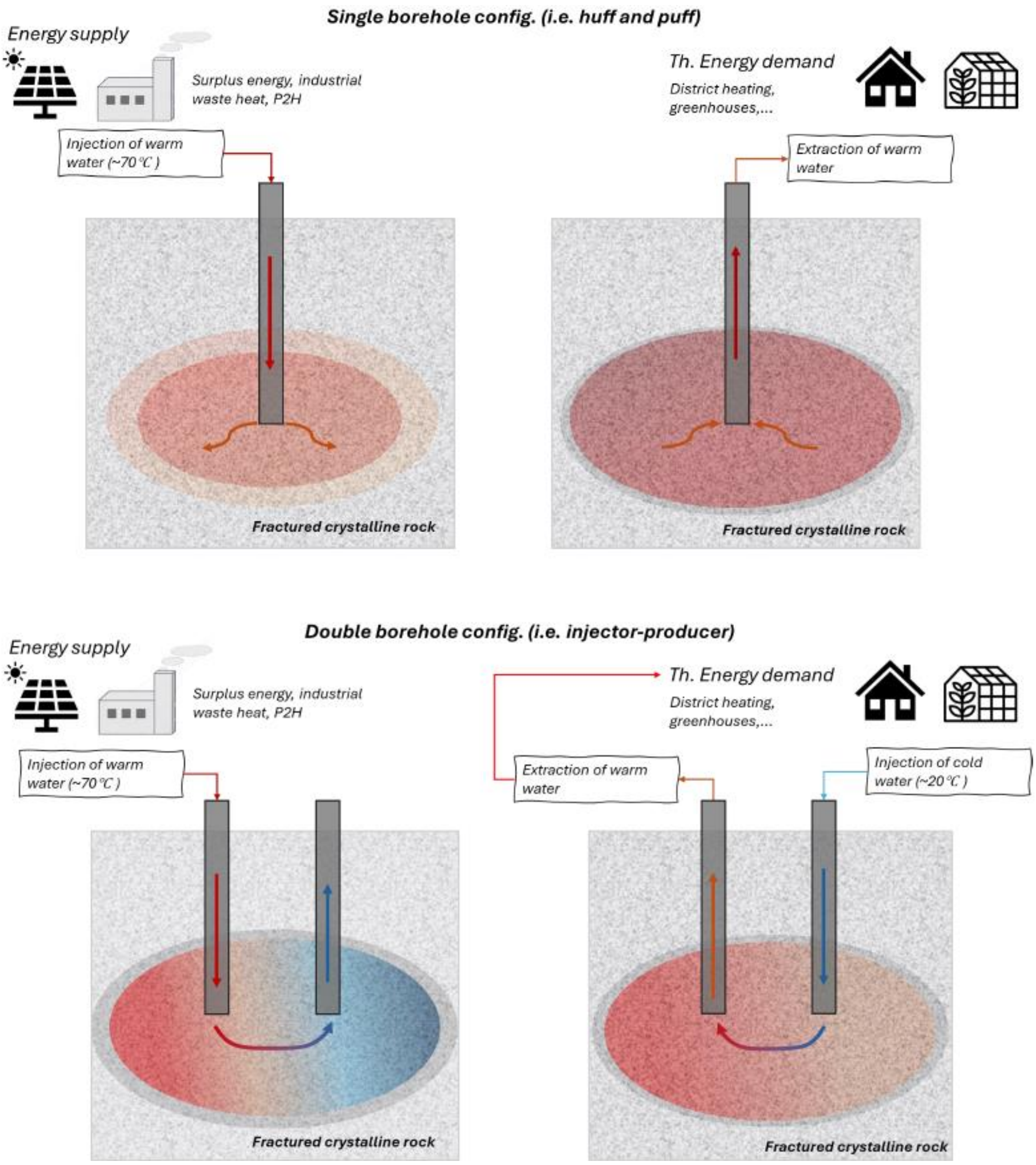

Figure 1: Conceptual illustration of subsurface thermal energy storage using single-borehole and doublet configurations: injection of excess heat during summer (left) and recovery for district heating during winter (right).

The project is structured into four interconnected work packages (WPs), which build sequentially upon each other while continuously exchanging data, information, and predictive scenarios to support the real-scale tests and implementation. **WP1** addresses the overall feasibility of the FTES concept through numerical simulations and reservoir-scale modelling, providing process understanding before, during, and after operations. **WP2** translates these insights into detailed experimental designs, including infrastructure planning and test preparation. **WP3** entails the execution of the real-scale experimental activities at the BedrettoLab including preparational work, onsite engineering, and comprehensive monitoring activities. Finally, **WP4** focuses on scaling up the technology, integrating FTES into the cantonal and national energy strategies, and developing future deployment scenarios.

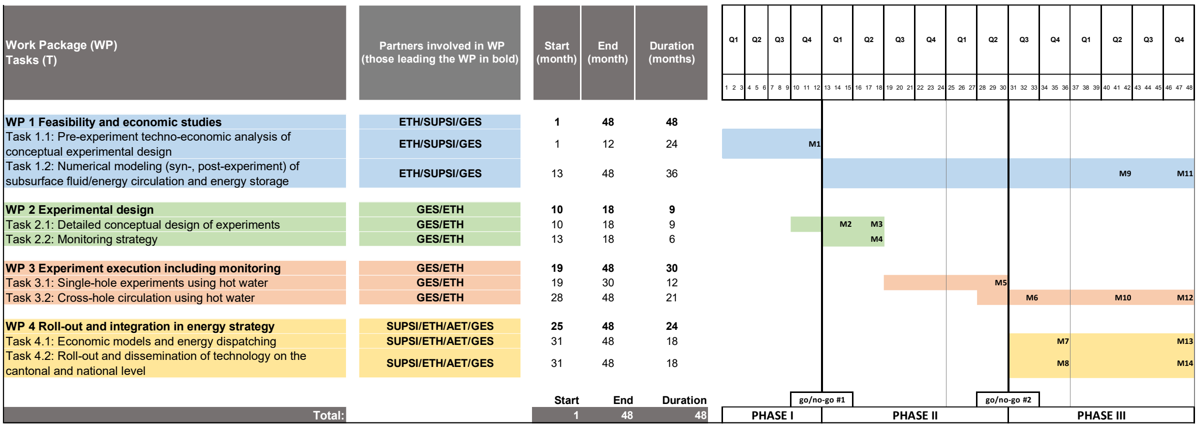

Figure 2: Organizational structure of the BEACH project, illustrating the four work packages across the three project phases.

This report presents primarily the outcomes of **Phase II**, which focuses on the experimental evaluation of the FTES concept in a single-borehole configuration. This includes the design and execution of experiments within the existing borehole infrastructure of the Geoenergy testbed (GTB) at the BedrettoLab, as well as the development of a comprehensive monitoring strategy, with particular emphasis on seismic monitoring and hazard management. In addition, we provide a short review of the **Phase I** results and discuss possible ramifications for **Phase III**.

The main questions addressed in **Phase II** are as follows.

1. How does reservoir behaviour under real-scale experimental conditions compare to model predictions?
2. What monitoring strategy enables safe, efficient, and sustainable operation of a FTES?

To address these questions, the following tasks were carried out.

- Demonstrating the technical feasibility of heat storage within the fractured Bedretto reservoir.
- Developing and implementing a monitoring framework that ensures safe and efficient reservoir utilization.
- Validating that the observed hydraulic, thermal, and storage behaviour of the reservoir is consistent with numerical model predictions.
- Using calibrated models to show how heat storage efficiencies can be improved through optimized injection–production strategies, both at the BedrettoLab and in comparable geological settings across Switzerland.

In preparation for **Phase III** of the project which will investigate cross-hole heat storage configurations, we further evaluate a range of technical concepts and economic scenarios, including options such as the remediation of existing boreholes (e.g. ST2) or the drilling of new boreholes for injection and production operations.

The remainder of this report is structured as follows. Section 2 summarizes the **Phase I** results relevant to the experimental design of **Phase II.** Section 3 describes the single-borehole heat storage experiment conducted at the BedrettoLab. Section 4 presents the numerical modelling based on experimental observations. Section 5 evaluates concepts for cross-hole configurations. Finally, section 6 outlines the current status and future outlook for FTES deployment.

2 Summary of Phase I

Phase I focused on generic numerical modelling, techno-economic assessment of the FTES concept, and the design of the experimental planning for hot water injection experiments at the BedrettoLab. Overall, the results of **Phase I** demonstrated that FTES is both technically feasible and potentially scalable in Switzerland, thereby offering a promising solution for storing surplus energy and mitigating seasonal imbalances in energy supply (see Brehme et al., 2025, for a more detailed account of **Phase I** results).

Simulation results indicated that FTES systems can achieve thermal recovery efficiencies exceeding 70% under realistic operating conditions, such as injection temperatures of approximately 60°C and flow rates on the order of 200 L/min. Sensitivity analyses identified fracture permeability, fracture porosity, and matrix porosity as the most influential parameters controlling storage efficiency. Importantly, the modelling exercises also showed that storage efficiency increases progressively over time with repeated injection–production cycles, as the surrounding rock mass undergoes gradual warming.

The techno-economic analysis suggests that financial viability is strongly governed by operational scale, particularly mass flow rate, well configuration, and energy pricing conditions. While **small-scale systems are unlikely to be economically competitive**, larger installations involving flow rates above approximately **13 L/s (780 L/min) distributed across multiple wells could achieve positive financial returns**, with estimated payback periods on the order of 12 years under favourable market scenarios.

Building on these findings, a first downscaled field experiment was designed for implementation at the BedrettoLab, in which heated water is injected into a fractured reservoir, and subsequently recovered to demonstrate practical heat storage and extraction under controlled conditions. A specific 18 m-long borehole interval (Interval 11) was selected as a test section. This was based on its fracture network characteristics, transmissivity, depth, and relatively low seismic activity. The experimental design incorporated comprehensive monitoring of temperature, pressure, flow rates, and seismicity, enabling direct validation of numerical models and iterative refinement of system design.

Beyond the site-specific case at the BedrettoLab, **Phase I** also evaluated the broader deployment potential of FTES across Switzerland, including case studies such as Vallemaggia, Uvrier, Schaffhausen, and an industrial site in northern Switzerland. These assessments highlighted the potential for integrating FTES systems with industrial waste-heat sources, waste incineration facilities, and district heating networks, thereby enabling the seasonal storage and redistribution of excess thermal energy.

3 Phase II: Heat storage experiments

3.1. Experiment setup

3.1.1. Injection borehole ST1

The target borehole for the single-borehole experiment of Phase II is the 405 m-long borehole ST1 within the Geoenergy testbed at the BedrettoLab. This borehole is equipped with a permanent multi-packer system that hydraulically isolates 14 intervals of varying lengths (Figure 3 and Figure 4). Each interval is separated by 1.5 m-long packers and can be accessed individually with sliding-sleeves, and hosts a downhole pressure and temperature sensor as well as distributed temperature sensing (DTS) cables along the borehole, enabling high-resolution monitoring of ongoing THM processes.

Based on structural characteristics and prior hydraulic stimulation experiments across all intervals, Interval 11 was selected as the optimum test section, for it represents the best compromise between hydraulic, geological, and operational constraints. The selection is supported by the following key factors:

1) The fracture network tapped by Interval 11 is relatively simple and dominated by a limited number of conductive fractures, which enhances the likelihood of recovering injected thermal fluids. In contrast, more complex fracture systems would promote fluid dispersion into multiple pathways, increasing mixing and reducing thermal recovery efficiency.
2) Interval 11 has been extensively characterized through multiple hydraulic stimulation campaigns, including the MzeroA experiment, which generated a well-defined seismicity cloud that clearly delineates the fracture network actively flowing fracture network. As a result, the reservoir response to injection is exceptionally well constrained by a rich monitoring dataset (e.g. Gischig et al. (2026), under review).
3) Interval 11 exhibits moderate but sufficient transmissivity, allowing efficient injection and recovery while maintaining controlled flow conditions. Lower-transmissivity intervals (e.g. 12 and 14) were excluded due to flow limitations, whereas highly transmissive intervals (e.g. 13) were avoided to reduce the risk of rapid thermal dissipation into the far field.
4) Its location at **intermediate depth (132–150 m)** ensures optimal coverage within the existing dense monitoring network, while also providing a favourable balance between thermal losses and operational efficiency, both of which tend to increase dramatically with depth.

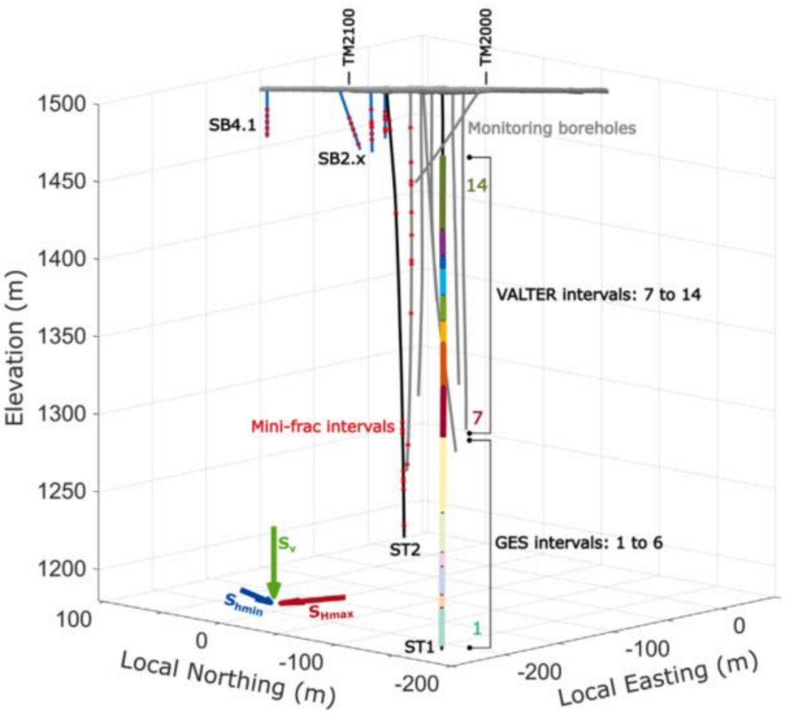

Figure 3: Layout of stimulation (ST), monitoring (in grey) and stress measurement (SB) boreholes within the Bedretto Geoenergy testbed. The 14 stimulation intervals along ST1 are coloured (after Bröker et al.,2024).

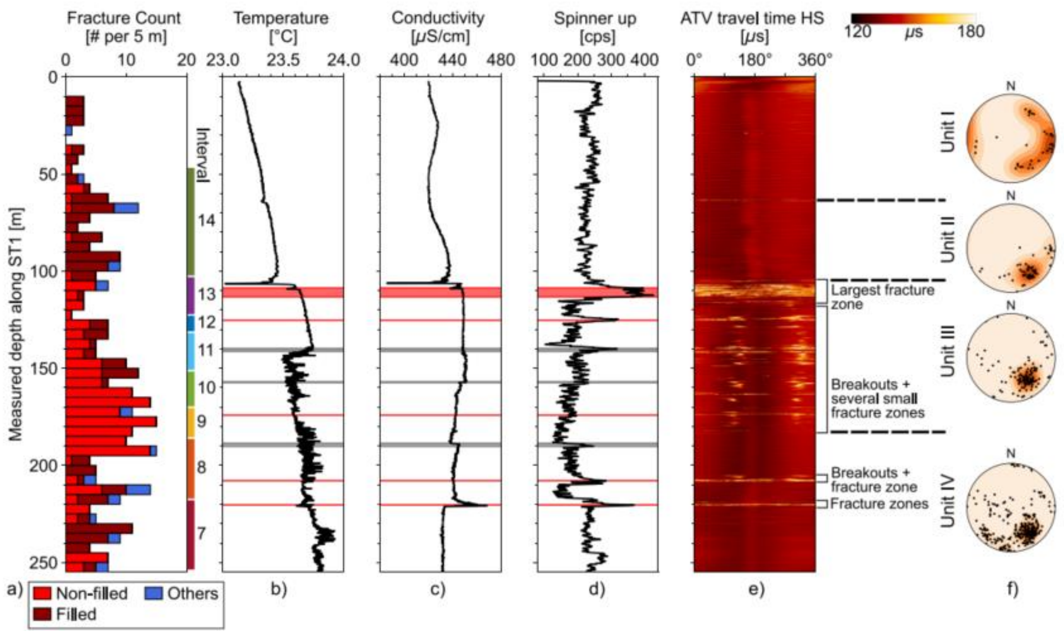

Figure 4: Integrated geophysical logs along the shallow section of ST1 (the deeper GES intervals 1 to 6 are not shown): (a) structural interpretation from televiewer logs and the extent of the stimulated intervals, (b) temperature, (c) electrical conductivity, (d) spinner flow log, (e) acoustic televiewer travel time (oriented to high side), (f) lower hemisphere pole plots with density contours of geological discontinuities. Fracture zones with widths greater than 10 cm are shown as red bands, and other identified inflow zones are shown as gray bands. The true aperture of fracture zones is shown. After Bröker et al., (2024).

Interval 11 is located between 132.2 m and 150.5 m depth, corresponding to a length of about 18.3 m. It intersects multiple open fractures, including two main fracture zones with an orientation of approximately 233°/58° (Figure 5). Geophysical logging identifies a conductive feature near 142 m depth, where increased temperature and inflow signatures were observed. This hydraulically active fracture can effectively transmit fluid, making the interval particularly suitable for injection and recovery experiments.

The initial static pressure at Interval 11 is approximately 3.6 MPa, and its transmissivity was initially estimated at about 4×10^{-8} m²/s (moderate transmissivity compared to other intervals). Following multiple hydraulic stimulation campaigns, including the Mzero experiment (Gischig et al., under review), the transmissivity increased to about 1×10^{-6} m²/s, reflecting significant injection-induced permeability enhancement. Cumulative injection volumes of up to 147 m³ of water during these stimulations generated an extensive seismicity cloud, which effectively maps the preferential flow pathways within the reservoir.

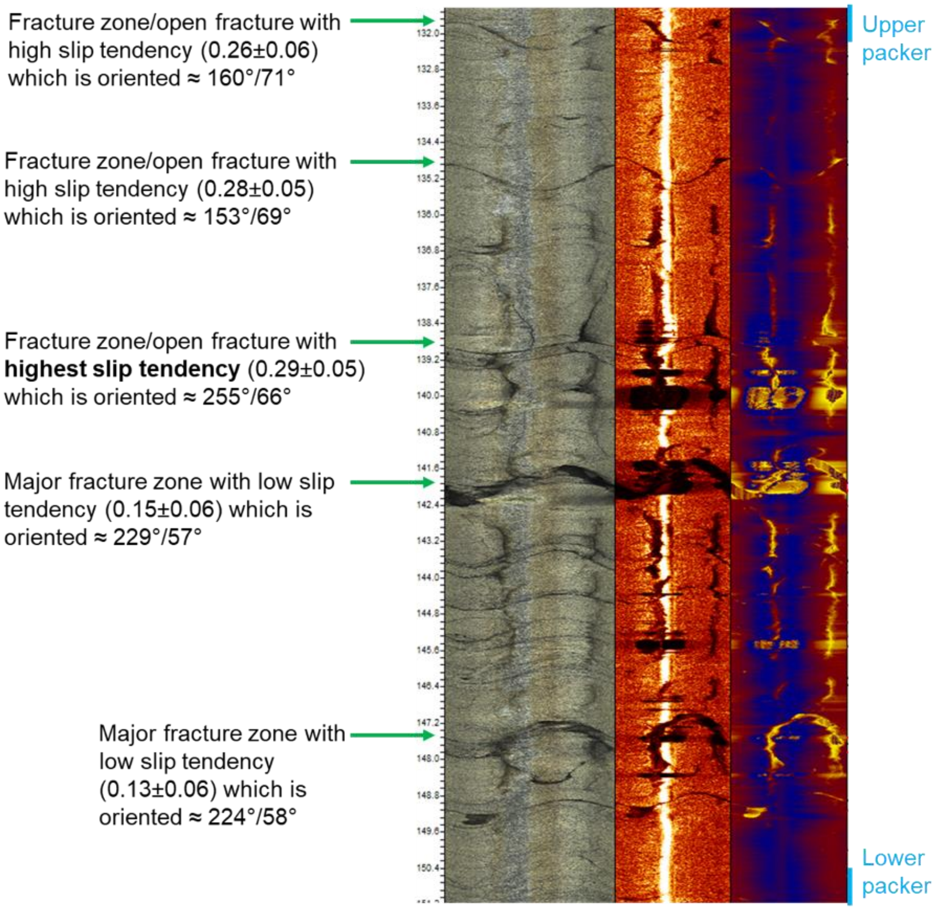

Figure 5: Detailed acoustic televiewer (ATV) log at Interval 11, highlighting hydraulically active features.

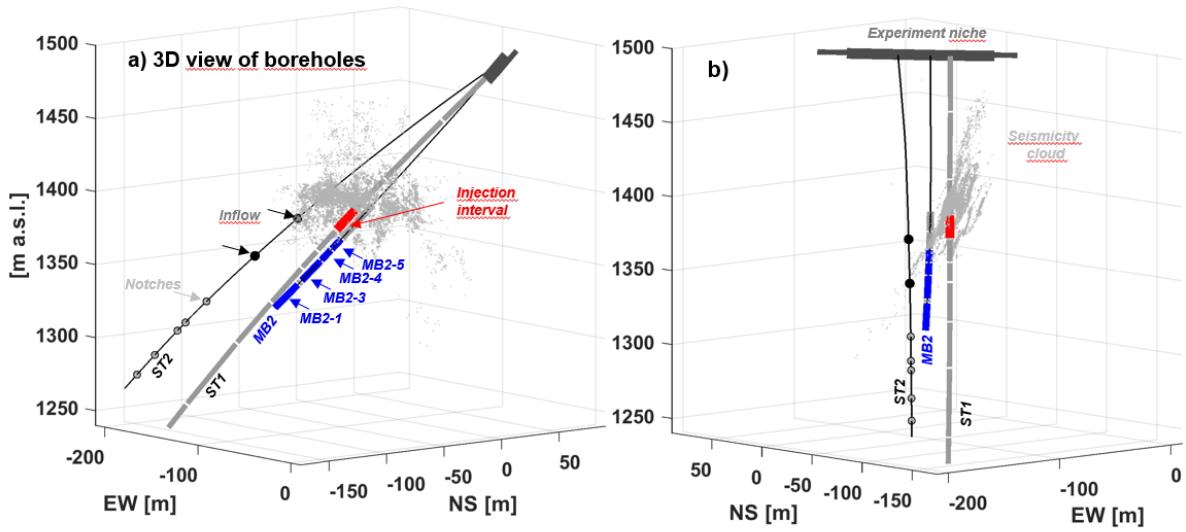

Figure 6: 3D view of borehole ST1 with the target interval 11 highlighted in red, along with adjacent boreholes including ST2 and the monitoring borehole MB2 MB, which contains 7 distinct monitoring intervals.

3.1.2. Uphole hot water injection system

The uphole hot water injection system was specifically designed and engineered within the BEACH project to enable controlled, high-temperature fluid injection under field conditions. It builds upon an existing high-pressure injection line developed in earlier projects at the BedrettoLab. This injection line was amended with i) a new set of high-pressure injection pumps, allowing for more versatile injection schemes and pump-swapping to allow cooling during high-temperature injections and ii) a set of two flow-through boilers with a separated heat-exchanger circuit for constant hot water supply at capacities required for a stable long-term injection.

Figure 7: Left: Jaspi flow-through heater with separate heat exchanger circuit. Right: array of six high-pressure injection pumps with a combined capacity of up to 270 L/min.

The entire system is integrated into a fully automated, remotely controlled operational framework, designed to ensure both operational efficiency and safety under demanding conditions. Critical components and parameters, such as low-pressure water supply, high-pressure thresholds, thermal limits of the pumps, and integrity of the flowline, are permanently monitored, and robust fail-safe mechanisms are implemented. Any loss of connectivity or exceedance of predefined safety thresholds of control parameters triggers an automatic shutdown sequence, including controlled termination of injection (shut-in) and depressurization (bleed-off) of the well system. This functionality is particularly crucial in the context of induced seismicity management. All operational data are continuously streamed to a centralized database and visualized in real time via dedicated dashboards at the project headquarters, enabling continuous situational awareness and rapid decision-making.

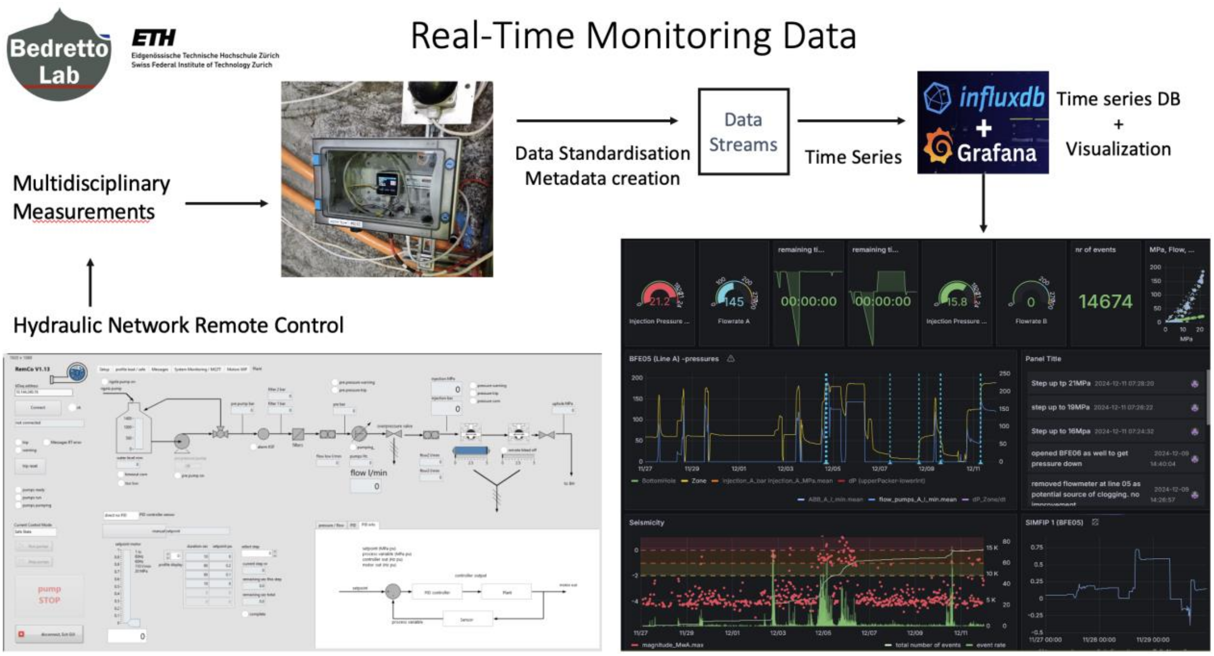

Figure 8: Schematic of the remote system architecture, including automated control, standardized data acquisition, transmission, and real-time visualization. Data are managed via the Bedretto Influx database and can be made accessible to external users.

With this system automation and automatic warnings, the injections are running largely autonomous and operators need a minimum of supervision. During the night, the system is running fully autonomously. Every morning, before regular work starts in the BedrettoLab, the duty seismologist checks for potential seismic events during the night and gives clearance to the on-site team. During daytime operations, the duty seismologist remains on call to respond to elevated seismicity levels or other unexpected events, ensuring adaptive and risk-informed system operation.

3.1.3. Injection schedule

The injection schedule closely follows the proposed plan in the Phase I interim report (Brehme et al., 2025), with two injection/production cycles as key elements: (1) injection followed by a shut-in (resting phase) and a production phase, and (2) injection followed by immediate production (bleed-off). More specifically, the following experiments were conducted:

- ***Cold water injection (2 – 16 June 2025):*** A 14-day injection of unheated tunnel water was performed to test the system, including testing of the pumping infrastructure, injection procedures and flow controls, monitoring setup, alert protocols, and reservoir response to sustained injection. This experiment serves as a baseline for comparison with subsequent hot-water injections under comparable operational conditions (i.e. similar flow rate and duration). The injection rate was maintained at 12 L/min, corresponding to the maximum flow rate to not reach jacking conditions i.e., overpressure of about 17 MPa, (Gischig et al., in review). During this injection, pressure increased to approximately 16 MPa, and a total volume of 240.87 m^3 was injected.
- ***1st hot water injection cycle (28 October – 1 December 2025):*** Hot water at an uphole temperature of ~80°C was injected over 15 days at a constant rate of 12 L/min, for comparability with the cold-water injection, resulting in a total injected volume of 246 m^3. Two short interruptions (16 hours and 0.5 hours) occurred due to an internet outage and a pump sensor failure, respectively.

Following injection, the borehole was shut-in on 12 November 2026 for a 12-day rest phase and subsequently reopened (bleed-off) on 24 November for production until 1 December. A total of 57 m^3 of water was recovered during this phase.

- ***2nd hot water injection cycle (1 December 2025 – 8 January 2026):*** A second hot-water injection was conducted at ~80°C and 12 L/min over 13 days, with a total injected volume of 217 m^3. In contrast to the first cycle, production was initiated immediately after shut-in on 14 December (bleed-off configuration), without a prolonged rest phase. The well remained open for production until 8 January 2026, yielding a total recovered volume of 220 m^3.
- ***3rd hot water injection cycle (3 – 24 February 2026):*** The third cycle implemented a daily cyclic injection scheme, consisting of 8 hours of injection (09:00–17:00) followed by 16 hours of shut-in. This configuration is designed to emulate realistic energy market conditions, where (cheap) excess energy is available during daytime periods. A total of 21 daily cycles were completed, with a cumulative injected volume of 220 m^3. The well was opened immediately after the final cycle for production (bleed-off).
- ***Hydromechanical tests:*** A series of step-pressure tests (SPT) were conducted to characterize key hydromechanical parameters, including injectivity, jacking pressure, and seismic reactivation thresholds at different stages of the experimental phase. These tests followed the standardized protocol established during the Mzero experiments, ensuring consistency in the assessment of reservoir conditions. SPTs were performed on 8 May 2025, 14 September 2025, and 29 September 2025, prior to the hot-water injection campaigns.
- ***Hydraulic tests***: A comprehensive series of hydrotests, including constant withdrawal tests, pulse tests and constant rate tests were performed before the hot water injection cycles to analyse possible changes of hydrogeological conditions in interval 11. These were performed between 1 - 23 October 2025.

3.2. Monitoring system

3.2.1. Monitoring boreholes

The Geoenergy testbed comprises two injection boreholes (ST1 and ST2) and a network of seven monitoring boreholes (MB1 to MB8, except MB6, which was abandoned). A detailed description of the borehole layout and instrumentation is provided by Plenkers et al. (2023) (Figure 9 and Figure 10). Table 1 gives information about orientation and length of each borehole, and their spatial relation to Interval 11 in ST1. Although ST2 was originally designed as a stimulation borehole, it is not used for injection due to technical limitations (see Section 5.1). Instead, it serves as a key observation borehole for monitoring fluid outflow, dissolved noble and reactive gases, and geochemical evolution.

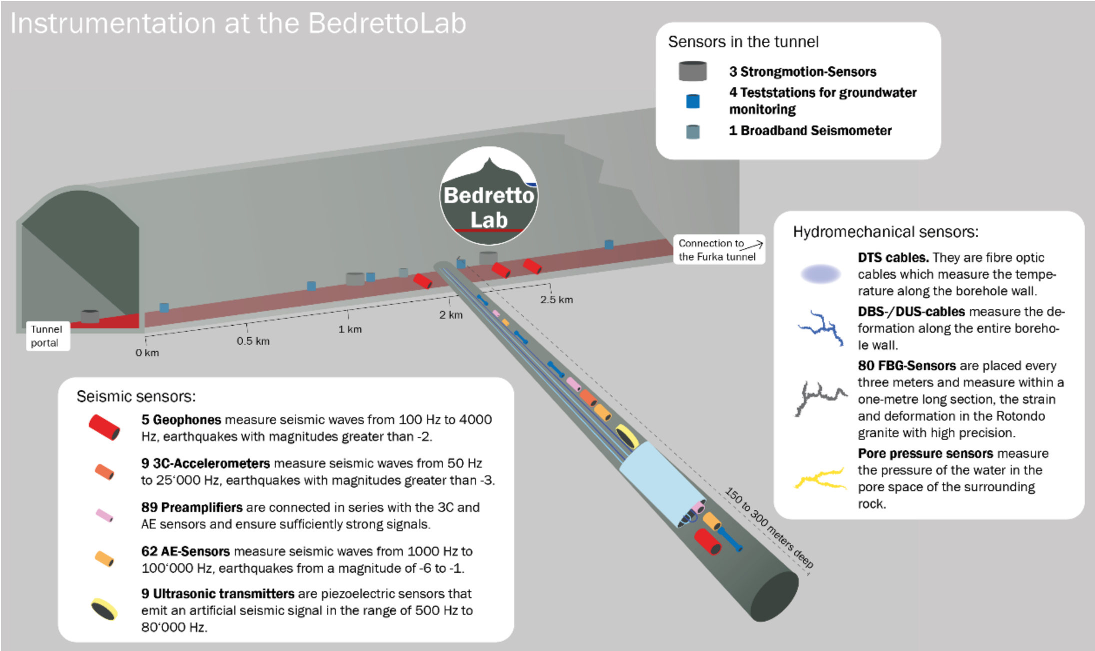

Figure 9. Overview of seismic and hydromechanical sensors installed in the monitoring boreholes and tunnel (source: BedrettoLab/ETH Zürich).

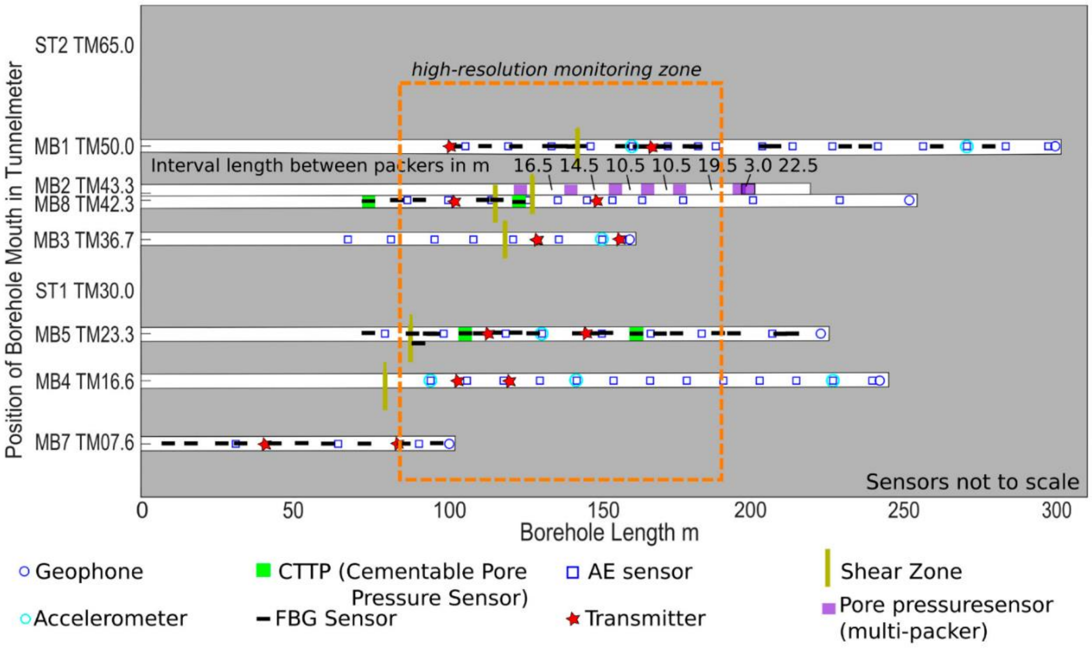

Figure 10. Sensor distribution within the monitoring boreholes MB1 to MB7 of the Geoenergy testbed, including spatial reference of the wellhead (TM##) to tunnel coordinates and the stimulation boreholes ST1 and ST2 (after Plenkers et al., 2023).

Table 1. Geometric characteristics of boreholes and their distance to Interval 11 in borehole ST1 (after Plenkers et al., 2023).

Borehole	Length (m)	Mean Azimuth (deg)	Mean Dip (deg)	Max. Deviation (m)	Distance to ST1-Int11 (m)	Borehole Diameter (mm)
ST1	404.8	227.10	49.15	20.9	0	216
ST2	350.9	224.68	41.79	25.1	32.9–47.0	216
MB1	304.2	227.56°	40.3	24.4	19.9–45.4	165
MB2	221.7	227.66	48.0	7.7	13.4–16.5	101
MB3	189.6	225.84	32.56	24.8	6.7–45.3	165
MB4	253.3	226.46	45.43	15.5	12.8–16.3	165
MB5	221.8	225.63	44.42	9.4	6.3–13.4	165
MB7	101.1	252.11	23.62	11.2	13.2–35.7	165
MB8	252.0	219.36	52.41	12.9	11.1–25.6	165

3.2.2. Pressure monitoring

Injection pressure is continuously monitored uphole, while downhole pressure sensors are installed in each interval of ST1 to capture local reservoir response (Figure 11). At the time of the experiments described in Section 3.1.2, 9 out of 14 interval sensors were operational, including the sensor in Interval 11. Additional pressure monitoring is conducted via dedicated monitoring cells in boreholes MB5 and MB8, each equipped with two sensors (one operational per borehole during the experiment). Borehole MB2 hosts a multi-packer system isolating seven monitoring intervals, with pressure recorded uphole. Due to technical constraints, interval MB2-6 is not functional, and interval MB2-4 was intentionally opened because of its strong hydraulic connection to interval 11 and the expected strong pressure increases exceeding the pressure rating of the surface pressure lines. The interval was instead repurposed for geochemical monitoring (see Section 3.2.6).

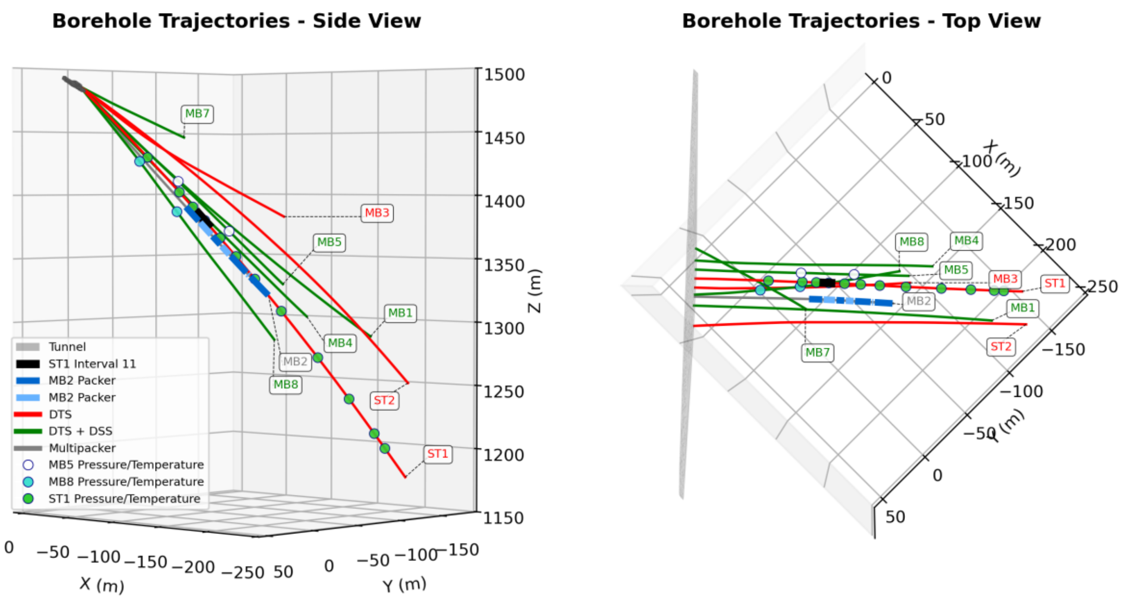

Figure 11. Monitoring boreholes (MB1 to MB8) and stimulation boreholes (ST1 and ST2) showing the installation of optical fibres (DTS, DSS) and multi-packers, FBG sensors, and pressure/temperature sensors active during the hot injection.

3.2.3. Temperature monitoring

Temperature measurements are acquired through combined pressure–temperature sensors installed in the intervals of ST1, as well as in monitoring boreholes MB5 and MB8 (Figure 11). In addition, distributed temperature sensing (DTS) is implemented using multi-mode fibre-optic cables installed in all boreholes except MB2, which is equipped with a multi-packer system that limits fibre deployment (Figure 12). This configuration enables high-resolution spatial and temporal tracking of thermal propagation within the reservoir.

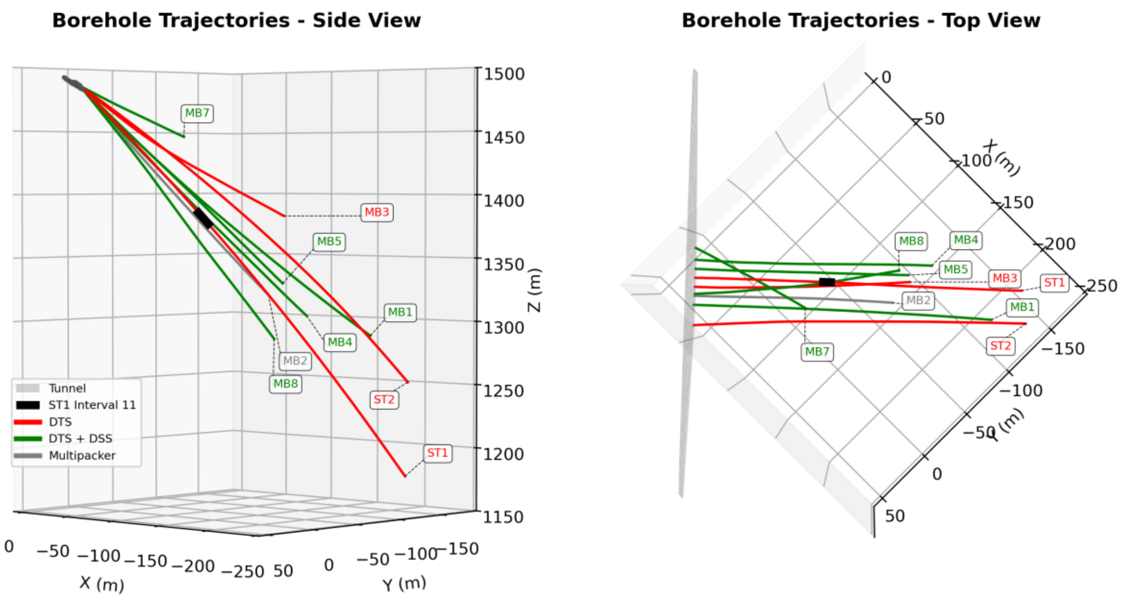

Figure 12. Monitoring boreholes (MB1 to MB8) and stimulation boreholes (ST1 and ST2) showing the installation of optical fibres (DTS, DSS) and multi-packer active during the hot injection.

3.2.4. Deformation monitoring

Deformation is monitored using single-mode cables for either Distributed Strain Sensing (DSS) using Brillouin scattering or Distributed Acoustic Sensing (DAS) using Rayleigh scattering in boreholes MB1, MB4, MB5, MB7 and MB8. All five boreholes were measured with a DSS interrogator during the cold water injection. Excluding the potentially malfunctioning loop in MB1 improved the data quality of the remaining boreholes during the hot water injections.

Distributed Acoustic Sensing (DAS) was installed in boreholes MB3 (19 channels), MB5 (27 channels), and MB8 (30 channels), providing dense spatial sampling of the seismic wavefield within the monitoring volume. Measurements after 04/11/2025 used a sampling frequency of 2000 Hz and a spatial sampling interval of 1.6 m. With such sampling rate, DAS strain-rate measurements can capture earthquake waveforms across a range of magnitudes, potentially contributing to microseismic monitoring in the future. Detectability remains dependent on instrumental and installation-related factors.

In addition, fiber Bragg grating (FBG) sensors (Figure 13) are installed in MB1, MB5, MB7 and MB8, providing continuous measurement of strain with frequency of 1000 Hz and accuracy of 1 µε (improving to 0.1 µε when averaged and downsampled to 1 Hz). Out of 70 installed sensors, 50 were operational during the BEACH injection experiments.

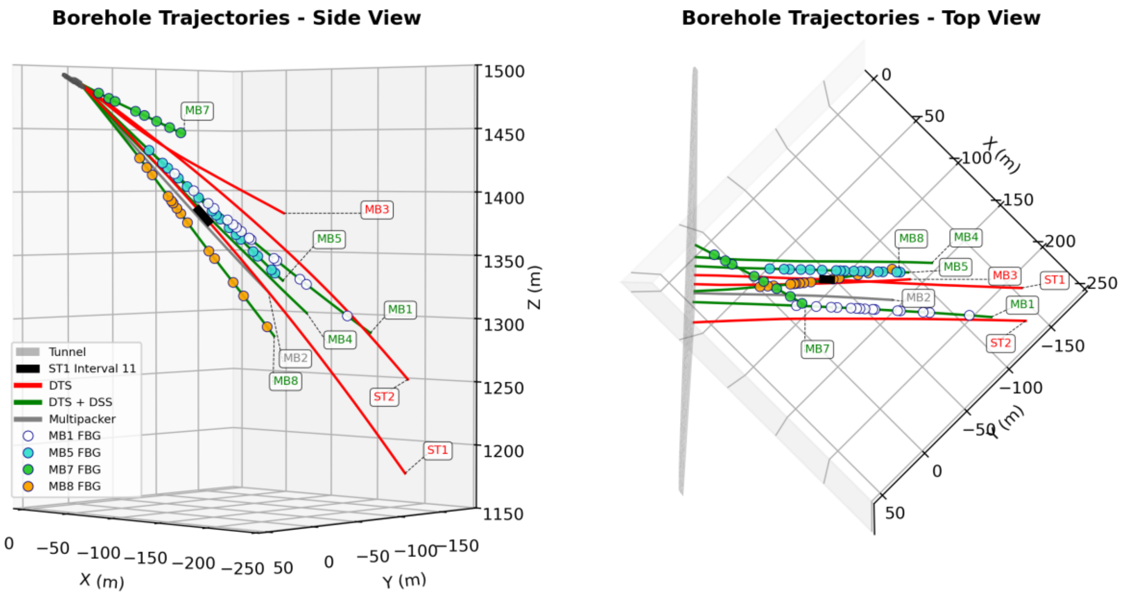

Figure 13. Monitoring boreholes (MB1 to MB8) and stimulation boreholes (ST1 and ST2) showing the installation of a) optical fibers (DTS, DSS), multi-packer and FBG sensors active during the hot injection.

3.2.5. Noble and reactive gas monitoring

Noble and reactive gas monitoring is employed to investigate fluid dynamics mixing processes, and reservoir connectivity during injection experiments. These measurements provide direct insight into flow pathways and interactions between injected fluids and resident groundwater within the fractured rock mass under controlled injection conditions.

Two complementary applications of dissolved gas monitoring are relevant in this context. First, naturally occurring noble and reactive gas concentrations in groundwater can be used as conservative indicators of fluid origin, mixing behaviour, and characteristic residence time. Second, noble gases may be deliberately added as artificial tracers to directly track injected fluids and their transport through the fractured reservoir. While both approaches are applied within the BEACH project, they serve different purposes and together provide a more complete picture of fluid behaviour. Krypton was artificially added as a dissolved tracer into ST1, allowing the observation of breakthrough behaviour and hydraulic connectivity at monitoring locations such as ST2 and Interval 4 in MB2.

Noble and reactive gas monitoring, including Krypton tracer breakthrough, was carried out during the cold water injection only, with the primary aim of establishing baseline circulation behaviour and testing the monitoring approach ahead of future hot water circulation experiments.

The experience gained during the cold water injections form the basis for refining the monitoring strategy and tracer protocols in subsequent experimental phases, where noble and reactive gas-based observations can play a central role in quantifying circulation efficiency and reservoir connectivity under thermal loading conditions. Due to unavailability of the instrument no further gas monitoring could be done during the hot water injections.

3.2.6. Monitoring of geochemical and microbiological parameters

It is estimated that more microorganisms live within the continental subsurface than the global oceans. These subsurface microorganisms are well adapted to the physical-chemical conditions of the subsurface, including microbial lineages that can rapidly metabolize nutrients supplied by subsurface operations. In the context of heat storage, stimulating microbial activity can potentially result in bioclogging, corrosion, microbial mineral precipitation, or microbial gas production. Biogeochemical monitoring aims to assess changes in fracture fluid-associated microbial communities induced by injection, measure the persistence of heat-induced alterations to the chemical and microbial composition, and quantify the transport of microbial and chemical species into the wider subsurface system.

The BEACH biogeochemical monitoring is conducted across a distributed network of observation points to capture system-wide responses (Figure 14). The near-field reservoir around the injection interval is monitored at sites ST1 Interval 11, MB2 Interval 4, and ST2. Additionally, sites located along potential flow paths are included, such as water from fractures TM1306 and TM1494 and the short borehole GB1. Injection water and water from fracture TM2848, the primary source of the injection fluid, are also monitored. Biogeochemical monitoring is continued prior, throughout, and after active injections to also assess the recovery of the system.

Our measurements include analyzing water parameters, water chemistry, microbial abundance, community composition, and microbial activity. Additionally, we investigate potential groundwater flow paths and the origins of water and carbon sources through isotopic analyses, including radiocarbon, stable carbon, and water isotopes. Sampling was conducted twice a week during active injections and biweekly or monthly before and after active injections.

The following analyses are included:

1. **Water parameter measurements:** Manual determination of electrical conductivity (EC), pH, temperature, oxidation-reduction potential (ORP), and total dissolved solids (TDS) using handheld probes (HI98129, HHI98121, HANNA Instruments).
2. **Flow rate measurements:** Manual measurements of the outflow rate at MB2 and GB1, complemented by automated monitoring at ST2.
3. **Microbial sampling:** Collection of samples for combined DNA and protein extraction to conduct quantitative PCR, 16S rRNA gene sequencing, metagenomics, and metaproteomics. Sampling of dissolved organic matter (DOM) for solid phase extraction to conduct DOM-based metabolomics and dissolved organic carbon (DOC) concentration analysis.
4. **Water chemistry analyses:** Quantification of major ions (including ammonium, sulfate, nitrate, and nitrite), alongside elemental and water isotope analyses.
5. **Carbon isotope analyses:** Analysis of dissolved inorganic carbon (DIC), dissolved organic carbon (DOC), and particulate organic carbon (POC), including both radiocarbon (^{14}C) and stable carbon isotopes (^{13}C).

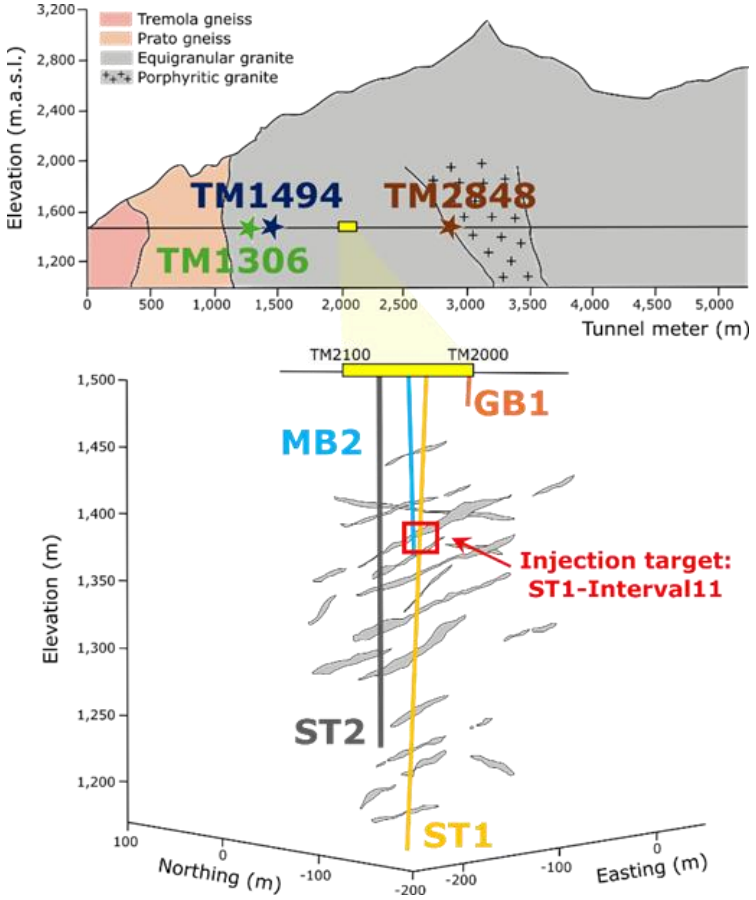

Figure 14: Sites included in the biogeochemical monitoring of BEACH (modified after Acciardo et al., 2025. Front. Microbiol. 16:1522714).

3.2.7. Self-potential (SP) monitoring

Self-potential (SP) monitoring is employed to investigate fluid flow processes associated with injection and production in fractured crystalline rock. The method measures naturally occurring electrical potential differences and is primarily sensitive to electrokinetic (streaming potential) effects generated by fluid flow, with possible additional contributions arising from temperature gradients. The monitoring system consists of eight non-polarizable Pb/$PbCl_2$ electrodes installed in the vicinity of the injection borehole ST1. The electrodes are distributed along the tunnel axis between approximately –99.5 m (electrode S95) and +99.5 m (N95) relative to ST1. Additional electrodes are positioned at distances of approximately ±1.7 m (S1, N1), ±15–18 m (S18, N18), ±34–35 m (S32, N32), and +49.5 m (B60), enabling spatially resolved detection of electrokinetic signals (Figure 15). Measurements are recorded as potential differences relative to the reference electrode S95 at a temporal sampling rate of 1 minute, with continuous acquisition initiated in late October 2025.

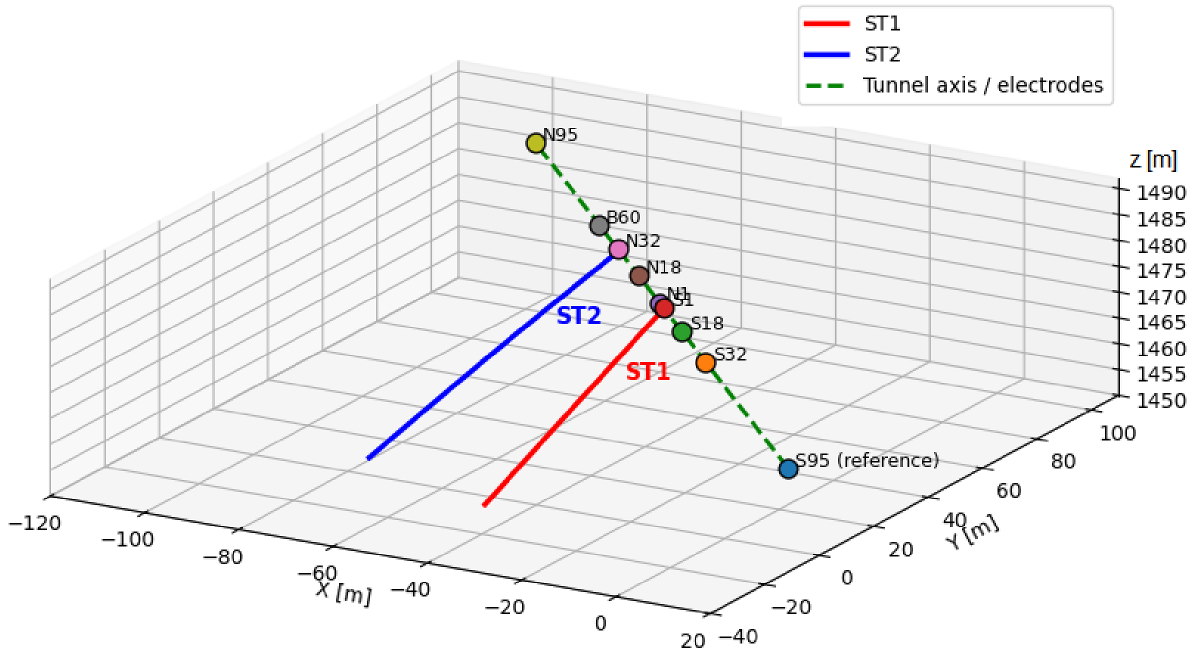

Figure 15: Overview of self-potential (SP) electrodes (circles) installed along the tunnel wall (dashed line) relative to ST1, highlighting the spatial coverage of the monitoring array. Electrode S95 serves as reference for calculating SP differences.

3.2.8. Seismic monitoring

Seismic monitoring is based on three complementary networks with distinct monitoring characteristics and sensitivities: the BedrettoLab experimental network, the BedrettoLab permanent network, and the national seismic network (Figure 16).

The **experimental network** consists of acoustic emission sensors and high-frequency accelerometers embedded in the described monitoring boreholes. They are sampled at 200 kHz and serve the goal of locating seismic events with magnitudes down to Mw<-4.0 with decimetre to meter relative accuracy. The network has been proven to resolve the reactivated fracture networks in great detail. However, this high-resolution network can only characterize seismicity within and at short distances around the monitoring boreholes. Magnitudes from this system are apparent moment magnitude MwA based on amplitudes recorded by the acoustic emission sensors and accelerometers.

The **permanent network** serves as a backbone network and includes broadband sensors at the surface and along the tunnel, as well as strong-motion sensors and high-frequency geophones along the tunnel and in boreholes. The sampling rate depends on sensor type and proximity to the experimental reservoir (200–2000 Hz). The network is less sensitive than the experimental network but can detect and localize seismicity beyond the experimental volume. The network provides a Bedretto-specific local magnitude termed MLc.

These networks are complemented by the **national network** run by the Swiss Seismological Service (SED) at ETH Zurich. All networks are integrated in the automatic detection and locating system called SeiscomP.

Using the permanent network, the national network and dedicated tunnel stations (not part of the previous networks), an alarming scheme was set up:

Red alert, if MLc≥1.5. Action: rapid screening for false alert; initiate bleed off if injection is ongoing; Immediately evacuate the tunnel, detailed analysis.

Orange alert, if MLc≥0.5 or PGV≥2.5 mm/s. Action: rapid screening for false alert; initiate bleed off if injection is ongoing; stop all activities in the lab and abandon the tunnel within one hour unless overruled by BedrettoLab Executive Committee (ExeCom) member based on technical analysis; manual analysis of seismicity and update hazard assessment; next stimulation only after BedrettoLab ExeCom decision.

Yellow alert, if MLc≥-0.5 or PGV>0.5 mm/s: Action: rapid screening for false alert; initiate bleed off if injection is ongoing; manual analysis of seismicity; update hazard assessment; next stimulation only after BedrettoLab ExeCom decision.

A seismic hazard study based on past experiment in the BedrettoLab showed that the seismic hazard is very small for the BEACH injection in particular since the injections do not pressure levels above which seismicity is reactivated (i.e. jacking pressure). Thus, seismological duty was setup to be operational between 7 AM and 6 PM during workdays. Additionally, screening for alarm events was done before 7 AM every workday in the morning to give clearance to the personnel going into the tunnel.

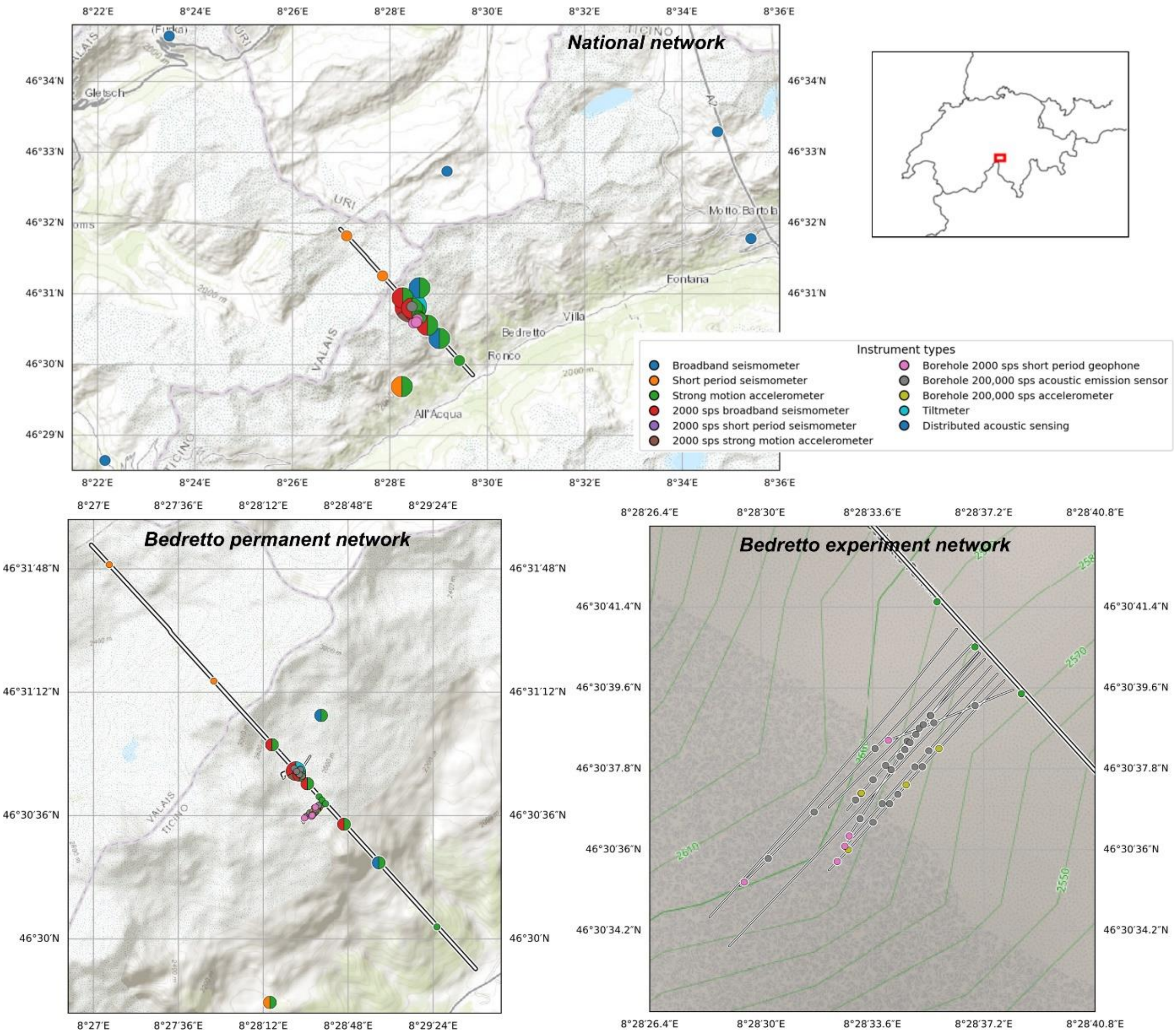

Figure 16: The three levels of seismic monitoring operational during the BEACH experiments.

3.3. Experiment results

3.3.1. Injection rate, pressure, temperature

Figure 17 presents the temporal evolution of injection rate during the experimental phases described in Section 3.1.3, along with pressure and temperature records measured by different sensors. During both cold- and hot-water injections, a constant injection rate of 12 L/min resulted in a gradual increase of downhole pressure in interval 11 to values exceeding 160 bar. Periods during which downhole pressure drops to 11.4 bar correspond to production (bleed-off) phases during which ST1 was opened.

Hydraulic responses in response to pressure variations in Interval 11 of ST1 are more prominent in Intervals 8, 9, 12 and 14, with the strongest changes in interval 12, consistent with its known hydraulic connectivity to Interval 11 from previous experiments. In contrast, Intervals 5 and 6 show no measurable response, indicating their location within a hydraulically disconnected, deeper compartment.

Monitoring intervals in MB2, MB5 and MB8 exhibit moderate pressure increases below 20 bar, indicating an existing yet limited hydraulic connection. No pressure response is shown for interval MB2-4, as it was intentionally opened to avoid overpressurization and repurposed for geochemical and microbiological monitoring.

Clear temperature changes are observable only in intervals in ST1 located above Interval 11. The shallowest interval (Interval 14) reaches temperatures of up to ~40°C, whereas Intervals 11 and 12 show more moderate increases (~33°C). This temperature pattern reflects **significant thermal losses along the borehole**, as expected, as the hot water descends through an uninsulated borehole prior to reaching the injection interval. In contrast, temperature changes below the injection interval and within the surrounding rock mass (e.g. in MB5 and MB8) remain minimal, typically not exceeding ~0.1°C. In particular the readings in MB5 and MB8 suggest **limited thermal breakthrough** into the far field under the tested conditions.

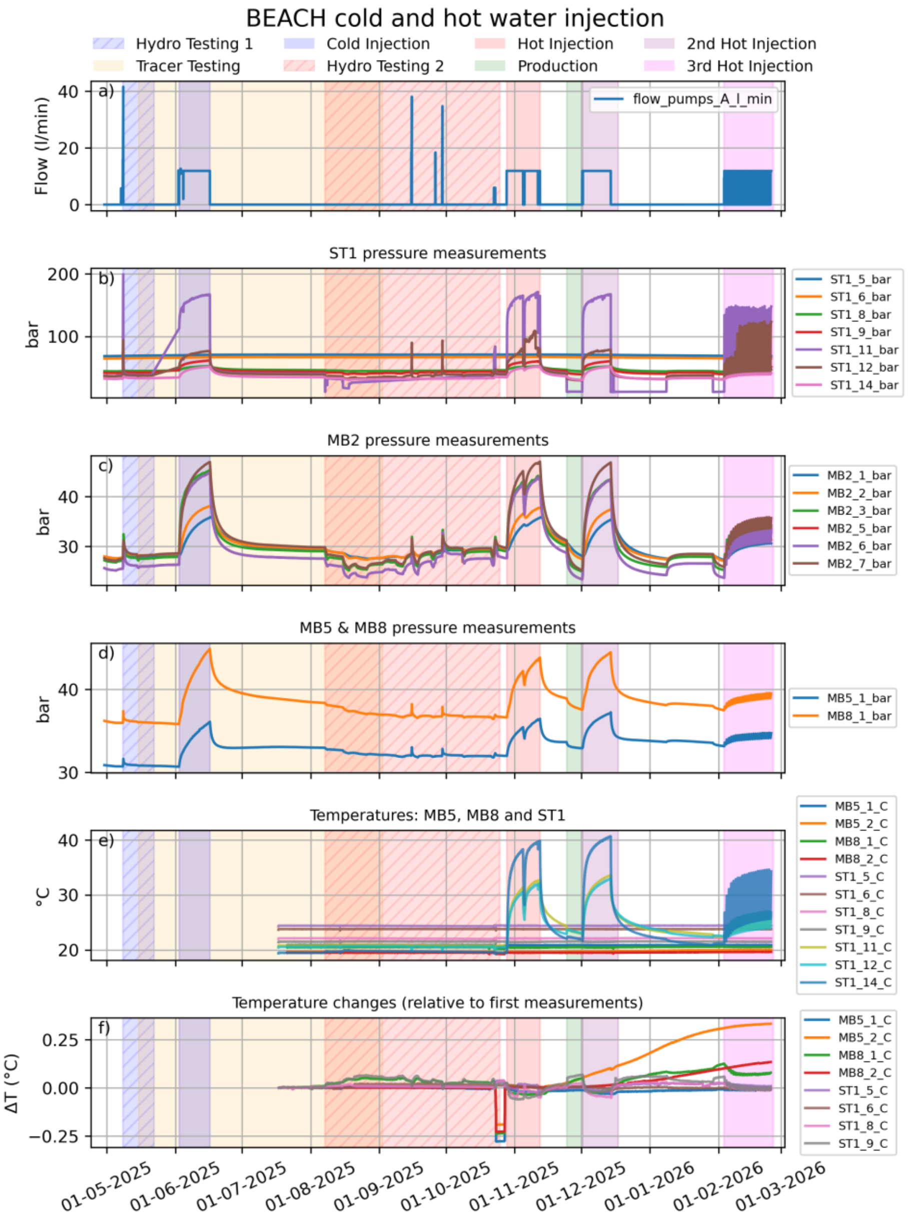

Figure 17: Summary of experimental observations: a) injection flow rate, b) downhole pressure evolution in ST1 intervals, c) uphole pressure in MB2 intervals, d) downhole pressure in monitoring boreholes, e) downhole temperature evolution in ST1, MB5 and MB8 and f) temperature changes relative to first measurement of monitoring locations with low thermal response.

3.3.2. Distributed Temperature Sensing (DTS)

Distributed Temperature Sensing (DTS) provides continuous, high-resolution temperature measurements along the boreholes, offering a detailed view of thermal evolution during injection and production phases (Figure 84 and Figure 85 in Appendix). Temperature changes derived from DTS in ST1 (Figure 18) clearly confirm pronounced heating of the borehole section above Interval 11, indicating substantial thermal losses along the borehole prior to injection into the target interval. The temperature at the top of ST1 reaches 56°C (ΔT=37°C; recall that, in the absence of losses, the nominal injection temperature was 80°C) at the end of the second hot water injection cycle, whereas temperatures at Interval 11 remain significantly lower (~33°C, corresponding to ΔT=12°C). Following shut-in after the first hot-water injection cycle, temperature decay at Interval 11 is slower than in the shallower Interval 14 (Figure 18b). This behaviour suggests that a larger volume of surrounding rock is thermally affected near Interval 11 by advection, resulting in increased thermal storage capacity and slower heat dissipation (recall that the impact of heat conduction is similar in both intervals). These observations provide direct evidence that heat is effectively stored within the fracture network connected to the injection interval.

DTS data from surrounding boreholes (Figure 19) further constrain the spatial extent of thermal propagation. Boreholes MB4 and MB8 show no significant temperature variations, with minor apparent changes interpreted as measurement artifacts. Slight temperature changes of <1°C are observed in boreholes MB3 and MB5, primarily at shallow depths and with a delay of several days following the first hot-water injection cycle, consistent with conductive heat transfer from the heated upper section of ST1. In MB5, small but localized temperature increases of ~0.1°C at depths of approximately 60 m and 140 m may indicate limited inflow through fractures transporting small amounts of heat. However, the overall magnitude of these changes remains minimal.

Importantly, the absence of significant temperature changes in boreholes surrounding ST1 indicates that the **thermal energy injected in Interval 11 is largely retained within the near-field fracture network and rock matrix, with negligible propagation into the far field (**Figure 19**).** This behaviour is highly favourable for thermal energy storage, as it minimizes heat loss beyond the target reservoir volume.

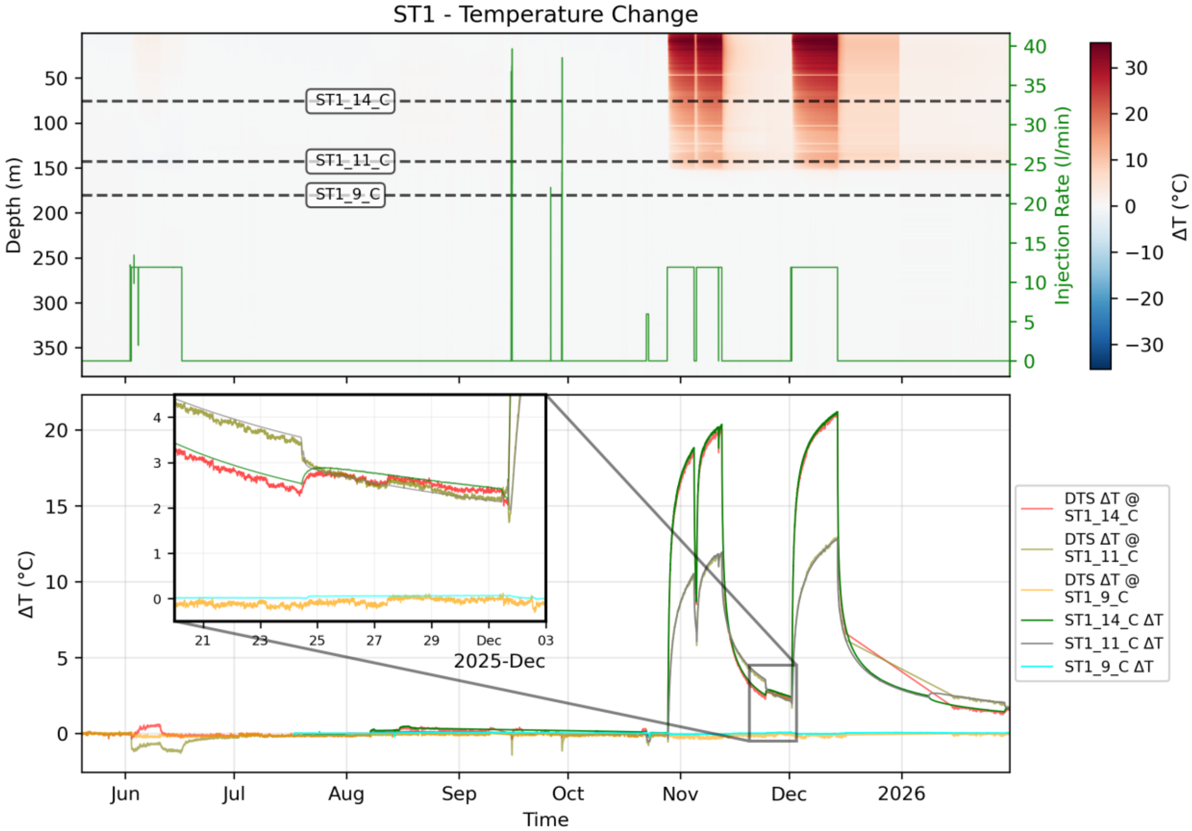

Figure 18: a) DTS-derived temperature changes in ST1 relative to initial temperature (20 May 2025). Dashed lines indicate depth of selected intervals; b) comparison between DTS-derived temperature changes and downhole temperature sensors for validation.

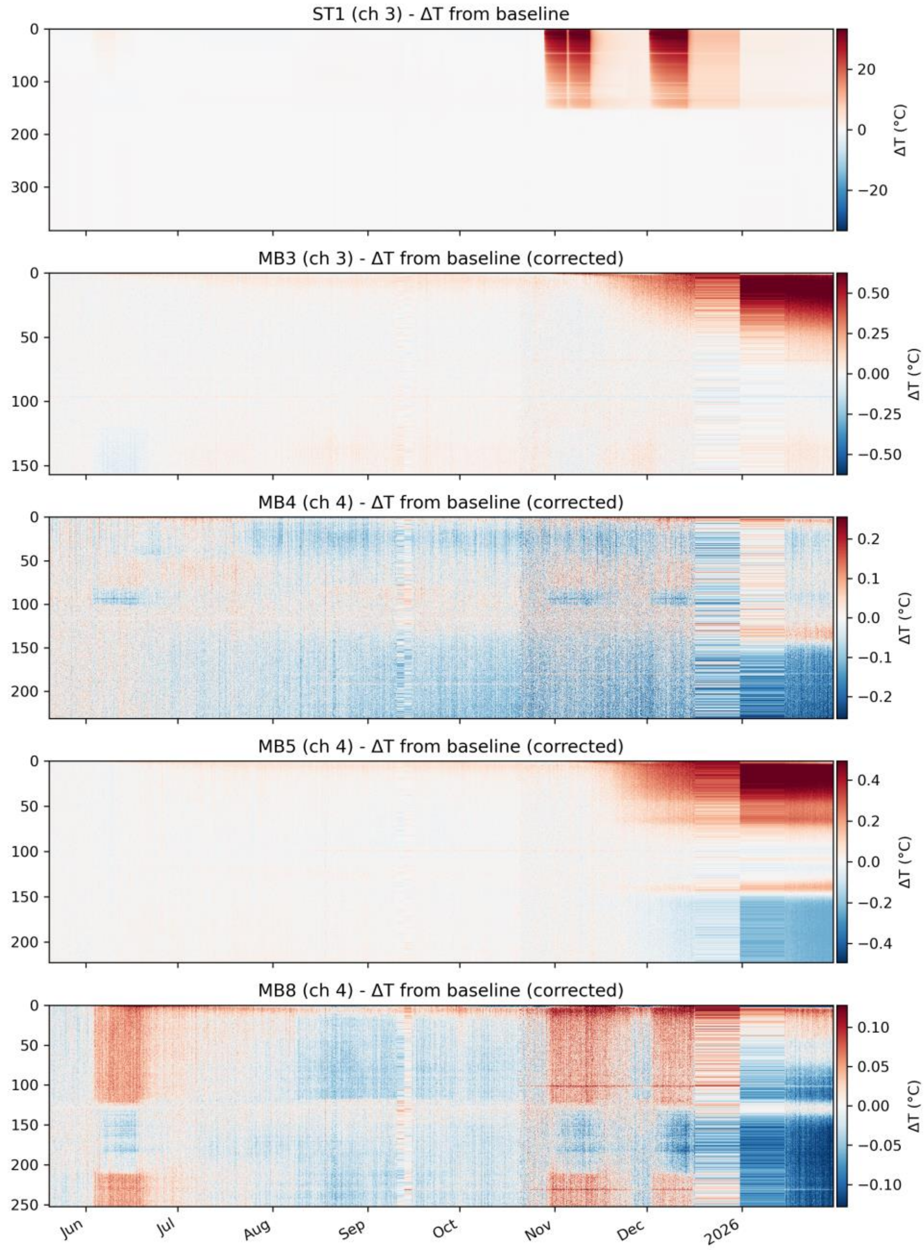

Figure 19: DTS-derived temperature changes in monitoring boreholes surrounding ST1. Illustrating limited thermal propagation into the far-field.

3.3.3. Distributed Strain Sensing (DSS)

Distributed Strain Sensing (DSS) provides insight into deformation associated with fluid flow and pressure propagation within the reservoir. Measured strain signals identify zones of fluid entry into monitoring boreholes, expressed as localized extensional strain (positive strain in Figure 20). Pronounced extensional zones are observed in boreholes MB4, MB5, and MB8, indicating hydraulically active inflow regions during injection. In contrast, MB7 (not shown) exhibits no significant deformation response, while MB1 showed no clear signal already during cold-water injection, likely reflecting weak hydraulic connectivity. After excluding MB1 from the DSS measurement loop due to suspected malfunction, overall data quality improved significantly, as evidenced by reduced noise levels in subsequent measurements (Figure 20).

Notably, temperature changes observed in MB5 (Figure 19) spatially coincide with distinct extensional zones identified in DSS-derived data supporting the interpretation of localized fluid inflow carrying limited thermal energy. In contrast, other extensional zones (i.e. potential inflow zones) in MB4 and MB8 are not associated with measurable temperature in the DTS dataset**,** indicating that **pressure perturbations propagate further than the thermal front.**

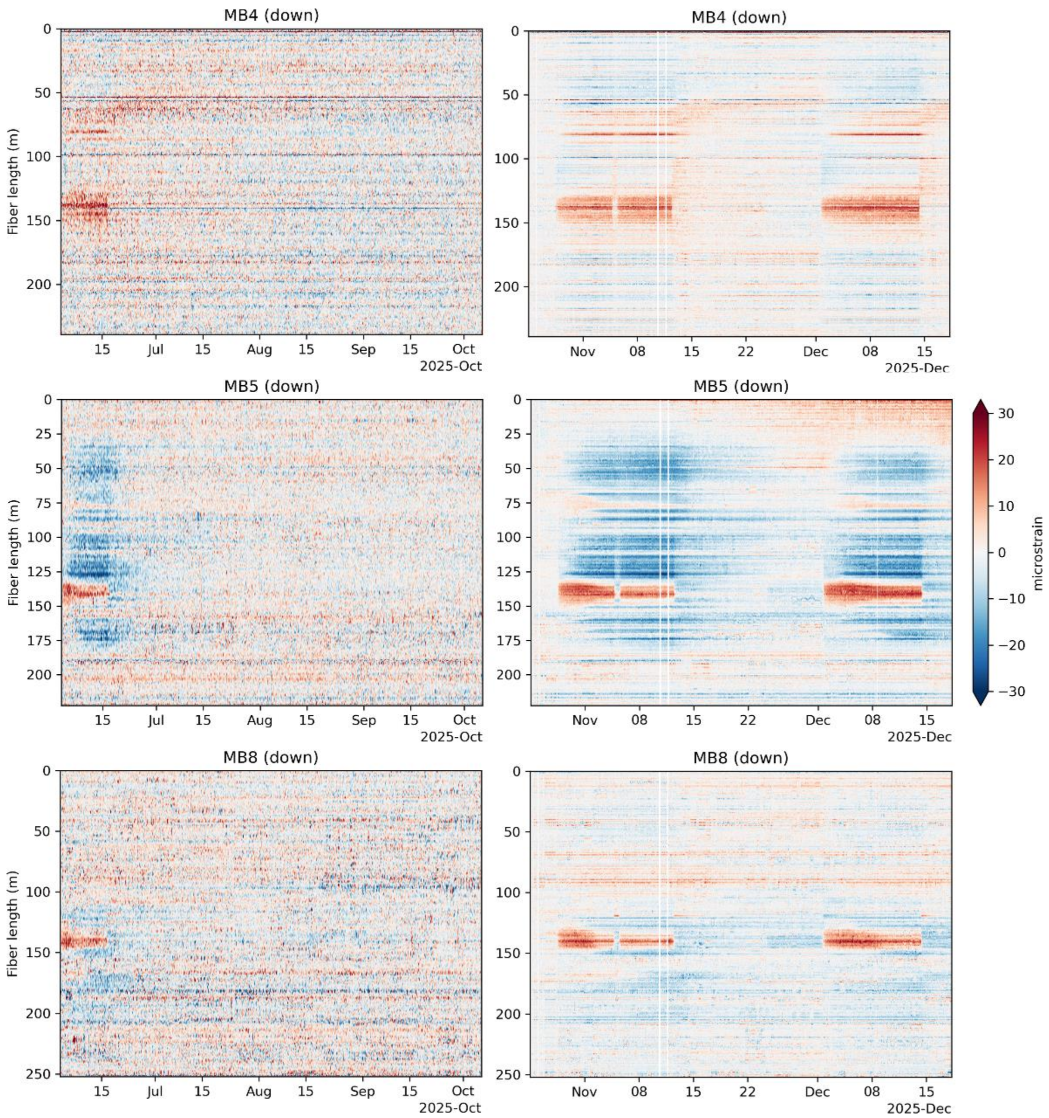

Figure 20: Longitudinal strain measured with DSS in boreholes MB4, MB5 and MB8 during the cold- water (left) and hot-water injections (right).

3.3.4. Energy balance

Temperature measurements, together with injection and production rates, are used to estimate the energy balance of the single-borehole storage system (Figure 21, Table 2). The analysis is performed for the water leaving the boilers with 80°C, when it enters the boreholes and at the level of the injection interval, i.e. considering only the thermal energy entering and leaving the reservoir. The latter analysis excludes losses along the tunnel and borehole and represents an idealized system with a perfectly insulated wellbore and isolates the performance of the reservoir itself. Further, the reference temperature for injected heat is set to 17°C, corresponding to the temperature of the water of the stream in the tunnel, from which the injection water was taken prior to heating.

Table 2: Summary of injected and recovered volumes and thermal energy during the two hot-water cycles. In the calculations below, a fluid with density 1000 kg/m³ and a specific heat capacity of 4180 J/kgK is assumed.

	Hot water cycle 1	**Hot water cycle 2**
Injected volume	246 m³ (during 15 days)	217 m³ (during 13 days)
Recovered volume	57 m³ (during 7 days)	220 m³ (during 25 days)
Thermal energy added by boiler (12 L/min heated from 17°C to 80°C)	17,880 kWh (100%)	15,847 kWh (100%)
Thermal energy loss along tunnel	6,079 kWh (34%)	5,230 kWh (33%)
Thermal energy loss along bore-hole	8,046 kWh (45%)	6,973 kWh (44%)
Thermal energy injected at the in-terval	3,709 kWh (21%)	3,613 kWh (23%)
Thermal energy produced from in-terval	234 kWh	1,256 kWh
Storage efficiency (i.e. ratio of ther-mal energy recovered from Interval 11 to thermal energy injected into Interval 11)	6.3 %	34.8 %

The nominal (i.e., assuming a 100% net efficiency) thermal energy supplied by the boiler system amounts to 17,880 kWh and 15,847 kWh for the first and second cycles, respectively. A significant fraction of this energy is lost prior to reaching the reservoir, with approximately 34–33% dissipated along the tunnel and 45–44% along the borehole, resulting in only 21–23% of the generated heat effectively injected into the target interval.

The net injected thermal energy into Interval 11 was therefore 3,709 kWh and 3,613 kWh for the first and second cycles, respectively. The corresponding recovered thermal energy from Interval 11 amounted to 234 kWh (7 days of production) and 1,256 kWh (25 days of production) **yielding apparent storage efficiencies of 6.3% and 34.8%, respectively**. For a consistent comparison, restricting the analysis of the second cycle to an equivalent production duration of 7 days results in a recovered heat of 421 kWh, corresponding to an efficiency of 11.7%, nearly a factor of two higher than in the first cycle. These results highlight a clear increase in thermal recovery between successive cycles, despite identical injection conditions and the absence of thermal insulation. This behaviour is consistent with the progressive thermal conditioning of the reservoir, whereby repeated injection–production cycles lead to an increase in effective storage efficiency.

It is worth to note that production was conducted against atmospheric pressure, resulting in declining flow rates that stabilize at approximately 3–4 L/min, i.e. only 25–33% of the injection rate (12 L/min). Consequently, the absolute recovery efficiency is influenced by operational constraints, including production duration, flow conditions, and pressure boundary conditions.

Differences in operational strategy between the two cycles further complicate direct comparison. During the first cycle, production followed a 12-day shut-in period, allowing partial thermal dissipation, whereas the second cycle benefited from immediate production and elevated reservoir temperatures. Additionally, only 57 m³ of the injected 246 m³ were recovered during the first cycle, compared to 220 m³ recovered during the second cycle (exceeding the injected 217 m³), indicating significant fluid exchange with the surrounding reservoir. Despite these differences, the observed increase in recovered thermal energy strongly suggests that storage performance improves with repeated cycling, even under suboptimal experimental conditions. Notably, this time-enhanced yield, also termed reservoir conditioning is observed in real projects worldwide (to cite a few, St. Paul in Minnesota (US)–Miller et al., 1994-; Rostock (Germany) -Schmidt and Müller-Steinhagen, 2004-; Neckarsulm-Amorbach (Germany) - Nussbicker et al. (2003)). However, a more rigorous quantification of this effect **requires numerical modelling calibrated against the experimental data, which allows consistent comparison under controlled boundary conditions**.

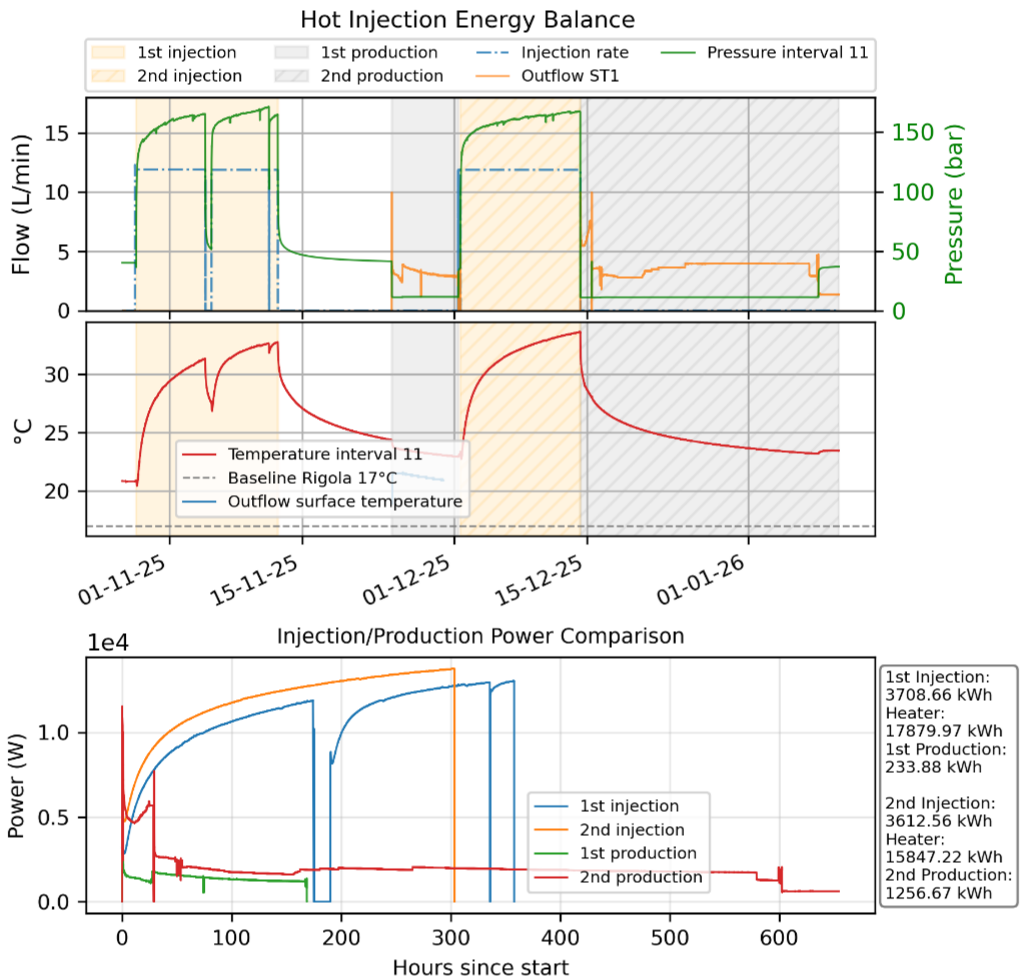

Figure 21: Energy balance of the two hot-water injections: (top) Injection and production rates, injection pressure and temperature; (bottom): Rate of injection and produced thermal energy (i.e., power), evaluated at the interval level and excluding losses along the surface lines or along the borehole.

3.3.5. Noble and reactive gas tracer tests

Figure 22 shows the breakthrough curves of the krypton (Kr) tracer measured at the monitoring boreholes ST2 and MB2 (Interval 4, closest to the injection point). MB2-4, exhibits a steep and rapid breakthrough, with peak concentrations of approximately 1.1 hPa reached within approximately 4.5 days. In contrast, the more distant borehole ST2 shows a broader and delayed signal, with arrival times around 6 days and peak concentrations nearly two orders of magnitude lower (6E-2 hPa).
Elevated baseline concentrations at MB2-4 at the onset of monitoring are attributed to residual tracer from a previous injection campaign conducted approximately one year earlier. The persistence of concentrations above baseline throughout the observation period indicates long-term tracer retention and incomplete flushing.
Tracer detection at ST2 confirms hydraulic connectivity over distances of several tens of meters, demonstrating that injected fluids can access a significantly larger reservoir volume than indicated by pressure signals alone. The comparatively low peak concentrations at ST2 are interpreted as the result of dilution within a larger swept volume and enhanced dispersion along more distributed flow paths, rather than weak hydraulic connectivity. The ST2 breakthrough curve also exhibits pronounced

tailing, with elevated concentrations persisting throughout the monitoring period, consistent with tracer retention and delayed release, likely due either to matrix diffusion or strong heterogeneity of the flow field (Carrera et al., 1998; Alcolea and Carrera, 2001; Silva et al., 2009).
In contrast, MB2-4 shows a more rapid decay in tracer concentration following peak arrival, indicating more efficient flushing and a smaller influence from retention processes. These contrasting behaviours point to fundamentally different transport regimes, i.e., advection dominated, channelized flow toward MB2-4 versus more distributed flow with significant retention effects toward ST2. These observations have important implications for reservoir performance, suggesting that while preferential flow paths enable rapid fluid circulation, a substantial fraction of the injected fluid interacts with a small storage volume around the injection point, which is favourable for thermal energy storage.

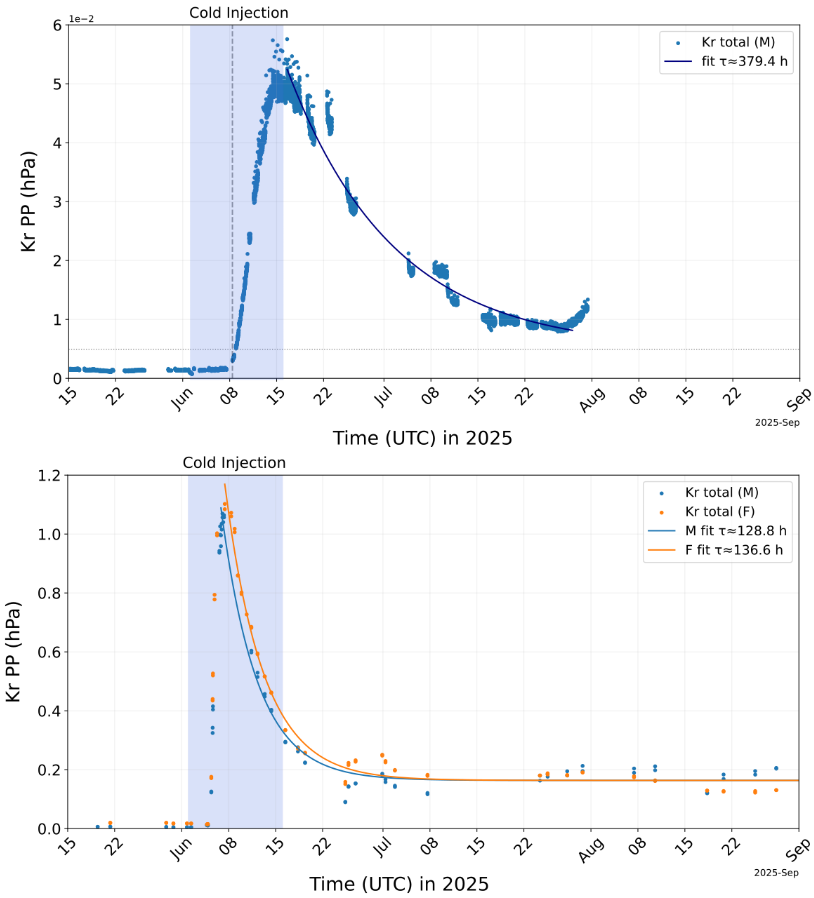

Figure 22: Breakthrough curves of the Kr tracer at monitoring boreholes ST2 (top) and MB2-4 (bottom).

Figure 23 shows the temporal evolution of dissolved noble and reactive gas partial pressures (directly proportional to molar concentrations) measured continuously at ST2 and MB2-4. These data provide complementary insight into fluid mixing, transport processes, and system perturbations during injection. At ST2, N_2 exhibits slightly elevated partial pressures prior to injection (early May), likely reflecting natural temporal variability. Following this period, N_2 remains relatively stable throughout the cold injection phase. Similarly to Ar and He, CO_2 and O_2, concentrations remain generally low and close to detection limits. However, further data processing is required to fully assess subtle variations. Preliminary observations suggest a possible minor O_2 response following the cold-water injection, but this remains to be confirmed through data cleansing and normalization relative to other gas species.

From approximately the 10 August 2025 onwards, slight increases in N_2 and He partial pressures are observed, coinciding with the second phase of hydrotesting. Kr concentrations show more variable behaviour, which may be linked to pressure variations in neighbouring borehole intervals (see Figure 17).

At MB2-4, both He and N_2 show a slight decrease coinciding with the Kr breakthrough, followed by an increase after the cold-water injection period. This pattern is consistent with dilution effects caused by the influx of injected water, followed by re-equilibration with pristine fluids.

Overall, the geochemical signals support the interpretation derived from tracer observations, indicating active fluid exchange, mixing processes, and spatially variable transport dynamics within the reservoir. Further quantitative analysis is expected to refine these interpretations and reveal more subtle system responses.

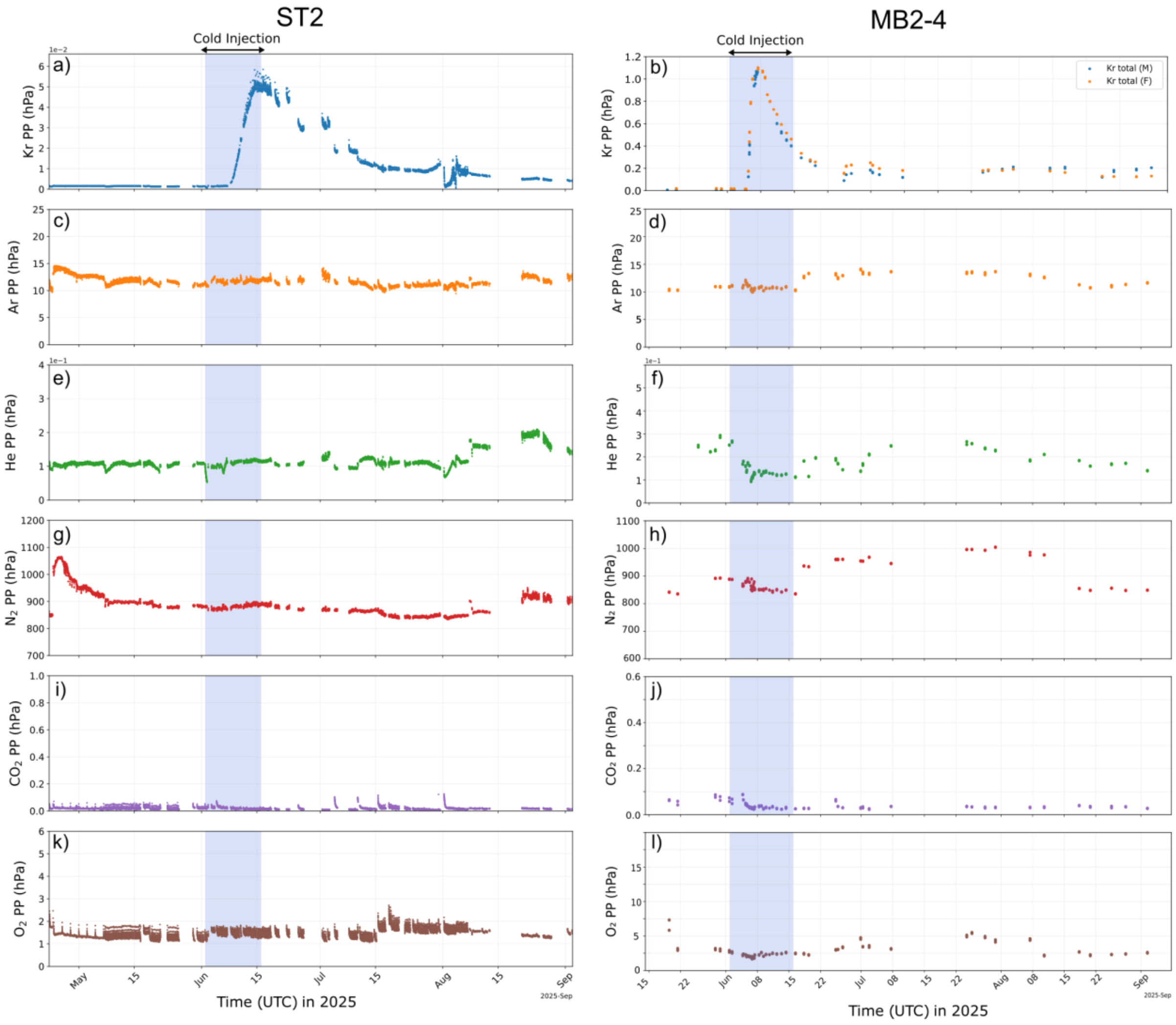

Figure 23: Temporal evolution of dissolved noble and reactive gas partial pressures at ST2 and MB2-4 monitoring boreholes, illustrating system response to injection and tracer transport.

3.3.6. Geochemical observations

Figure 24 - Figure 27 present **time series of flow rate, electrical conductivity, temperature, and pH** measured between **April 2025 and March 2026**. The dataset captures system responses to the cold-water injection conducted in June 2026 and three hot-water injection campaigns conducted in October–November 2025, December 2025, and February 2026, respectively.

Both ST2 and MB2-Interval4 exhibited a clear increase in flow rate during active injection at ST1-Interval11, validating hydraulic connectivity between these locations (Figure 24). ST2 has an average outflow of 19.1 ± 0.5 $L \cdot min^{-1}$, with a maximum increase of 3.9 $L \cdot min^{-1}$ observed during the first hot-water injection. In contrast, MB2-Interval4 has a substantially lower baseline outflow of 0.13 ± 0.03 $L \cdot min^{-1}$, which approximately doubled during injection at ST1-Interval 11. Notably, the response at MB2 occurred within one day, highlighting strong connectivity. No injection-related changes in flow rate were detected at borehole GB1.

Electrical conductivity (EC) measurements at ST1-Interval11 showed a pronounced decrease following injection, dropping from an initial 410 ± 21.1 $\mu S \cdot cm^{-1}$ to values as low as 154 $\mu S \cdot cm^{-1}$ (Figure 25). This reduction reflects the introduction of injection water with significantly lower EC (91.8 ± 7.5 $\mu S \cdot cm^{-1}$). A comparable decrease was observed at MB2-Interval4, indicating substantial dilution by injected water. Other monitoring locations showed only minor or no discernible EC variations associated with injection events.

Injection water temperatures measured at the ST1 wellhead reached maxima of 69.7°C during the first two hot-water injections, which were conducted continuously over two weeks, and 66°C during the third injection, which followed a daily injection schedule (09:00–17:00). These temperatures were slightly lower than the 73°C produced at the boiler, reflecting heat loss during water transport through the surface infrastructure.

A substantial increase in production temperature was observed at ST1 following each hot-water injection, rising from the pre-injection baseline of 18.4 ± 0.3°C (Figure 26). After the first injection, the outflow temperature increased to a maximum of 21.2°C. The second injection started at 20.5°C, peaking at 24.5°C during the initial bleed-off phase. Over the subsequent 3.5 weeks of production, temperatures declined to 19.7 ± 0.2°C, remaining at 1.3°C above the pre-injection baseline. Prior to the third injection, the baseline temperature remained elevated at 19.0 ± 0.3°C. Following this injection, temperatures reached 23.2 ± 0.2°C and gradually decreased to 19.5 ± 0.3°C over three weeks of production, still 1.1°C above the pre-injection baseline.

At the outflow of MB2-Interval4, a modest temperature increase of approximately 1.2°C was observed, which declined rapidly after hot injection ended. This suggests that most of the injected heat remained localized near the ST1 injection interval. Temperature changes at more distant boreholes (ST2 and GB1) were within measurement uncertainty and cannot be reliably quantified. These findings demonstrate that even **short-term injection cycles can elevate production temperatures from ST1-Interval11 for weeks to months**. Furthermore, heat storage appears to be spatially localized, with minimal thermal impact on hydraulically connected but more distant sites. Decreasing the substantial heat-loss along the non-insulated borehole casing is expected to substantially increase the outflow temperature at ST1.

Changes in pH were comparatively subtle (Figure 27), as the injected water (pH 8.7 ± 0.3) is only slightly more acidic than the native groundwater at ST1 (pH 9.1 ± 0.1), ST2 (pH 9.3 ± 0.2), and MB2 (pH 9.15 ± 0.2). Nevertheless, transient decreases in pH to values as low as 7.7 were observed at ST1 following injection cycles, occasionally dropping below the pH of the injected water. This may indicate biogeochemical processes, such as microbial decomposition of organic matter introduced during injection.

Overall, the observed variations in hydrochemical parameters are consistent with the expected flow pathways within the BEACH reservoir. The data suggests strong hydraulic connections from the injection interval to MB2-Interval4, while more distal monitoring points remain largely unaffected. Our observations suggest that **injection processes influence subsurface geochemical conditions within a confined spatial radius, thereby keeping potential environmental effects localized, at least in our downscaled experimental setup.** Notably, **production temperatures at ST1 remained elevated above the pre-injection baseline for several weeks** after injection, **demonstrating the fractured rock's heat storage capacity** and supporting the FTES concept's feasibility. Improving borehole and surface infrastructure insulation is expected to reduce heat loss during injection and **should be evaluated in future experiments**, particularly with regard to its potential influence on **biogeochemical responses at higher temperatures**. Ongoing analyses of water chemistry, stable water isotopes, and carbon isotopes will provide further insight into geochemical processes associated with heat storage and recovery.

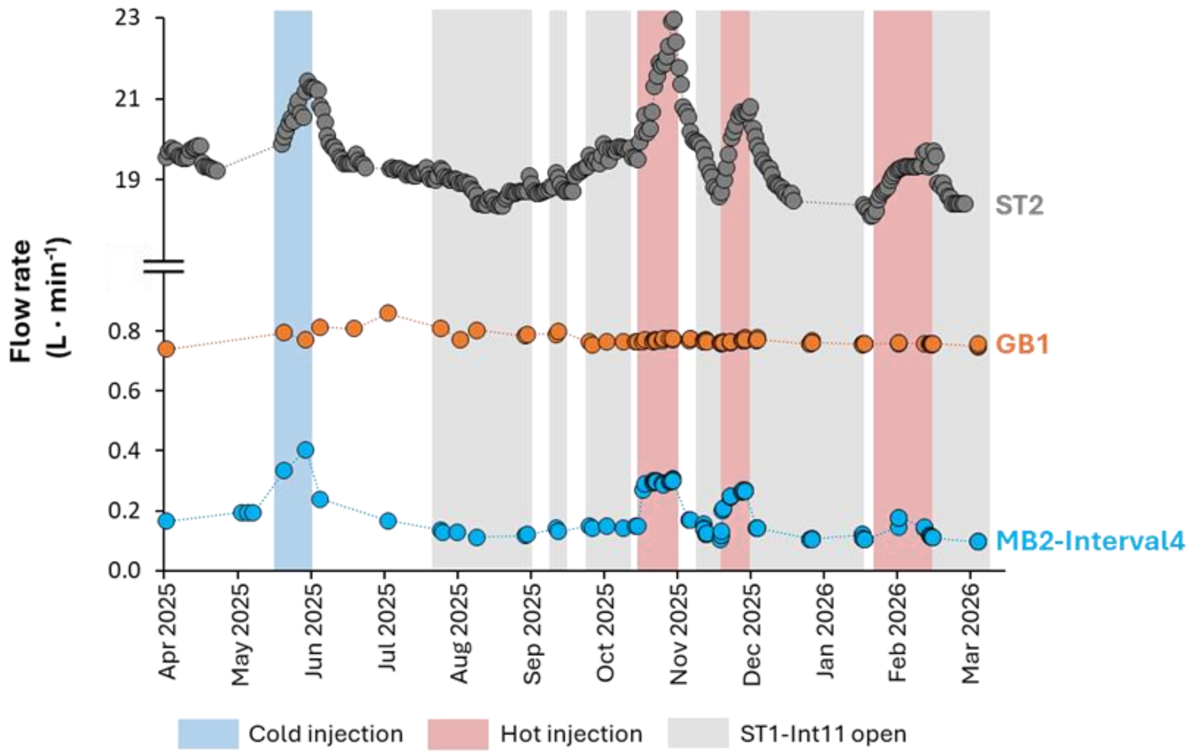

Figure 24: Flow rate at ST2, MB2-Interval4, and GB1 from April 2025 to March 2026. Measurements at MB2 and GB1 were conducted manually, while ST2 is monitored automatically. Time periods of cold and hot water injections and ST1-interval11 bleed-offs are shown with blue, red, and gray backgrounds, respectively.

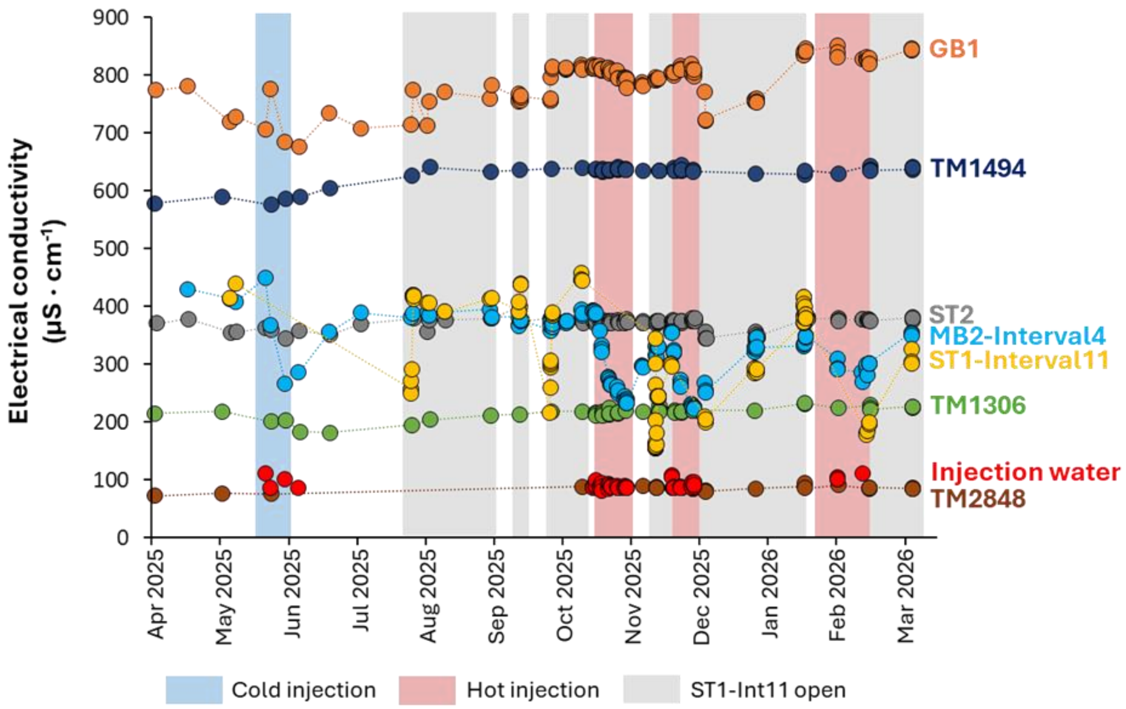

Figure 25: Electrical conductivity of ST1-Interval11, ST2, MB2-Interval4, GB1, TM1306, TM1494, TM2848 and the injection water from April 2025 to March 2026. Measurements were conducted manually using probe HI98129 (HANNA Instruments). Time periods of cold and hot water injections and ST1-interval11 bleed-offs are shown with blue, red, and grey backgrounds, respectively.

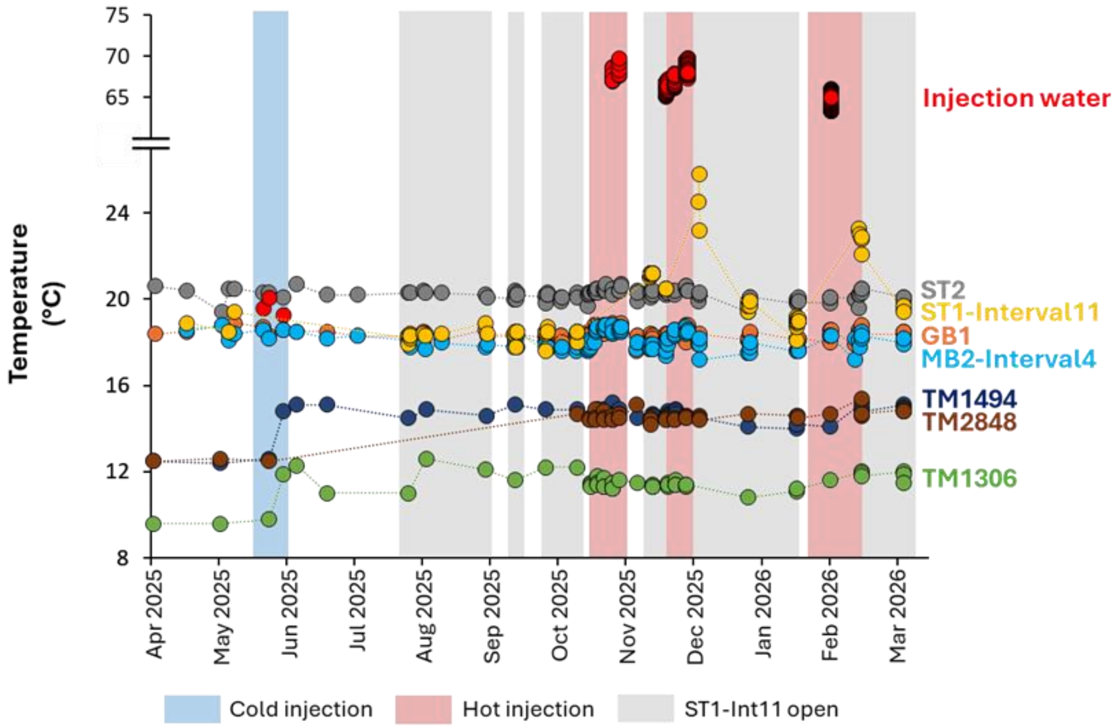

Figure 26: Temperature of outflow water from ST1-Interval11, ST2, MB2-Interval4, GB1, TM1306, TM1494, TM2848 and the injection water from April 2025 to March 2026. Measurements were conducted manually using probe HI98129 (HANNA Instruments). Time periods of cold and hot water injections and ST1-interval11 bleed-offs are shown with blue, red, and gray backgrounds, respectively.

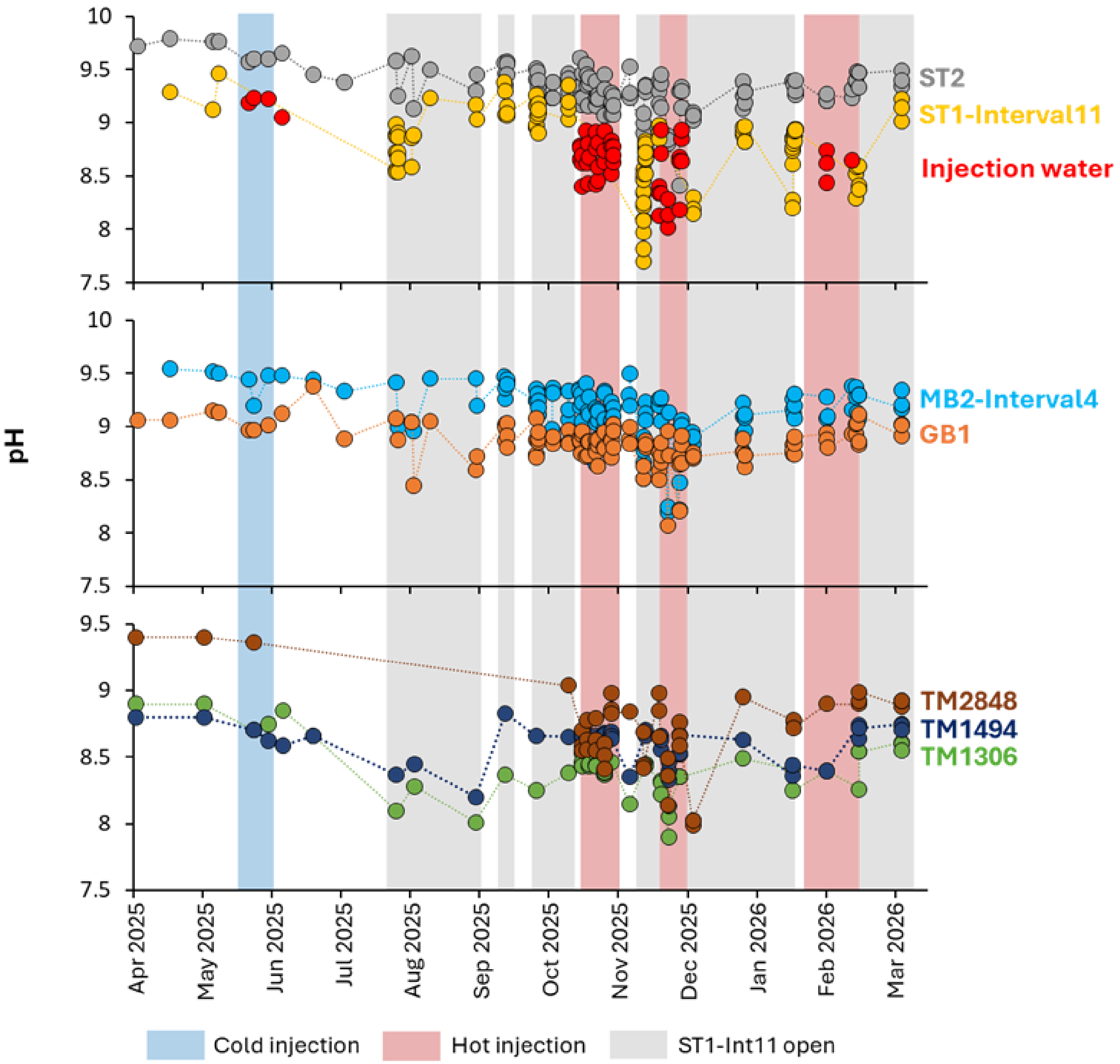

Figure 27: pH of ST1-Interval11, ST2, MB2-Interval4, GB1, TM1306, TM1494, TM2848 and the injection water from April 2025 to March 2026. Measurements were conducted manually using probe HI98129 (HANNA Instruments). Time periods of cold and hot water injections and ST1-interval11 bleed-offs are shown with blue, red, and gray backgrounds, respectively.

3.3.7. Microbiological observations

While hydrochemical parameters indicate mixing with injected water at specific monitoring sites, microbiological monitoring offers biogeochemical insights to assess system responses to cold- and hot-water injections. This monitoring includes both DNA and dissolved organic matter (DOM) extraction.

At present, most microbiological samples are still under analysis, and no results from DNA-based investigations are available yet. However, preliminary results from DOM extraction are available for the cold-water injection conducted in June 2025, whereas analyses for the hot-water injection cycles are still ongoing. DNA and proteins are extracted using a combined phenol–chloroform-based protocol. All samples will be subjected to quantitative PCR to assess microbial abundance, and 16S rRNA gene sequencing to evaluate changes in microbial community composition. Selected samples will be further investigated using metagenomic approaches, and potentially metaproteomics, to gain deeper insight into functional adaptations.

Notably, visible changes were observed in the material collected on filters from ST1-Interval11, whereas no comparable changes were detected in samples from other boreholes (Figure 28). At this stage, these observations suggest an increase in biomass and microbial activity at ST1 following the second and third hot-water injection cycles. To ensure representative sampling, each borehole is flushed for a minimum of 24 hours prior to sampling, thereby minimizing contributions from upstream sections of the borehole.

If confirmed, the apparent increase in biomass after hot injections may be attributed to several factors. Elevated temperatures associated with hot-water injection may promote microbial growth by stimulating thermophilic populations that are dormant under ST1-interval11's ambient conditions and/or by mobilizing nutrients that are otherwise trapped within the surrounding rock, packer, and injection system. The combined heat, pressure, and oxygen accompanying injection may additionally kill the in situ microbial community, providing a new source of organic matter (e.g., necromass) to the carbon-limited ST1 ecosystem and promote the proliferation of fast-growing, injection-stress-resistant heterotrophic microorganisms. Microbial heterotrophic activity can help explain the decrease in pH observed at ST1 and may further enhance biomineralization processes through increased activity of iron- or manganese-reducing bacteria. This could explain the formation of the reddish-brown precipitates observed on the filters. Ongoing analyses will provide further clarity on these aforementioned processes.

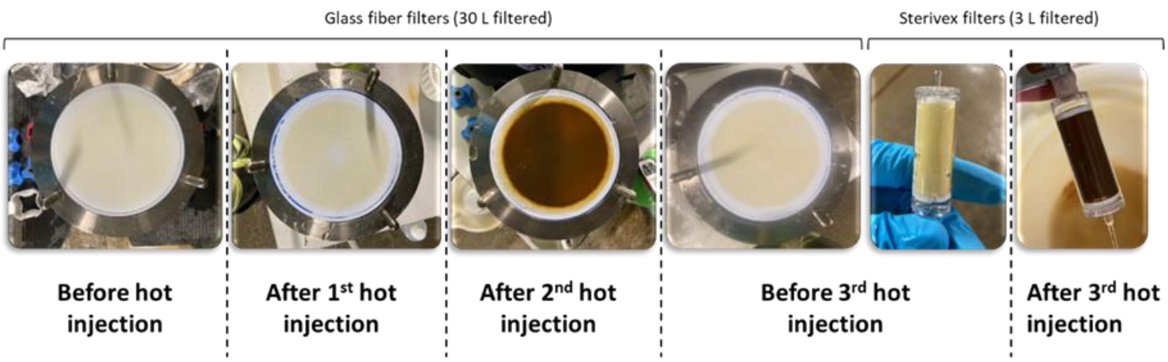

Figure 28: Visible increase in biomass and organic particles in the outflow water from ST1-Interval11 after 2nd and 3rd hot water injections. Glass fiber filters with a pore size of 0.3 µm are used to separate the total organic carbon into particulate and dissolved fractions. Sterivex filters (0.2 µm pore size) are used for combined DNA and protein extraction.

Figure 29 presents preliminary results from high-resolution mass spectrometry analyses of dissolved organic matter (DOM) for samples collected before, during, and after the cold-water injection from 3–18 June 2025. DOM monitoring was conducted at ST1-Interval11, MB2-Interval4, ST2, GB1, and in the injection water. More distant locations were not included in this dataset.

Principal component analysis (PCA) indicates that the DOM composition of the injection water differed markedly from that of the native groundwater at ST1, MB2, and ST2 (Figure 29A). In contrast, the injection water showed greater similarity to GB1, which may reflect a stronger influence of surface-connected flow paths at both locations. ST1 and MB2 form a close cluster, consistent with their known hydraulic connectivity, whereas ST2 exhibits a more distinct DOM signature.

Comparison of pre- and post-injection samples showed a pronounced shift in DOM composition at MB2 toward the injection water signature, followed by a gradual return toward baseline conditions by late August. ST2 exhibited a similar but less pronounced response. At ST1, DOM composition also changed following injection and partially returns toward pre-injection conditions over time. In contrast, GB1 showed variability but no clear injection-related trend. These observations were consistent with changes in hydrological parameters and support the inferred connectivity between monitoring sites.

In addition, the number of compounds shared between the injection water and groundwater DOM pools increased at MB2 and ST2 during the injection period, followed by a decrease after injection ceased (Figure 29B). This pattern supports the temporary introduction and subsequent attenuation of injection-derived organic compounds. A similar trend is observed at GB1; however, interpretation is more uncertain, as its DOM composition is inherently more similar to that of the injection water, suggesting potential overlap in source contributions.

Compound class analysis indicated that MB2 is characterized by a relatively high proportion of unsaturated hydrocarbons, which are also present at ST1 and appear to be diluted during injection Figure 29C). These compounds may originate from anthropogenic but also microbial sources. GB1 and the injection water contain a notable fraction of peptide-like compounds, which may derive from the degradation of sedimentary organic matter or from surface infiltration. The presence of lipid-like compounds across all samples is consistent with ongoing microbial activity within the Bedretto groundwater system.

Overall, the DOM data revealed distinct, injection-related shifts in organic compound distributions, supporting the transport and mixing of injection-derived organic matter within the fractured rock system. These results demonstrate the potential of DOM analysis as a tracer for flow paths and mixing processes. Notably, the **system shows recovery to near baseline conditions within approximately two months following cold injection, suggesting that the observed perturbations are not permanent**. Data from the first and second hot-water injection campaigns are currently under analysis and will provide further insight into DOM dynamics under elevated temperature conditions. As these results are preliminary, **further analyses**, including the combined evaluation of DOM composition and DNA-based microbial data, **are required to robustly assess subsurface microbial activity and its response to injection, particularly over longer injection cycles and at higher injection temperatures**.

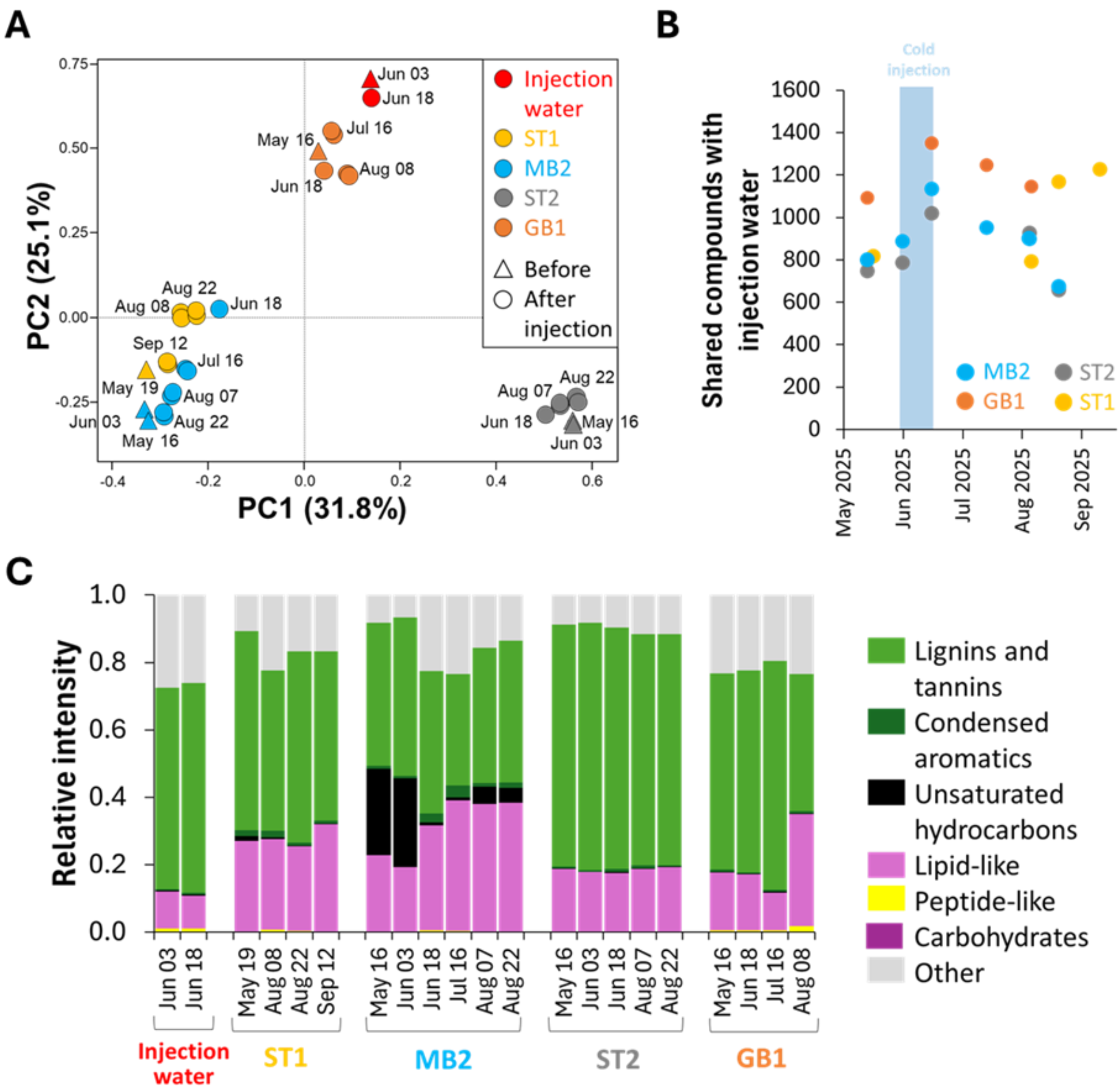

Figure 29: Changes in the dissolved organic matter (DOM) pool during cold water injection in ST1-Interval11. A: Principal component analysis (PCA) based on the DOM composition between May and September of 2025 in ST1-Interval11, ST2, MB2-Interval4, GB1, and the injection water. Triangles depict samples taken prior to cold water injection; circles depict samples taken afterward. B: Number of compounds that were shared with the injection water DOM pool. C: Relative abundance of compound classes over time. Chemical classes were assigned based on C, H, O, and N contents of individual organic compounds.

3.3.8. Self-Potential (SP) measurements

Figure 30 shows filtered self-potential (SP) amplitudes at selected electrode locations along the tunnel, together with injection flow rate and pressure. The SP signals exhibit temporal variability over the monitoring period and observed trends differ between electrode locations. The SP dataset will be further analysed to reach more conclusive findings.

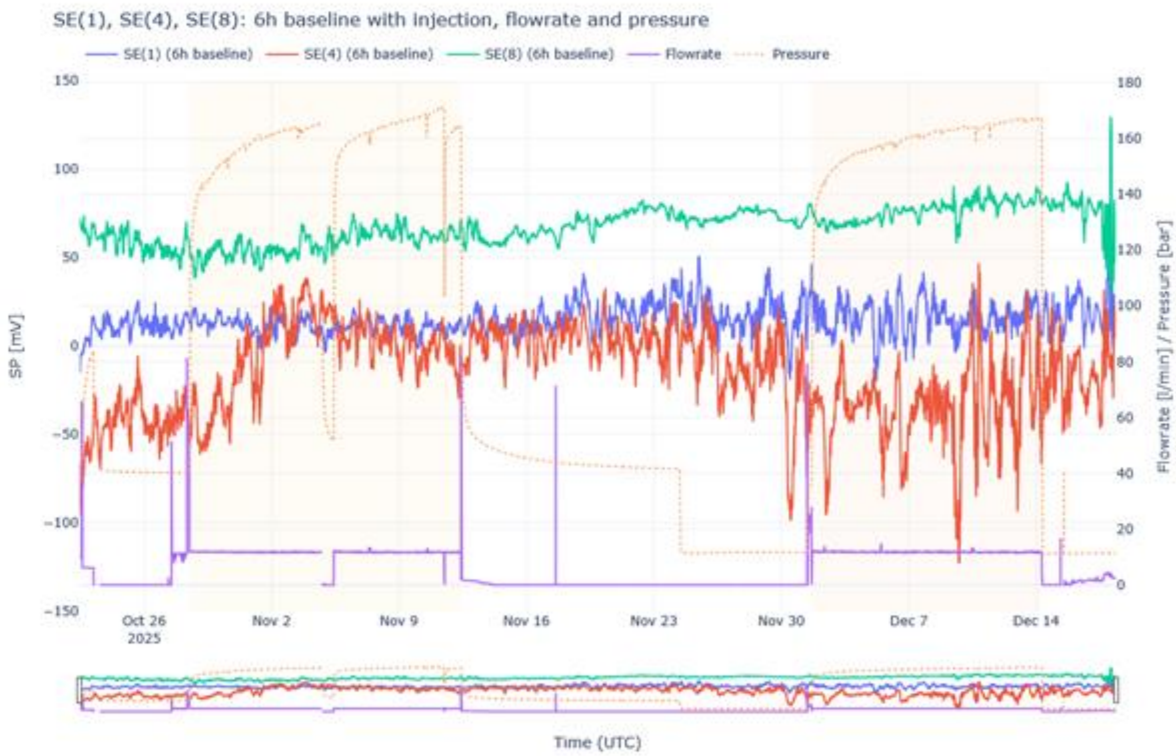

Figure 30: Filtered self-potential (SP) time series at selected electrode locations (SE(1), SE(4), SE(8); see Figure 15) along the tunnel, shown together with injection flow rate and pressure. SP signals are referenced to electrode N95 and processed using a 6-hour moving median baseline.

3.3.9. Seismicity

Figure 31 shows the seismicity that occurred during the experiments. A total of 1828 events were recorded with the experimental network and 96 events with the permanent network during the experimental sequence. During the cold water injection, about 300 events were recorded, which is about 20 per day. During the hot water injection 1 and 2, 80 and 100 event were detected, respectively which is only 5 – 10 events per day. Interestingly, seismicity seemed to decrease during hot water injections, a phenomenon that has yet to be analysed. The largest events recorded have magnitude of ~MLc -2.3, which is well below any alarm thresholds.

The seismicity is located around the injection ST1-interval 11 and reaches beyond the high-resolution borehole-based monitoring network. The seismicity clouds corroborate with seismicity clouds induced during past experiments performed in ST1-interval 11, with a tendency to propagate upwards. Sparse seismicity also occurs outside the main seismicity cloud.

Even though injection pressure was kept below jacking pressure, the pressure levels of 16 MPa are still considerable and obviously able to induce seismicity. **Even though seismicity rates are very low, its occurrence stress the need for seismic monitoring and altering during the pilot phases of FTES.**

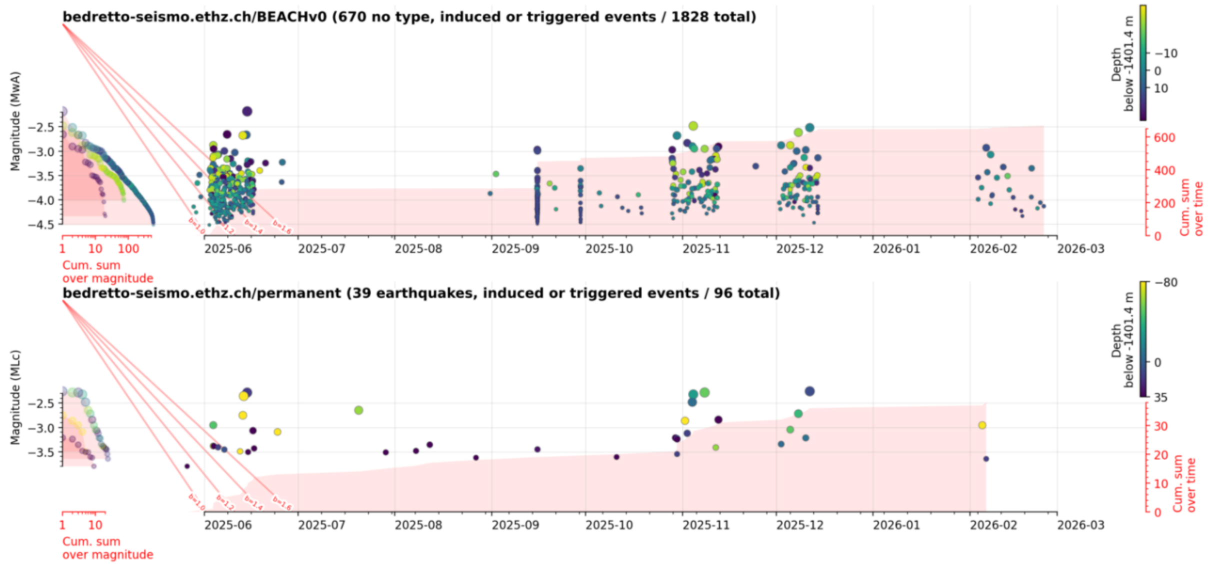

Figure 31: Evolution of seismicity between June 2025 and February 2026 as recorded with the experimental network (top) and the permanent network (bottom). The primary vertical axes are the magnitudes MwA (experimental network) and MLc (permanent network) The figure includes the frequency magnitude distributions as well as the number of events recorded during the experiment sequence. Color scale of the events corresponds to vertical depth.

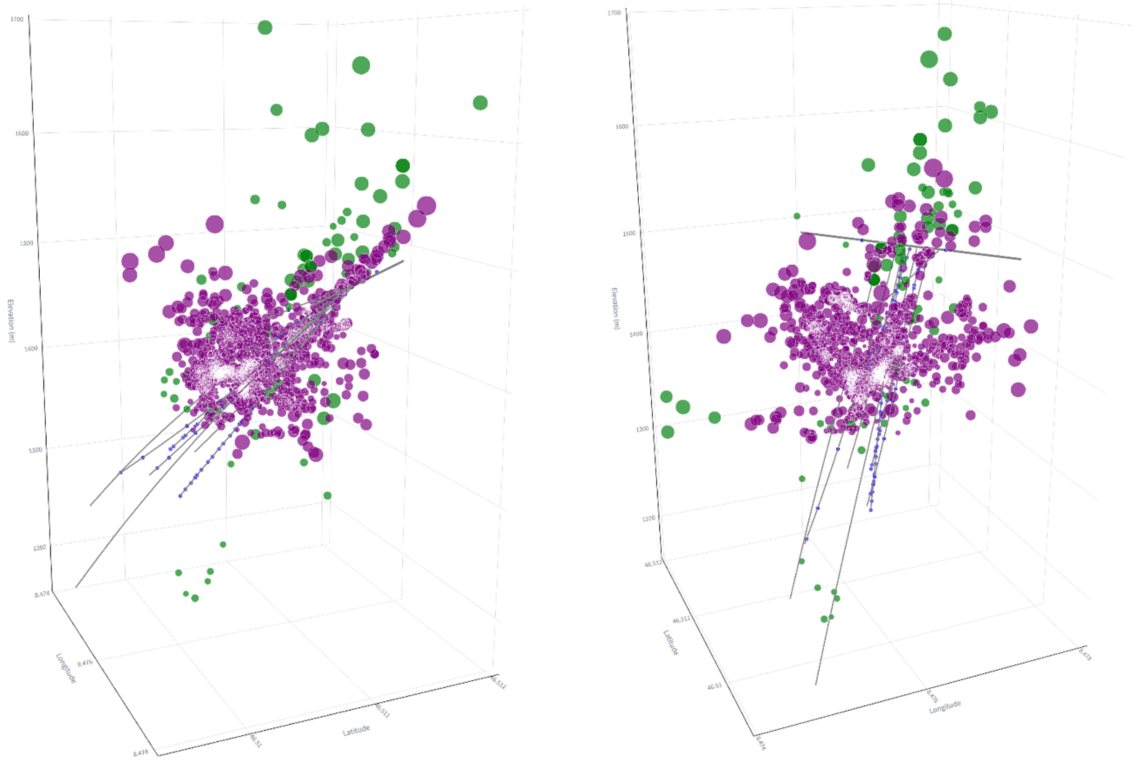

Figure 32: 3D views of the seismicity recorded during the BEACH injections. Purple events were recorded with the permanent network, green events with the experimental network.

3.3.10. Distributed Acoustic Sensing (DAS) monitoring

DAS data were examined using the seismic event catalogue from the BEACH injection experiments (Figure 33). The catalogued events that occurred after the increase in DAS sampling frequency to 2000 Hz (Figure 34) were inspected in the DAS recordings. Two events could be identified, corresponding to earthquakes with magnitudes MwA −2.61 and −2.88. Wavefield propagation along the fibre is observable over source–receiver distances of up to approximately 60 m (Figure 35), though only within borehole MB3. The detectability of smaller-magnitude events is limited by the achievable temporal sampling frequency, while detection of more distant events is primarily constrained by a signal to noise ratio (SNR) approaching the instrumental noise floor. These observations demonstrate that DAS can effectively complement conventional borehole seismic monitoring systems, providing dense spatial sampling from a single sensing unit and enhancing overall monitoring coverage. The observations also underscore the role of the acquisition design, with future experiments targeting higher sampling rates to achieve improved detection capabilities on DAS recordings.

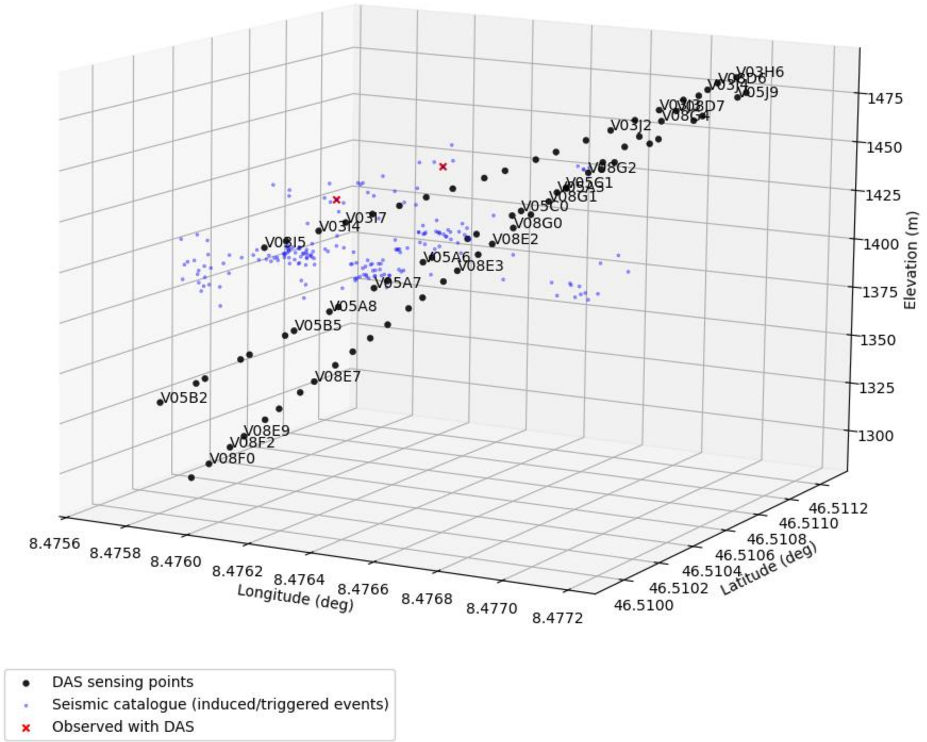

Figure 33: 3D spatial distribution of DAS sensing points with station names (black circles) including the seismic catalogue (blue dots) and events observed with DAS (red crosses).

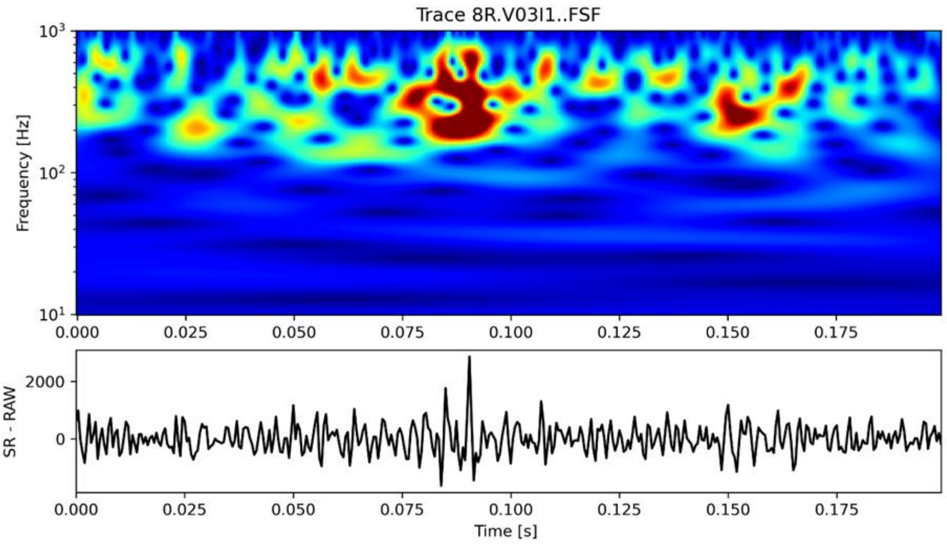

Figure 34: Time–frequency analysis of a DAS channel in MB3, showing the spectrogram (top) and the corresponding raw strain-rate signal.

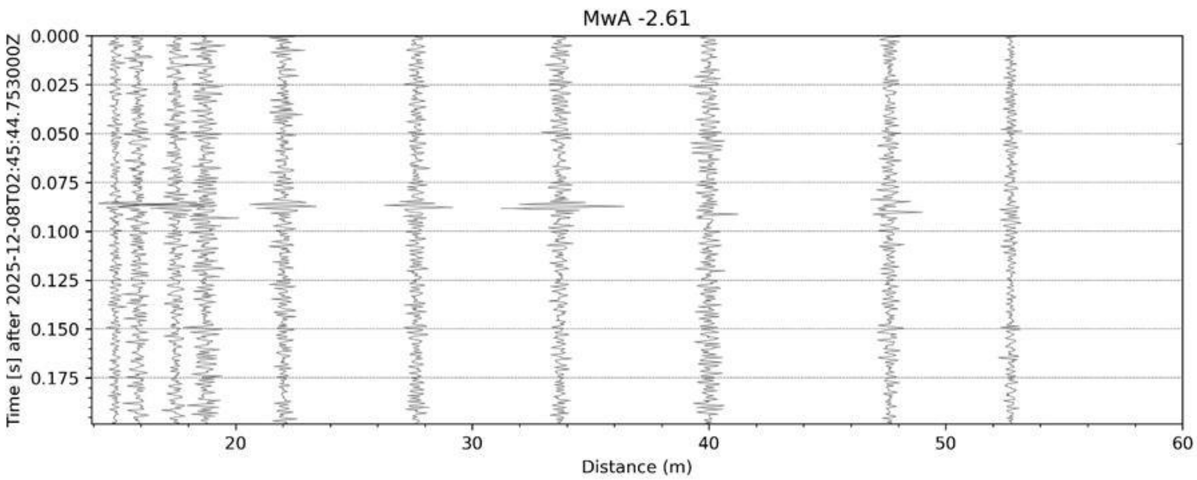

Figure 35: DAS strain-rate waveforms for a MwA –2.61 microseismic event plotted against source-receiver distance for DAS channels in MB3, illustrating coherent arrivals across the sensing array.

3.4. Summary of heat storage experiments

- The experiments successfully demonstrated the technical feasibility of storing thermal energy in fractured crystalline rock under in situ conditions. Water was heated up to 80 °C in a boiler and injected into a borehole interval at 132 – 150 m depth, where a fraction of the thermal energy was effectively stored within the connected fracture network and subsequently recovered.
- As expected, substantial thermal losses occurred along the injection lines in the tunnel (33%) and along the borehole (45%), resulting in maximum temperatures of 33 °C at the injection interval (i.e. 12 °C above ambient temperature level). These losses are attributed to the lack of thermal insulation and represent a known, non-optimized boundary condition of the experiment.
- At the reservoir (interval) level, thermal recovery efficiency increased from approximately 6% in the first cycle to >10% in the second cycle (for comparable production periods), providing clear experimental evidence of improving performance with repeated cycling. It is important to note that ST1

outflow temperature stayed elevated for almost two months after production, showing fractured rock heat storage and supporting FTES feasibility.

- Despite the heat losses in the tunnel and in the borehole and the short duration of the injection cycles, the observed increase in recovery efficiency demonstrates progressive thermal conditioning of the reservoir, a behaviour consistent with subsurface heat storage systems world-wide and indicative of improved performance with continued operation.
- Achieving economically relevant efficiencies will require both upscaling to larger injection rates and larger reservoirs, and improved reservoir access through optimized interval design. In particular: (1) the borehole segment above the injection interval must be thermally insulated; (2) the interval length should be optimized to give access to a larger fracture network and eventually to more transmissivity structures; (3) the unload (production) is expected to significantly enhance performance by using a downhole pump (forced production instead of production exposed to atmospheric conditions); (4) a multi-borehole setup (e.g. standard dipole cross-hole setup or using several production boreholes surrounding a central injection borehole) will also enhance efficiency significantly. These optimization strategies can be systematically evaluated through a combination of calibrated numerical modelling (see Section 4) and further experimental work (see Section 5).
- The experiments were supported by a comprehensive, multi-parameter monitoring system, ensuring safe operation— particularly with respect to induced seismicity— and providing a detailed dataset for process understanding and model validation. Key observables include temperature distributions derived from DTS and deformation patterns from DSS highlighting fracture flow, as well as tracer and geochemical and microbiological parameters addressing environmental changes in the reservoir.
- DTS and pressure observations show no evidence of thermal breakthrough to surrounding monitoring boreholes, indicating that heat transport remains confined to the near-field fracture network around the injection interval. This confirms that thermal energy is effectively retained within the target reservoir volume rather than being lost to the far-field, which is a key requirement for efficient thermal energy storage.
- Seismic monitoring (complemented with DAS) achieved high sensitivity, detecting events down to magnitudes $M_w<-4.0$. A dedicated seismic duty service ensured that any significant events would have been promptly identified and managed to maintain operational safety. Observed seismicity remained confined to previously identified fracture zones, consistent with known flow pathways.
- Hot-water injections had only minor impact on reservoir geochemistry of the reservoir, while microbiological communities exhibited temporary changes during injection but rapidly returned to pre-injection conditions, indicating limited long-term environmental impact.
- The impact of hot-water injections on water chemistry effects seems to be localized, suggesting the environmental impact is limited to a small radius. The system showed recovery within two months after cold injection, indicating no permanent alteration (Hot injection data is pending). Longer and higher-temperature injection cycles (i.e. through improved insulation) require further monitoring to assess long-term system changes.

4 Modelling of heat storage experiments

4.1. Hydraulic characterization

The hydraulic properties of the formation control the achievable injection rates, the pressure response, and the radius of influence of any injection or pumping within the reservoir. For these reasons, particular emphasis was placed on obtaining a robust and internally consistent characterization of the hydraulic properties of Interval 11 in ST1.

An inverse modelling approach was adopted. A numerical finite-difference model was developed to simulate Darcy flow within a discretized equivalent porous medium under Neumann boundary conditions. The model was calibrated by matching simulated responses to observed pressure and flow data. This calibration procedure was repeated across several hydraulic tests performed at different times. The final parameter set corresponds to values that are consistent across all tests, while also accounting for the operational history of Interval 11, in particular the stimulation campaigns carried out between 2022 and 2024.

The analysis was divided into two parts:

- (A) near-field properties, which control the short-term response of the well,
- (B) far-field properties, which govern long-term behavior during sustained injection.

4.1.1. Near-field assessment

Near-well properties were calibrated using multiple hydraulic tests. The constant-rate injection test of 28 October 2025 was selected as the most representative dataset for estimating transmissivity (m^2/s) and storage coefficient (-).

Initial interpretations, assuming a homogeneous reservoir, yielded a transmissivity of 1.4E-7 m^2/s and a storage coefficient of 1E-4. However, this storage coefficient is unrealistically high and does not match field observations. Such a value would imply a very limited radius of influence that should not extend to the observation wells (MB2 and ST2), whereas a clear hydraulic response is observed in both wells. To resolve this inconsistency, a higher-transmissivity zone was introduced around the well. This “stimulated zone” significantly improves the match between model and data and is consistent with the known stimulation history of Interval 11. It is interpreted as the result of the stimulation activities carried out by ETH between 2022 and 2024.

With this approach (Figure 36; Figure 37), the background formation transmissivity is estimated at 7.8E-8 m^2/s, with a storage coefficient of 2E-6. The stimulated zone extends approximately 15 m from the well and is characterized by a higher transmissivity of 4.5E-7 m^2/s, while maintaining a similar storage coefficient. This radial extent is consistent with the spatial distribution of induced microseismicity observed during stimulation operations in 2023, providing independent support for the model structure.

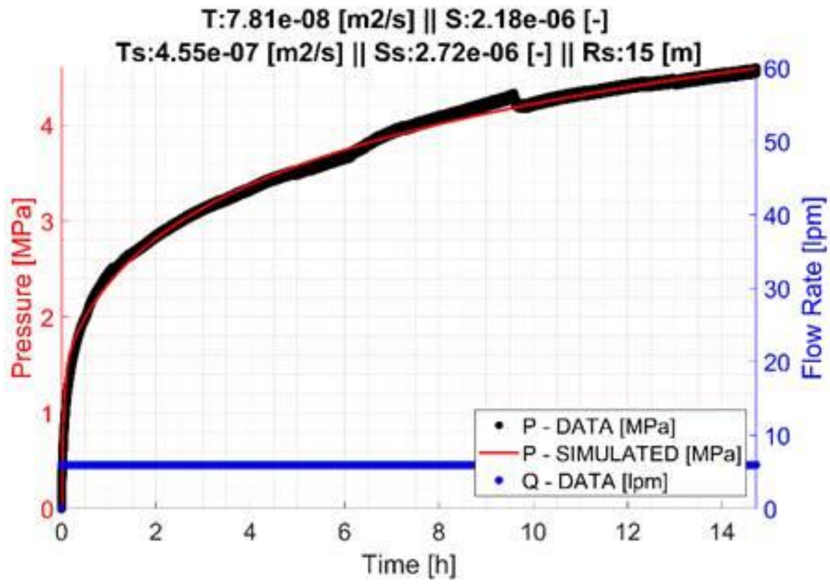

Figure 36: Pressure response during the 28.10.2025 constant-rate injection test used for near-field calibration. Measured pressure (black) is compared with the simulated response (red), showing good overall agreement. The model incorporates a dual-zone structure, consisting of a higher-transmissivity stimulated zone near the well and a surrounding intact granite domain. The constant injection rate is shown in blue.

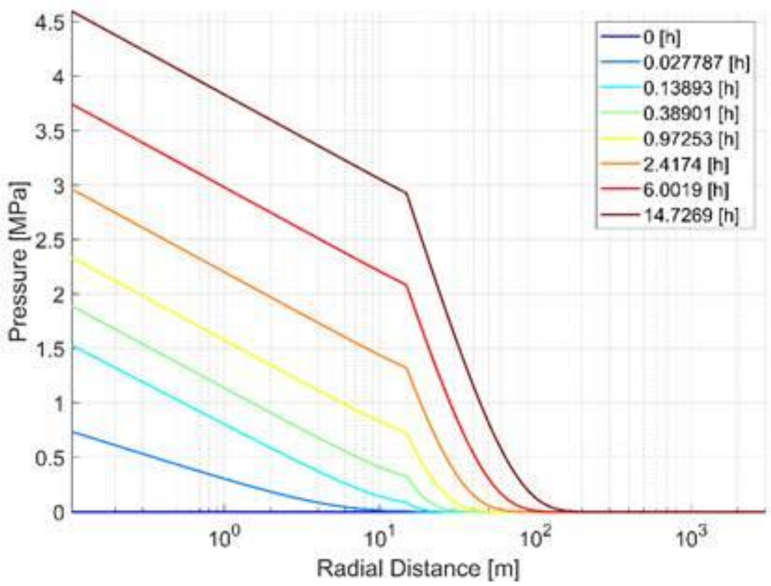

Figure 37: Simulated radial pressure distribution at selected times for the calibrated near-field model. The curves illustrate the temporal evolution of the radius of influence and highlight the dominant role of the stimulated zone in controlling early-time pressure propagation.

4.1.2. Far-field assessment

Far-field behavior was analyzed using data from the first hot water injection, during which fluid was injected into ST1 at a constant rate of 12 L/min. During this period, the observation well ST2 remained open, and an increase in outflow of approximately 3 L/min was recorded after 15 days of continuous injection. The open condition of ST2 (i.e., a sink) imposes a persistent pressure gradient across the reservoir that significantly influences the pressure response observed in ST1.

Simulations based solely on the near-field calibrated parameters reproduce the early-time pressure response because it is mainly controlled by the accounted wellbore storage (not reported here for the sake of brevity) but deviate from the observations at late times (Figure 38). This mismatch is attributed to the unaccounted influence of ST2. When ST2 is explicitly included in a two-dimensional model, the agreement improves significantly. The model is then able to reproduce both the pressure evolution in ST1 (Figure 39) and the measured outflow at ST2 (Figure 40) using a similar parameter set. This highlights the critical importance of inter-well hydraulic connectivity in controlling system-scale behaviour.

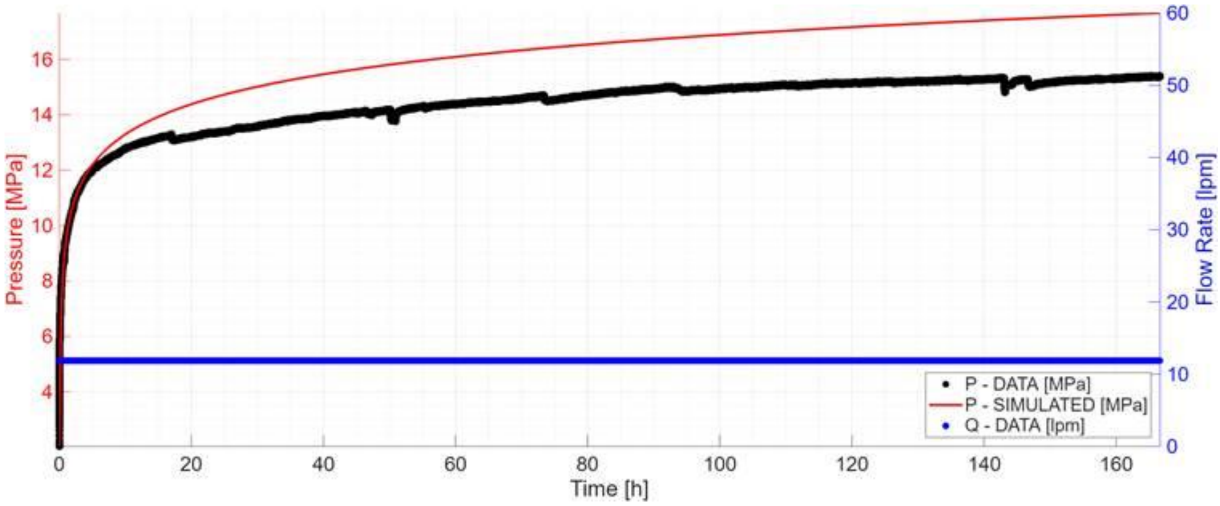

Figure 38: Pressure response during the first hot-water injection, simulated using near-field parameters only. Measured pressure (black) is compared to the simulated response (red). While early-time behaviour is reasonably captured, the model overestimates pressure at late times, indicating that additional boundary effects are not accounted for.

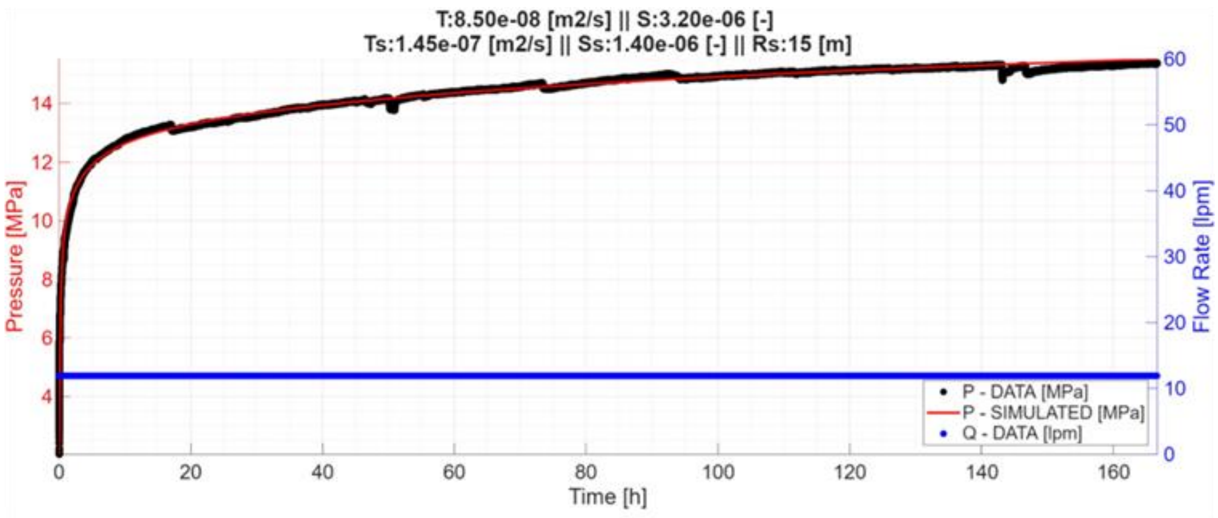

Figure 39: Pressure response during the first hot-water injection. Incorporating the persistent sink of ST2 in the model significantly improves the agreement between measured (black) and simulated (red) pressure over the full duration of the test.

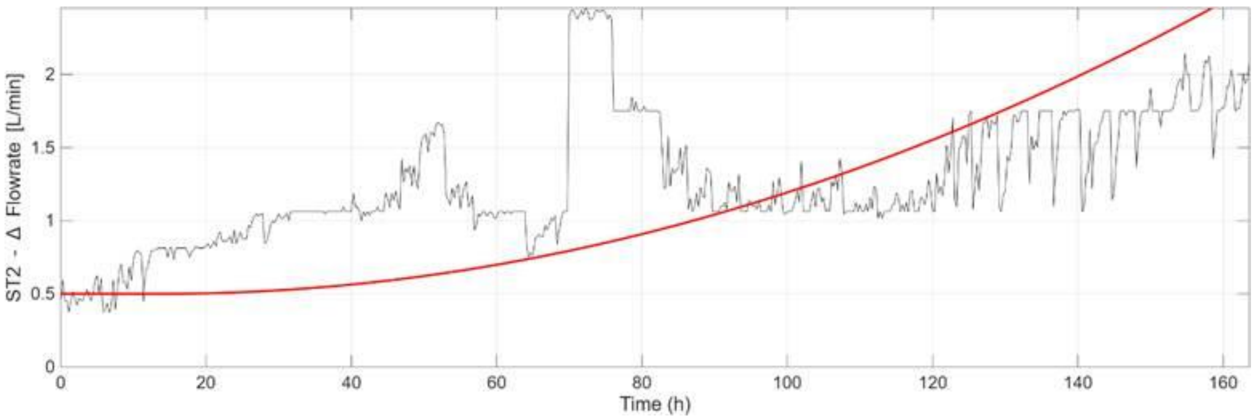

Figure 40: Measured change in outflow at ST2 during the first hot-water injection (black), compared with the simulated response (red). The outflow was not used for calibration and therefore provides an independent validation of the model. The overall agreement supports the correct representation of inter-well connectivity in the simulation.

4.2. Discrete fracture network models

We undertook a discrete fracture network (DFN) model approach to replicate the heat storage experiments. This modelling was itself broken up into two separate models: a) a wellbore heat loss model and b) a DFN model of the reservoir. The DFN model was then used to derive storage efficiency projections using the calibrated reservoir behaviour.

4.2.1. Simplified Wellbore Heat Loss Model

The wellbore model was developed to test the hypothesis that the measured temperatures in Interval 11 were the result of wellbore heat loss rather than heating of the surrounding rock mass. The heat loss in ST1 and the heating of wellbores MB5 and MB3 near the surface suggest that heat loss along the wellbore is significant (see also Section 3.3.4). A simplified model was developed, as shown in Figure 41.

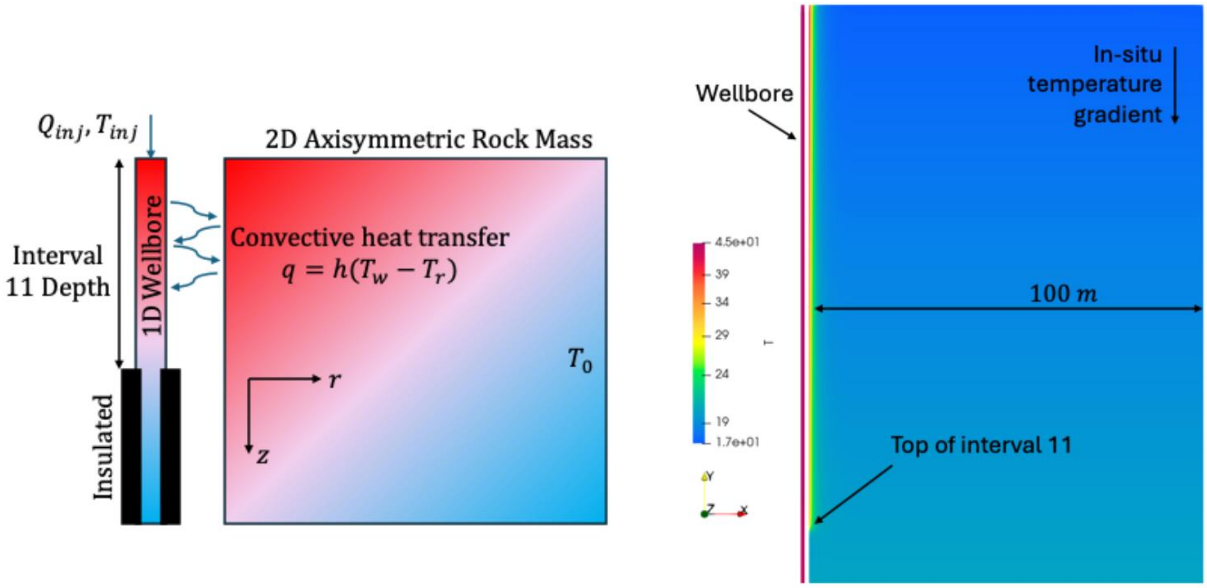

Figure 41. Conceptual diagram of simplified wellbore model and the thermal heating layer developing in the surrounding rock due to convective heat transfer along the wellbore.

In the simplified model, a one-dimensional wellbore exchanges heat with a two-dimensional axisymmetric isotropic and homogeneous rock mass. Heat transfer in the wellbore is transient and advection-dominant, while heat transfer in the rock mass is driven only by conduction. Heat transfer between the two domains is governed by a convective boundary condition, such that the flux is equal to $q = h(T_w - T_r)$, where h is the heat transfer coefficient, T_w is the mean temperature of the fluid over the horizontal cross section, and T_r is the temperature of the rock mass at the rock-borehole interface.

Figure 41 shows the resulting temperature distribution, in which a thin thermal boundary layer develops around the wellbore in the rock mass. The model is solved using the finite element method. Figure 42 illustrates the idealized flow rate compared to the measured flow rate. Fluid is injected at a constant temperature T_{inj} = 55°C, assuming some heat is lost between the boiler and the wellbore. Table 3 illustrates the adopted material parameters, all of which are standard and expected values for the rock mass. The heat convection boundary condition is adopted from the empirical Dittus-Boelter equation for the Nusselt number for turbulent flow through a pipe, $Nu = \frac{hD}{\lambda_f} = 0.023 Re^{0.8} Pr^{0.4}$, in which Re is the Reynolds number and Pr is the Prandtl number.

Table 3. Fitted and standard material properties and boundary conditions for DFN and simplified wellbore models.

Property	Symbol	Value	Property	Symbol	Value
Fluid density	ρ_f	980 kg / m^3	Rock density	ρ_m	2600 kg / m^3
Fluid heat capacity	c_{pf}	4180 J / kg °K	Rock heat capacity	c_{pm}	**800 J / kg °K**
Fluid thermal conductivity	λ_f	0.65 W / m °K	Rock thermal conductivity	λ_m	**3 W / m °K**
Fluid viscosity	μ	0.9 mPa s	Porosity	ϕ	0.02
ST1 diameter	D	0.2 m	Matrix compressibility	C_m	3.8×10^{-8} kPa^{-1}
Surface temperature	T_{surf}	17.2 °C	Geothermal gradient	G	0.02°C/m
Fracture transmissibility	Tr_f	**6.02×10^{-15} m^3**	Matrix permeability	k_m	**0.08 mD**

**Fitted parameters are bolded.*

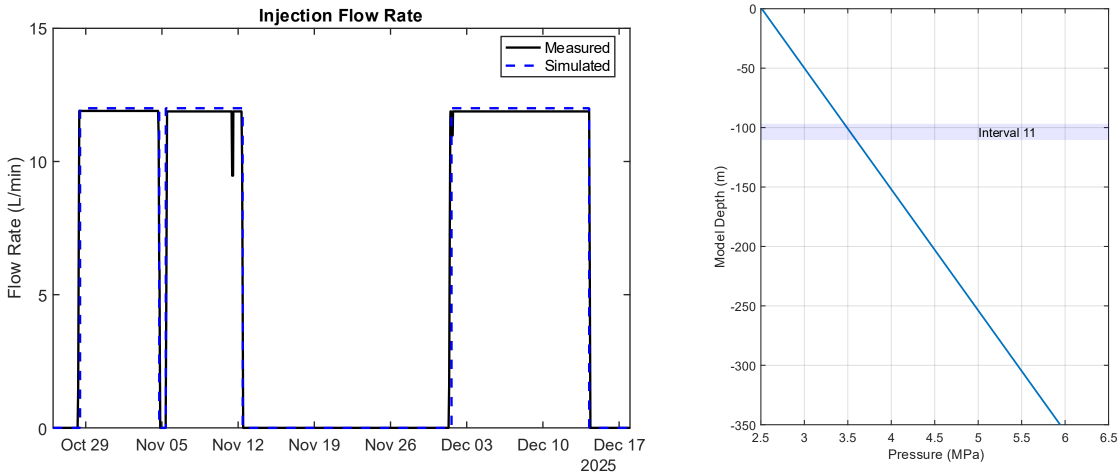

Figure 42. Hydraulic initial and boundary conditions. The flow rate is compared to the real measured flow rate in the left panel.

Figure 43 shows the temperature distribution in the rock mass (i.e. along borehole MB5) as well as the temperature profile at the rock-wellbore interface in ST1 at two representative time steps. The simulated distributions are qualitatively similar with generally good agreement with measured temperatures, but the slope of temperature decline along the injection borehole is steeper in the measurements, particularly during the shut-in period, suggesting a slightly higher heat flux into the rock mass than modeled by pure conductive heat transfer.

We further validate the model using measurements from the nearby borehole MB5, as illustrated in Figure 43. The temperature variations in MB5 are much smaller than in ST1, the temperature change (ΔT_r) is plotted instead of absolute temperature. The agreement is less accurate than for ST1, several important insights emerge. First, from 0 to -90 m, the temperature increase is underestimated, indicating that conduction alone cannot explain the observed heat transport, and suggesting the presence of an advective heat flux, potentially driven by either coupled hydrothermal buoyancy or thermo-mechanical pressurization. Between -90 and -130 m, the agreement with the measured temperature is generally good, implying that conduction dominates in this interval. From -130 to -150 m, temperature increases again, indicating a localized hot spot that cannot be explained by conduction alone. Below the injection interval, the temperature profile is unperturbed.

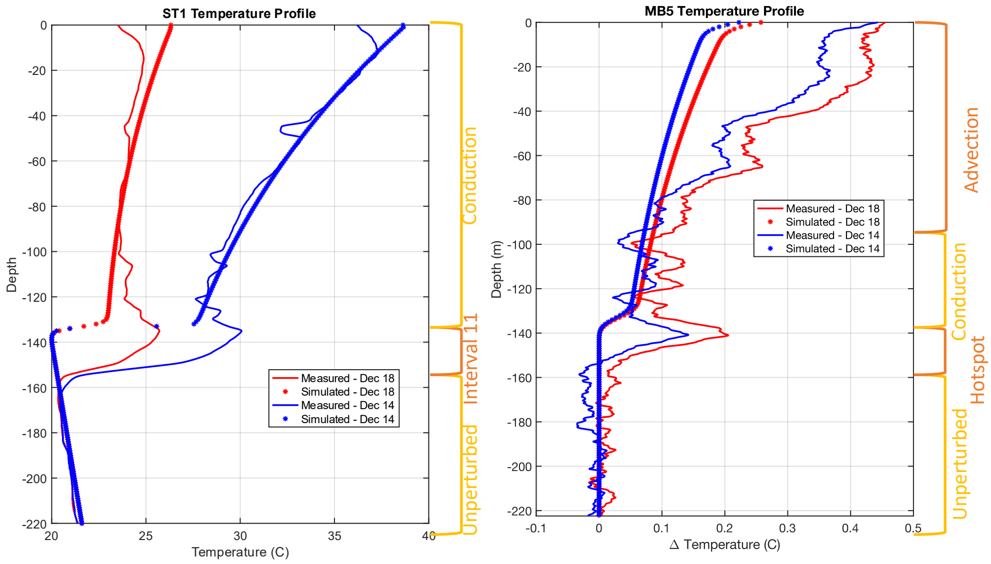

Figure 43. Measured and simulated temperature profiles in ST1 and MB5 using the simplified wellbore model at selected times. Temperature changes in are shown for MB5 due to the small amplitude of variations with respect to the temperature gradient.

Figure 44 shows the temperature at the top of the injection interval (132 m depth) compared to downhole measurements behind the casing, along with the mean fluid temperature. The slopes during injection periods are similar, but the model overestimates cooling during shut-in periods, which again suggests an increased thermal storage capacity over the modeled rock mass. The wellbore fluid temperature, representing the cross-sectional average, is also shown. The fluid in the wellbore cools radially such that the center is hotter than the rock surface, resulting in a mean fluid temperature that is higher than measured at the wellbore-rock mass interface. This mean fluid temperature is later used as the injection temperature into the DFN reservoir model.

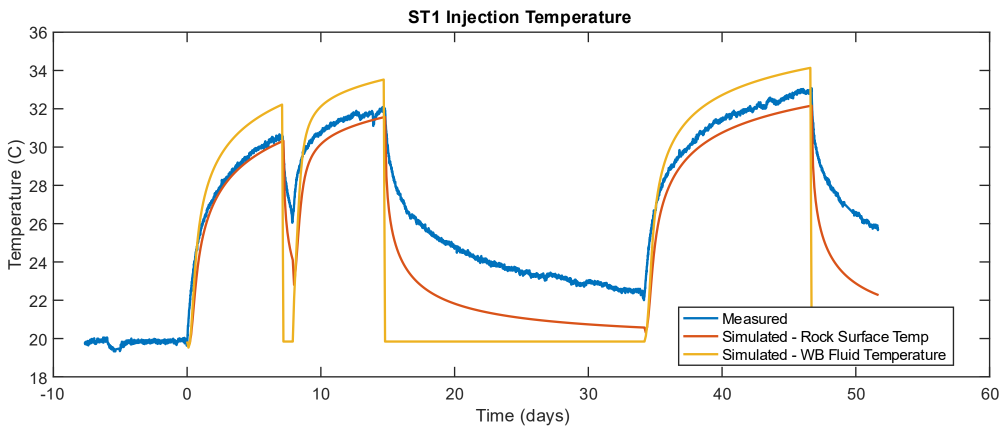

Figure 44. Measured and simulated temperature at the top of Interval 11 in ST1 using the simplified wellbore model. The rock surface temperature represents the temperature at borehole wall, while WB fluid temperature corresponds to the cross-sectional average fluid temperature.

Overall, this model confirms that the temperatures measured in ST1 are primarily governed by conductive heat losses through the borehole wall, as evidenced by the good agreement with measured temperatures both qualitatively and quantitively and in both time and space. At the same time, the model also provides physical insights that advective fluxes are likely present at shallow depths near the tunnel, and that the effective thermal storage of the rock mass may be exceed that predicted by a homogeneous and isotropic representation. Next, we will examine the reservoir-scale behaviour using the injection temperature derived from this wellbore model as the inlet boundary condition.

4.2.2. Discrete Fracture Network (DFN) Reservoir Model

Next, the reservoir behaviour was modelled using a discrete fracture network (DFN) model in CMG STARS. The rock mass is represented as a hydro-thermally coupled homogeneous, isotropic porous medium intersected by high-permeability fracture planes. Temperature-dependent couplings, such as temperature-dependent viscosity, are neglected to reduce the system to a one-way coupled system (hydro → thermal), thereby simplifying the calibration to the experimental data. The wellbore is also discretized to account for pressure losses, but no thermal interaction with the surrounding rock mass is included, and the wellbore geometry is not explicitly represented within the reservoir domain.

Figure 45 illustrates the reservoir boundaries and DFN geometry. The discrete fractures are modelled as planes of best-fit derived from fracture mapping along ST1 generated within the VALTER project. A reservoir domain of 300 × 300 × 350 m is adopted, with significant mesh refinement around the injection interval to accurately capture the thermal boundary layers that developing around the fractures and the injection interval. Figure 42 illustrates the in-situ pressure gradient, while the temperature gradient was neglected and a uniform initial temperature of $20°C$ was assumed for simplicity. Prescribed pressure and temperature boundary conditions are imposed at the domain boundaries. The injection flow rate illustrated in Figure 42 is applied using the wellbore fluid temperature from the simplified wellbore model (Figure 44). The material properties are identical to the simplified wellbore model, documented in Table 3.

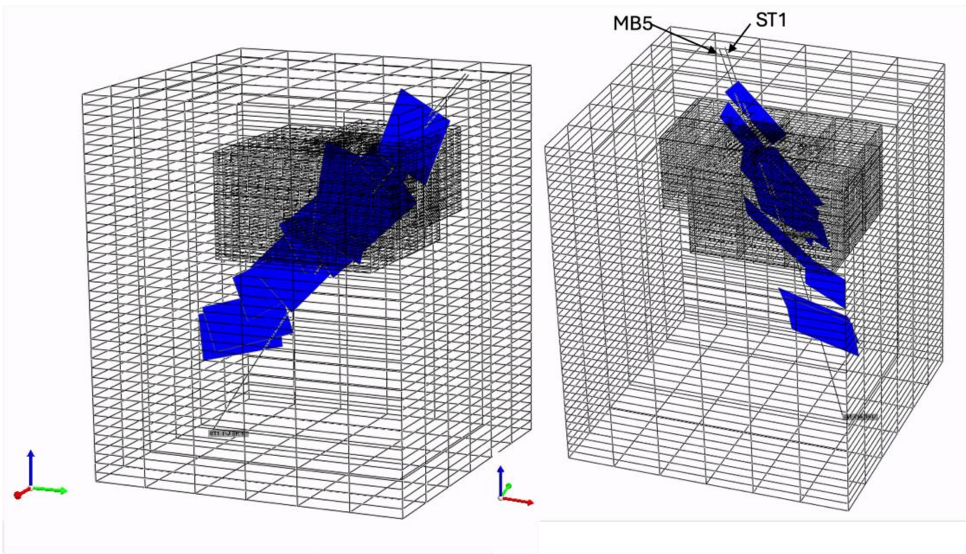

Figure 45. Discrete fracture network reservoir model with ST1 injector well and MB5 well. The domain extent is 300 × 300 × 350 m, with mesh refinement around the injection interval to resolve pressure and temperature boundary layers.

First, we fit the hydraulic parameters of the rock mass. We find that the measured injection pressure curve can be interpreted as the result of two sequential processes: 1) the rapid filling of high-permeability fractures, followed by 2) fluid leak-off into the matrix through pressure diffusion. These processes are illustrated in Figure 46.

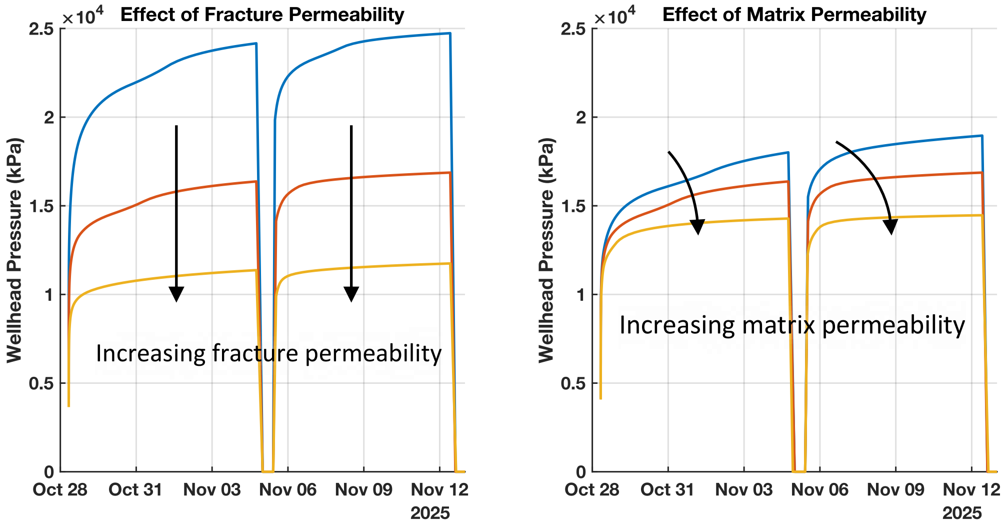

Figure 46. Influence of fracture and matrix permeability on wellhead pressure. The hydraulic behaviour can be interpreted as a two-step sequential process of fracture filling, followed by diffusion dominated leak off into the matrix.

For parameter estimation, we adopt a standard porosity of $\phi = 0.02$ and compressibility then tune the matrix permeability and fracture transmissibility, $Tr = wk_f$ in which w is the fracture hydraulic aperture and k_f is the fracture permeability. The fractures are all assumed to have identical hydraulic properties. We first use trial and error to find the neighbourhood of the permeabilities, followed by minimization of the error between simulated and measured pressures using a gradient descent line search to determine the minimum error. Figure 47 compares the measured and simulated pressure curves after parameter calibration. Our calibration is based on the first injection period, then we validate the model against the data from the other periods. The validation is excellent in the first validation period, and more modest in the second injection period. Rather than a single global optimum, multiple parameter combinations provide locally optimal fits for different time intervals. This behaviour is likely related to the absence of ST2 in the model, which acts as a pressure sink in the real system. Despite this limitation, the variability between optimal parameter sets is small, and the DFN model provides consistently strong agreement with the observed wellhead pressure evolution across both injection periods.

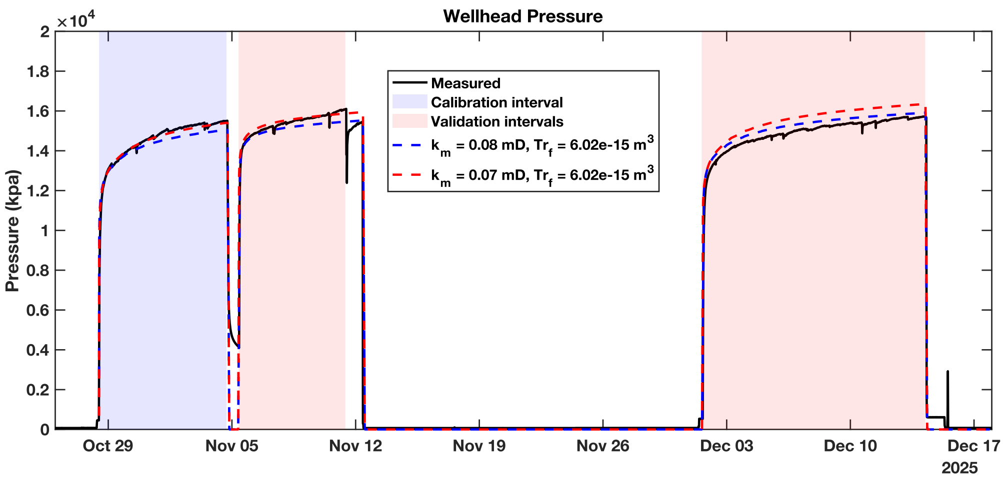

Figure 47. Simulated and measured wellhead pressures with calibrated hydraulic properties. k_m is the matrix permeability and Tr_f is the fracture transmissibility.

For an ideal planar fracture in which $k_f = w^2/12$, the calibrated fracture transmissibility corresponds to a hydraulic aperture on the order of $w = 4\mu m$. In reality, fracture tortuosity and roughness lead to a much smaller hydraulic aperture than physical aperture. The calibrated matrix permeability is substantially higher than the bulk permeability of an unfractured crystalline rock mass (typically on the order of ~0.001 mD = 10^{-18} m^2), suggesting that secondary micro-fractures are present and form the dominant means of fluid flow through the matrix.

Next, the thermal behaviour is analysed. Figure 48 illustrates the evolution of the heated volume in the reservoir, defined as regions experiencing a temperature increase of at least 0.5°C. The geometry of the heated volume clearly reflects the fracture-controlled flow pathways intersecting ST1, demonstrating that fractures dominate the spatial distribution of heat. During shut-in, fractures retain heat locally, while the outer extents of the fracture cool rapidly. Upon re-injection, the same fracture-controlled heating pattern re-emerges, indicating a strong structural control on thermal evolution.

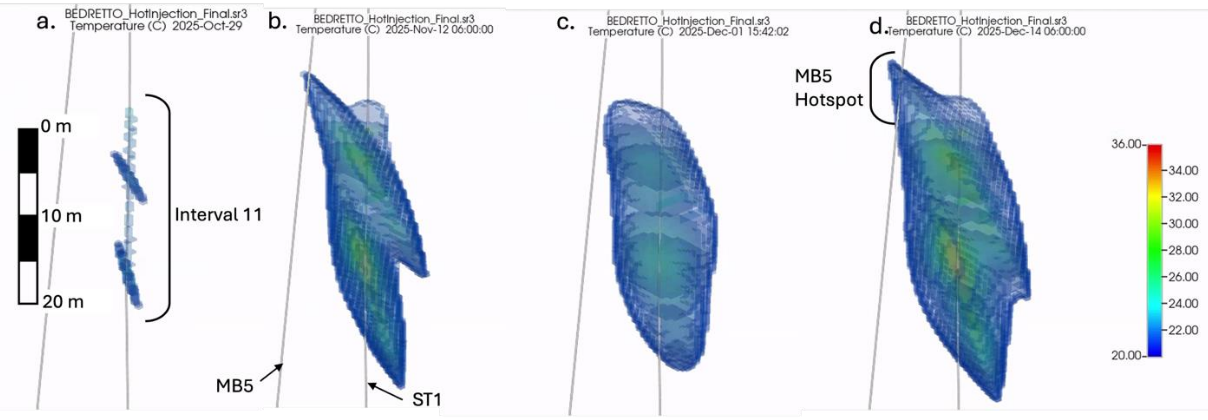

Figure 48. Development of the heated volume (temperature increase of at least 0.5℃) at times: a) one day into hot-water injection; b) end of first injection period; c) end of shut-in period; d) end of second injection period.

Figure 49 shows the calculated and measured temperatures at the midpoint of Interval 11. The agreement with measured temperatures is less accurate than for the simplified wellbore model because the borehole geometry and heat losses are not explicitly included in the DFN model. The temperature near the wellbore is smeared into the surrounding rock mass which results in slower simulated heating and cooling *Figure 49*. We therefore attempt to validate the temperature results using measurements from other wells, namely MB5.

Figure 50 illustrates the temperature profile along MB5 as well as the mean temperature over the hotspot at depth 130-150m for different fracture hydraulic apertures but fixed transmissibility. The model successfully reproduces the location and spatial extent of the hotspot, confirming that the hotspot is controlled by hydraulically active fractures, consistent with earlier observations. However, the model significantly overestimates the magnitude of temperature increase. To recover more similar behaviour, we can increase the storage capability of the fractures by increasing the fracture aperture while maintaining the calibrated transmissibility such that we don't alter the hydraulic behaviour. While this moves us closer to the observed results, we must increase the aperture to large non-physical values.

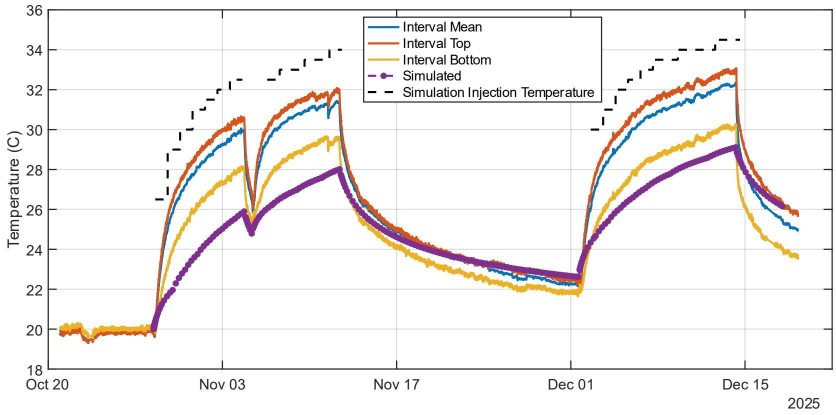

Figure 49. Temperature evolution at Interval 11 in ST1 in the DFN reservoir model compared to DTS measurements. The DFN model shows reduced accuracy due to the absence of explicit wellbore representation and heat losses.

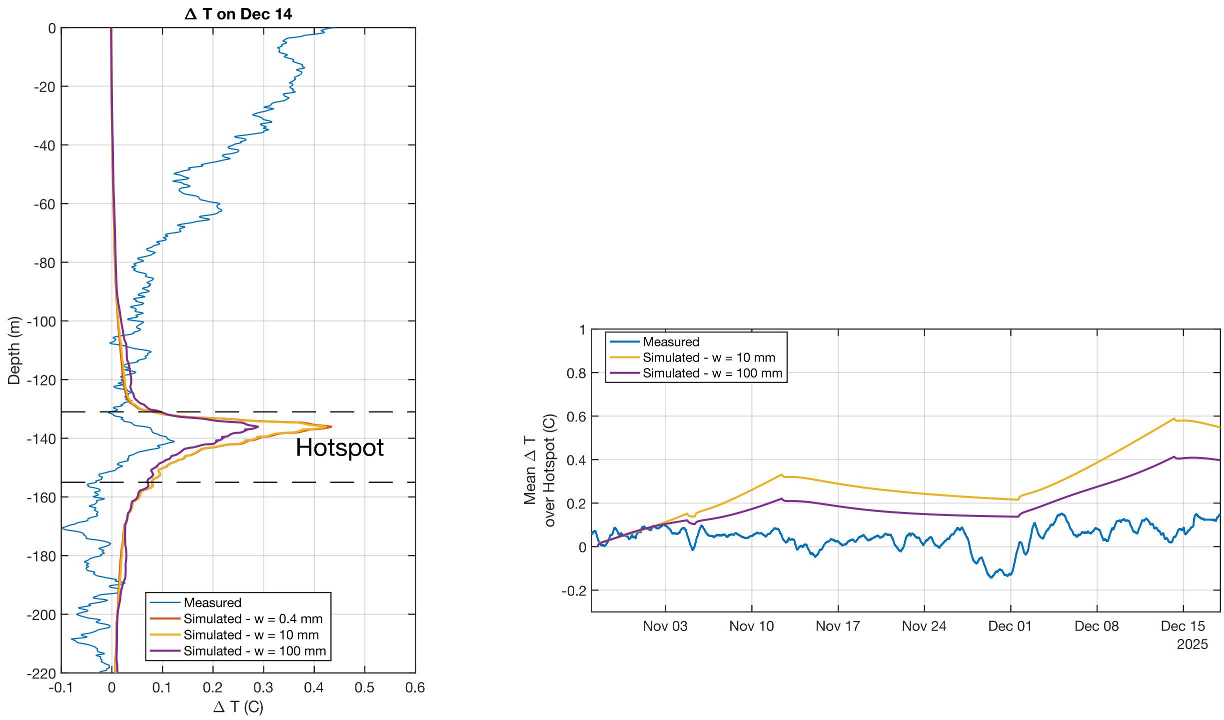

Figure 50. Temperature profile in MB5 from DFN reservoir model and mean temperature over the hotspot depth. The DFN model captures location and extent of the hotspot, but overestimates temperature increase.

This mismatch in temperature may have several explanations that cannot be conclusively resolved with the current dataset. First, the fracture geometry is idealized as planar, smooth, and homogeneous, whereas in reality, heterogeneity may limit direct fluid transport toward MB5 (see section 4.1.2). Second, the results may indicate the presence of a localized zone of enhanced thermal and hydraulic storage around ST1, not captured by the homogeneous parameterization. The calibrated hydraulic parameters represent an effective, spatially averaged rock mass, potentially masking such localized effects. This enhanced storage capacity could plausibly result from drilling-induced damage or stimulation-related alteration in the near-well region. Third, the impact of the permanent sink of ST2 plays a significant in heat transport, as shown in section 4.1.2. None the less, the calibrated parameters for the wellbore and DFN models provide a conservative underestimation of the ability of the surrounding rock mass to store and retain heat.

4.2.3. Wellbore Insulation

Heat loss along the borehole before reaching the injection interval is significant during the hot injection experiments. The fluid entered the borehole at 55°C and was ~32°C by the time it reached the injection interval. As discussed in Section 4.2.1, the heat loss along the wellbore is primarily responsible for the transient heating measured in the injection interval. This analysis uses the simplified wellbore heat loss model to examine the effect of installing insulation in the wellbore. To this end, we add a layer of insulation between the wellbore and the rock mass surface with a thickness of $t = 10\ mm$ and vary its thermal diffusivity. The thermal diffusivity of the insulation, α_i, is given as

$$\alpha_i = \frac{k_i}{\rho_i c_{pi}}$$

in which $k_i$is its thermal conductivity, ρ_i is its density, and c_{pi} is its specific heat capacity. The total insulating power of assembly scales such that a thicker layer of insulation reduces heat loss, and a lower thermal diffusivity also reduces heat loss (doubling the thickness is equivalent to using a material half as diffusive). We therefore report the effective insulation as the ratio of thickness to diffusivity, t/α_i $[mm/(mm^2/s)\ = s/mm]$.

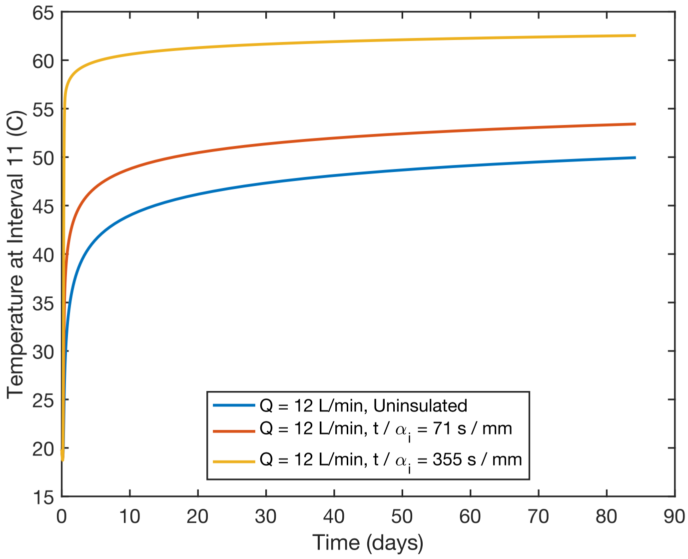

Figure 51. Effect of insulating in wellbore on temperature reaching interval 11 over time.

Figure 51 illustrates the temperature of the fluid reaching interval 11 as a function of time given an injection temperature of 80°C (assuming perfect insulation is installed in the tunnel before reaching the borehole, which we believe is achievable). We observe that the general shape of the curve is an initial fast heating period followed by a slowly increasing quasi-steady-state temperature. The initial heating is caused by the heating of the borehole surface, and the subsequent heating is caused by the ability of the rock mass to carry heat away from the borehole. There will thus always be some heat loss in the wellbore, but we can control the amount by controlling the flow rate and the insulation.

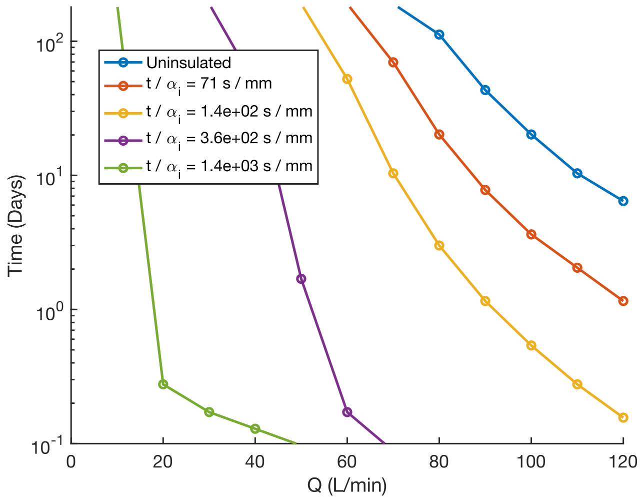

Figure 52 Effect of insulation and flow rate on temperature reaching interval 11.

Figure 52 illustrates the time for the temperature of the fluid reaching interval 11 to reaching a threshold of $0.9(T_{inj} - T_0)$ in which $T_{inj} = 80°\text{C}$ and $T_0 = 20°\text{C}$ is the initial temperature in interval 11. In an ideal full-scale system, we achieve high flow rates $(Q > 80L/min)$ and the injection period is long ($\Delta t \approx 3$ months). In the uninsulated case, the time to reach this threshold is approximately 10 days, ~11% of the total injection period. In the full-scale system, this heat loss can be partially recovered during the extraction phase but will be less efficient than storage deeper the reservoir because the area to exchange heat is smaller in the borehole than in the fractures. **Insulation improves the efficiency of a full-scale system but is not mandatory for operation.**

In the smaller-scale experiments performed in the BEACH project which use lower flow rates ($Q = 12\ L/min$) and shorter injection periods ($\Delta t \approx 14$ days), the system never reaches steady-state and continuously leeches heat through the borehole. To reduce this effect and effectively replicate the full-scale system on an experimental scale, sufficient insulation needs to be installed such that the borehole heat-up period represents a similar proportion of time as the full-scale system (11% of 14 days -> $\frac{t}{\alpha_i} \sim 1400 \frac{s}{mm}$).

4.2.4. Reservoir Storage Projections & Sensitivity Analysis

Last, the calibrated DFN reservoir is used to make projections of storage efficiency under a range of operating scenarios. Both operational and geologic factors are considered. **This analysis is intended to examine the potential efficiency of different operational concepts and does not reflect the maximum achievable storage potential of a fully engineered and optimized system.** The following assumptions are made:

- The cycle consists of 3 months of hot-water injection (the loading period), 3 months of rest (shut-in), 3 months of production (pumping) (the unloading period), and 3 months of rest, repeated cyclically.
- The target flow rate is 120 L/min. Injection pressure is limited to 16 MPa, while production pressure is limited to the vapor pressure of water. We only consider the use of surface pumps in this analysis.
- Fluid is injected at 80°C. Perfect insulation is assumed in the tunnel, which we find achievable. Perfect insulation is also assumed in the wellbore, which is less likely. However, the injection interval is expanded to allow greater flow such that only the first 50 m of the borehole are isolated and insulated while the rest of the borehole length is able to flow into the reservoir.
- Temperature-dependent viscosity and density, and the temperature gradient are reintroduced in the reservoir.

- All fractures have the same permeability as calibrated from the hot-water injection experiments (Section 4.2.2). No additional fractures are considered; only fractures connected to ST1 are included.

The target production and injection flow rate is assumed to be a maximum of 120 L/min based on the modelling in Phase I of the project which identified this flow rate as economically viable. We restrict flow beyond this target rate.

The energy efficiency of the cycles, ϵ, is calculated as

$$\epsilon = E_{out}/E_{in}$$

$$E_{in} = \int_{\Delta t_{inj}} Q_{in}\rho_f c_{pf}(T_{in} - T_0)dt$$

$$E_{out} = \int_{\Delta t_{prd}} Q_{out}\rho_f c_{pf}(T_{out} - T_0)dt$$

in which Q_{in} and Q_{out} are the injection and production flow rates in/out of the primary borehole, Δt_{inj} and Δt_{prd} are the loading and unloading time periods, T_{in} is the injection temperature of 80°C, T_{out} is the production temperature, and T_0 is a reference temperature. The reference temperature is taken as the ambient temperature of the tunnel, 17°C. In the cases with simultaneous injection and production, the recirculation of produced fluid is used to increase the reference temperature, reducing the required energy input into the system.

Figure 53 illustrates the instantaneous curves for flow rate and production temperature for a sample case. The per-cycle metrics; including average flow rate, temperature, and efficiency; are calculated using the instantaneous curves and summarized as time-weighted averages. In general, flow rates and temperatures are greatest at the start of each phase and decrease over time.

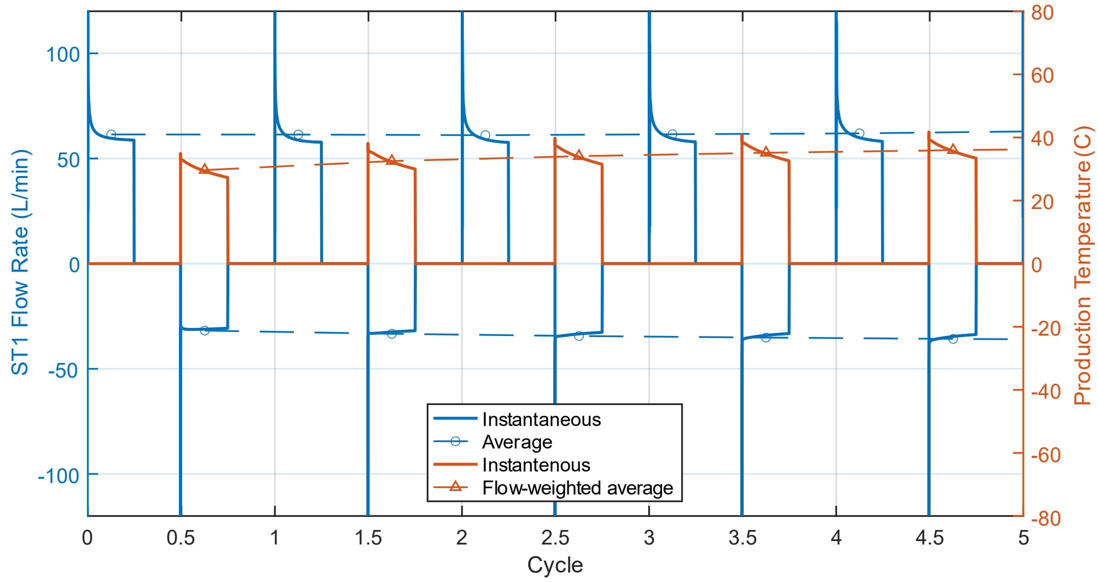

Figure 53. Instantaneous flow rates and temperatures from ST1 for an example case (case 4). Positive flow into ST1 indicates injection while negative flow indicates production.

Operational Controls on Efficiency

Injection Scheme

Three injection schemes are examined, as illustrated in Figure 54. First, a single borehole case is examined in which fluid is injected and produced from a single borehole. We observe that the system struggles to generate sufficient flow rates, which motivates the use of helper wells – additional wells which are used to change the local pressure gradients and generate more flow through the primary storage borehole. We examine two injection schemes with a helper borehole – one in which the helper borehole is used to motivate flow only in the production phase where the single borehole struggles; and a second in which the helper borehole is used in both the injection and production phases. For the alignment of the helper borehole, we first adopt the alignment of borehole ST2 to ensure a realistic alignment.

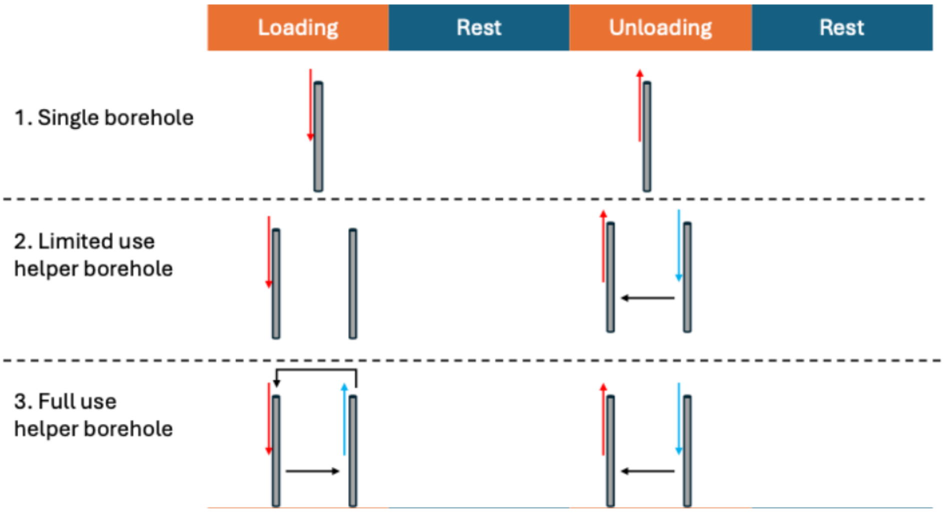

Figure 54. Operational setups for storage projections. In the single borehole case, fluid is injected and produced from the same borehole. In the limited use case of a second borehole, fluid is injected into the second borehole during production to encourage flow out of the first well. In the injector-producer case, the second borehole is used to encourage flow in both the injection and production phases.

Table 4 enumerates the flow rates, temperatures, and efficiencies for five cycles of operation for the three different injection schemes.

Table 4. Storage efficiency of different injection schemes using DFN reservoir model.

	Loading Period			Unloading Period			
Cycle	**Primary Borehole Flow Rate* (L/min)**	**Secondary Borehole Flow Rate* (L/min)**	**Average Produced Temperature (°C)**	**Primary Borehole Flow Rate* (L/min)**	**Secondary Borehole Flow Rate* (L/min)**	**Average Produced Temperature (°C)**	**Energy Efficiency (%)**
Case 1 – Single Borehole (ST1)							
1	41.7			-11.3		28.0	4.8%
2	39.9			-12.0		30.1	6.2%
3	39.7			-12.7		30.9	7.1%
4	39.7			-13.2		31.8	7.8%
5	39.8			-13.4		32.2	8.1%
Case 2 – Limited Use Helper Borehole (ST1-ST2)							
1	43.7			-20.5	21.9	27.4	7.7%
2	41.6			-21.4	21.7	29.2	10.0%
3	40.6			-22.1	21.6	30.1	11.3%
4	40.5			-22.6	21.5	30.7	12.2%
5	40.4			-23.0	21.5	31.2	12.8%
Case 3 – Full Use Helper Borehole (ST1-ST2)							
1	49.7	-14.5	17.8	-20.6	22.3	28.5	7.7%
2	48.8	-15.5	18.1	-21.6	22.2	30.8	9.8%
3	48.1	-15.6	17.9	-22.3	22.2	32.0	11.2%
4	48.2	-15.7	17.9	-22.7	22.1	32.9	12.1%
5	48.3	-15.9	18.0	-23.2	22.2	33.5	12.7%

*Average flow rate over period. Positive indicates inflow while negative indicates outflow.

There are several trends to observe that describe the behaviour of the system. First, the flow rates are asymmetric: the injection flow is limited by the maximum pressure to avoid jacking, while the production flow rates are limited by the vapour pressure. The target flow rate of 120 L/min is rarely achieved. Next, flow rates, production temperatures, and efficiency all increase over time. This trend does not plateau within the expected life of the system, and instead continuously increases.

The limitations on flow rate are particularly evident in the single borehole (Case 1), where pressure built up during the injection phase dissipates before production begins, resulting in low flow rates and energy efficiency. This limitation highlights the inherent challenge of single-well operation and motivates the investigation of multi-borehole configurations. In the limited use of a helper borehole (Case 2), production flow rates nearly double, due to the additional pressure support provided by the helper borehole, which drives fluid back toward the primary well. As a result, efficiency improves by approximately 50%, although absolute values remain still low.

The full-use helper borehole (Case 3) offers two advantages for efficiency. First, recirculation of produced fluid reduces the net energy input required. Second, the thermal plume generated during injection becomes more focused along preferential flow paths between wells, effectively concentrating thermal energy within the actively swept reservoir volume. Case 3 consequently offers higher loading flow rates and higher production temperatures than Case 2. Despite this, the overall efficiency of the system remains similar to Case 2. This efficiency is a ratio of energy loaded and unloaded and thus hides the fact that Case 3 loads and unloads >15% more energy than Case 2 and continues to produce a higher amount with each cycle. The full use helper well is adopted going forward for its advantages in energy storage and recovery.

Helper Wells – Alignment & Connectivity
Next, consider the impact of well alignment & connectivity on overall efficiency. Despite the use of the helper well in Cases 2 and 3, the flow rates in the helper well remain low. Wellbore ST2 was adopted for the alignment as this borehole was designed to be an injection well like ST1. However, we hypothesize that the low flow rates are attributable to the low connectivity of ST2 in the DNF model. Figure 55 illustrates the alignment of boreholes ST2 and MB1 relative to ST1 and the DFN and illustrates how ST2 has few intersections with the highly permeable fractures. By contrast, MB1 intersects multiple fracture and is more favourably positioned to provide connectivity to ST1. The alignment of MB1 is adopted to provide a realistic alignment of a potential helper borehole designed to have high connectivity to the storage borehole.

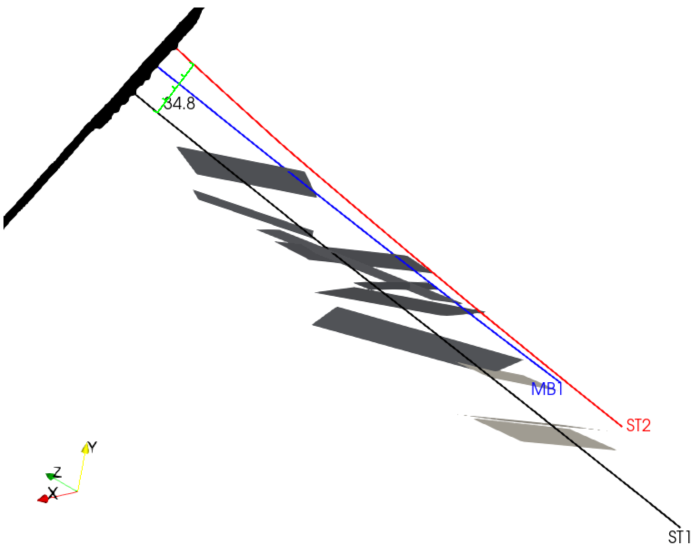

Figure 55. Alignment of boreholes ST1, ST2, and MB1 relative to the modelled discrete fractures. These alignments are used to evaluate the feasibility and performance of different storage operations.

Table 5 enumerates the flow rates, temperatures, and efficiencies for five cycles of operation for the two different alignments. The use of MB1 alignment results in a substantial increase in flow rates and elevated production temperatures, which translate to greater increase in system efficiency (+20-50%). The new alignment results not only an increase to the initial values but also experiences greater increases per cycle. Although thermal breakthrough represents a potential risk due to cold injection in the helper borehole, it is not expected to occur under the simulated conditions as pressure buildup dissipates between cycles. These findings illustrate the importance of well connectivity to engineering a successful FTES. **In all subsequent scenarios, case 4 is taken as the baseline against which changes are compared.**

Table 5. Effect of well alignment and connectivity on storage efficiencies

	Loading Period			Unloading Period			
Cycle	**Primary Borehole Flow Rate* (L/min)**	**Secondary Borehole Flow Rate* (L/min)**	**Average Produced Temperature (°C)**	**Primary Borehole Flow Rate* (L/min)**	**Secondary Borehole Flow Rate* (L/min)**	**Average Produced Temperature (°C)**	**Energy Efficiency (%)**
Case 3 – Full Use Helper Borehole (ST1-ST2)							
1	49.7	-14.5	17.8	-20.6	22.3	28.5	7.7%
2	48.8	-15.5	18.1	-21.6	22.2	30.8	9.8%
3	48.1	-15.6	17.9	-22.3	22.2	32.0	11.2%
4	48.2	-15.7	17.9	-22.7	22.1	32.9	12.1%
5	48.3	-15.9	18.0	-23.2	22.2	33.5	12.7%
Case 4 – Full Use Helper Borehole (ST1-MB1)							
1	61.4	-29.1	18.3	-31.8	36.8	29.7	10.6%
2	61.4	-30.9	18.7	-33.4	37.1	32.5	13.7%
3	61.1	-31.4	18.8	-34.4	37.4	34.1	15.7%
4	61.5	-32.0	19.1	-35.2	37.6	35.2	17.0%
5	62.0	-32.5	19.4	-35.8	37.8	36.0	18.0%

*Average flow rate over period. Positive indicates inflow while negative indicates outflow.

Helper Wells – Number

Next, consider the impact of the number of helper wells. A single well draws fluid towards it which helps to shape the thermal plume but does not make use efficient use of fractures that are not situated on the path between the wells. Increasing the number of helper wells can potentially make better use of the subsurface. To place new wells, we consider the alignment of borehole MB1, rotate it around the axis of borehole ST1 and space the wells at equal angle intervals. The alignment of new wells is illustrated in Figure 56 and the production metrics (flow rate, production temperature, and efficiency) are illustrated in Figure 57.

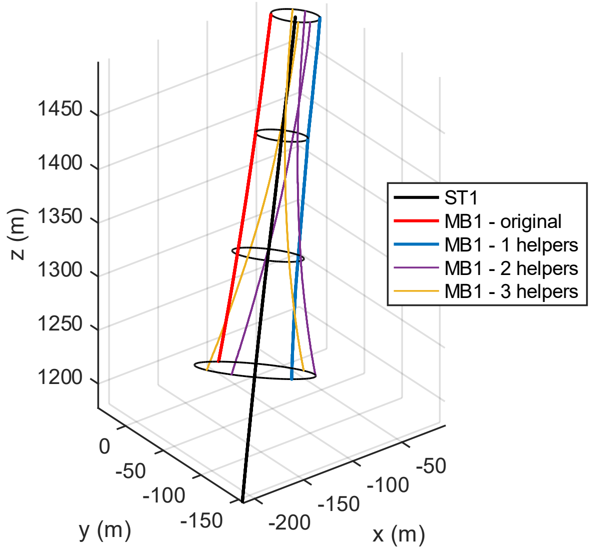

Figure 56. Alignment of boreholes ST1, MB1, and potential placement of more helper wellbores created by rotating MB1.

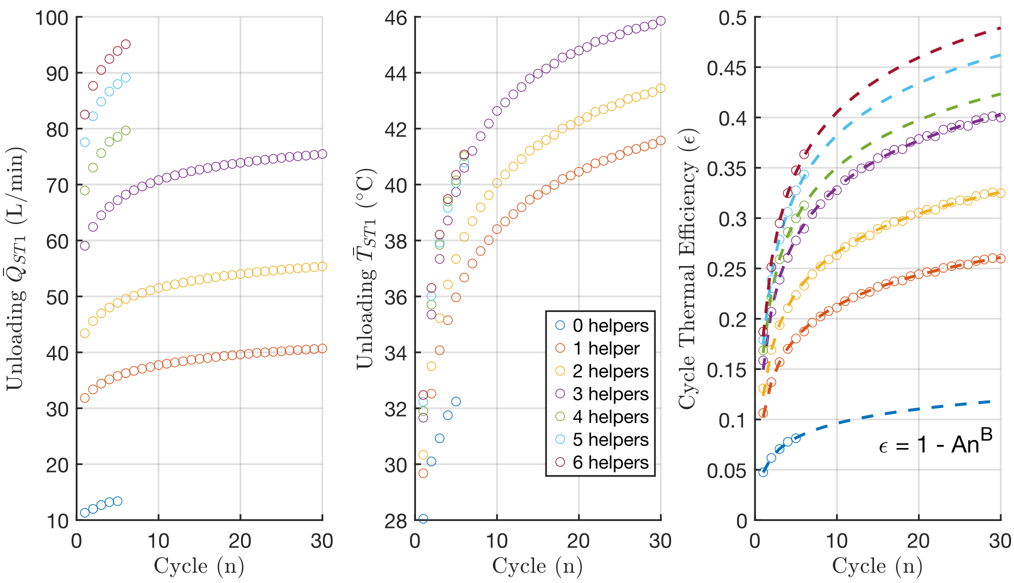

Figure 57. Production metrics (flow rate, production temperature, efficiency) of the system with an increasing number of helper boreholes.

Figure 57 also extends the cycles up to 30. The efficiency increases continuously and is well-described by the power-law relationship $\epsilon = 1 - An^B$ in which n is the number of cycles and A, B are fitting coefficients. The number of cycles required to reach an asymptote of efficiency exceeds 30 years, and continuous improvements are expected within the lifespan of the system. It is also observed that there is a positive correlation between the magnitude and the rate of change ($A \propto B$), which allows the trend to be described by the efficiency at a single point. We choose a representative cycle to illustrate the behaviour as $n = 4$ (4 years) to determine the trends as illustrated in Figure 58.

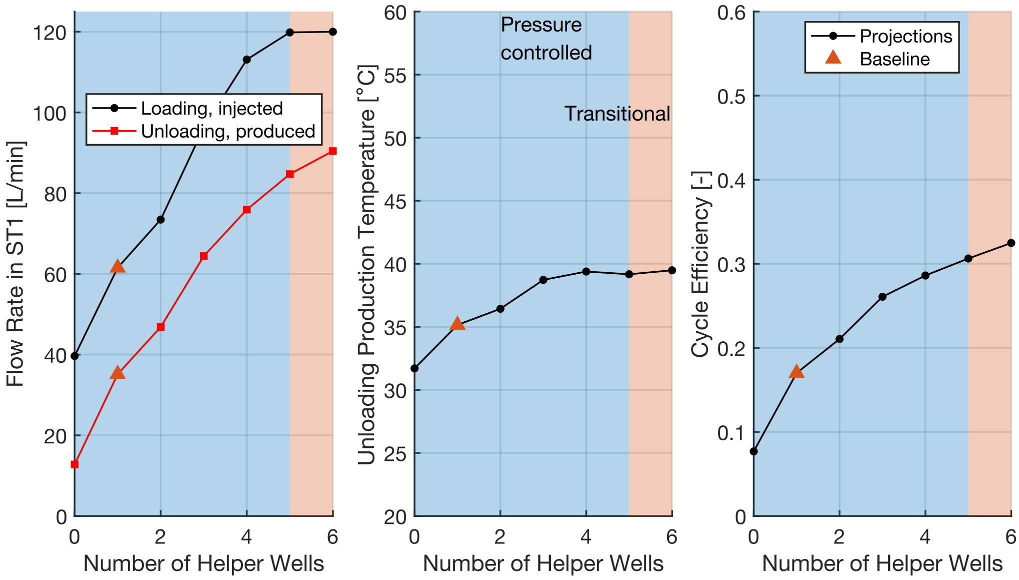

Figure 58. Production metrics (flow rate, production temperature, efficiency) at cycle $n = 4$ with an increasing number of helper boreholes.

In general, more helper wells results in higher flow rates and higher efficiencies. There are increasing returns up to three helper wells, after which diminishing returns are observed. This is partially attributable to the decreased volume swept by additional wells but also occurs due to the asymmetry of the loading and unloading phases. With a large number of helper wells, the target flow rate of 120 L/min is reached in the loading phase, transitioning the results from a pressure-controlled regime to a flow-controlled regime. A transitional regime is identified in which the loading flow rate is controlled by the target flow rate while the unloading flow rate continues to increase. Temperature appears to reach an asymptote once the loading flow rate reaches the target flow rate as the amount of energy imparted during the loading phase is now limited.

Injection Temperature

The last operational control considered is the injection temperature. The results of changing the injection temperature are illustrated in Figure 59. Higher injection temperatures require more external energy input and create higher temperature gradients which drive heat flow away from the storage away. Lower injection temperature has higher viscosity and thus lower flow rates which results in lower energy stored and recovered. Figure 59 illustrates how lower injection temperatures results in lower produced temperatures, but the produced temperatures ($\boldsymbol{\Delta T_{prd}}$) represent a greater proportion of the injected temperatures ($\boldsymbol{\Delta T_{inj}}$). Consequently, the efficiency increases at lower injection temperatures. This may be a desirable quality for applications such as district heating.

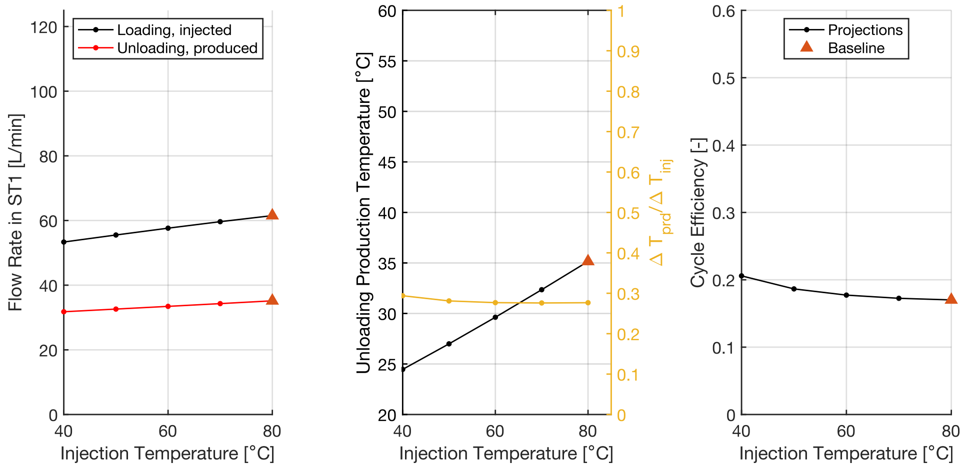

Figure 59. Production metrics at cycle $n = 4$ for changing injection temperature.

Geologic Controls on FTES Efficiency

Next, consider the impacts of geological features and site selection. In general, many geologic parameters are correlated – for example, increased porosity typically correlates with increased permeability. In this section, we examine the effect of making perturbations to the calibrated DFN model by changing parameters individually to isolate their effects.

Porosity

First consider the impact of porosity, which affects the rates of pressure and heat storage in the matrix. The calibrated DFN model assumes a porosity of $\boldsymbol{\phi} = 0.02$ in the experiment area, while the unperturbed granite nearby is around $\boldsymbol{\phi} = 0.01$. These are typical porosities for crystalline and granitic rock masses. Figure 60 illustrates the effect of changing matrix porosity. An increase in the flow rates is observed as the storage modulus of the matrix permits more flow. Accompanying the increased flow rates is an increase in production temperature. However, the cycle efficiency is practically unaffected by the matrix porosity.

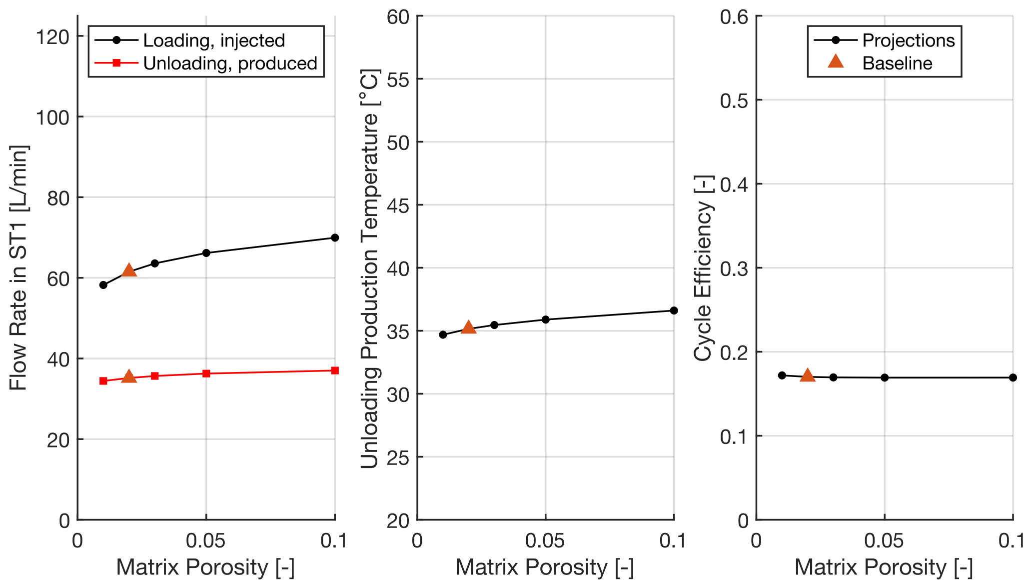

Figure 60. Production metrics at cycle $n = 4$ for changing matrix porosity.

Matrix Permeability

Matrix permeability is highly variable between rock masses and can vary over orders of magnitude. The bulk permeability of a granitic rock mass is typically on the order of $\mathbf{10^{-19}} - \mathbf{10^{-18}}$ m². Higher permeabilities are observed in the field due to the presence of smaller secondary fractures through the bulk matrix. Figure 61 illustrates the effect of different matrix permeabilities while the primary DFN transmissibility remains fixed. Three regimes are observed. At low permeabilities ($\boldsymbol{k_m < 10^{-17}}$ m²), the fluid flow is restricted to the DFN with little secondary flow through the matrix, and there is little change in the flow rates, production temperature, or efficiency. At high permeabilities ($\boldsymbol{k_m > 10^{-15}}$ m²), the flow rates enter the flow-controlled regime, and the matrix is permeable enough that heat during the storage period can be dissipated by heat-driven advection, resulting in lower production temperatures and the efficiency begins to decrease. In the transitional regime between the two extremes, higher matrix permeability allows for higher flow rates and production temperatures while not being so permeable as to allow high heat dissipation.

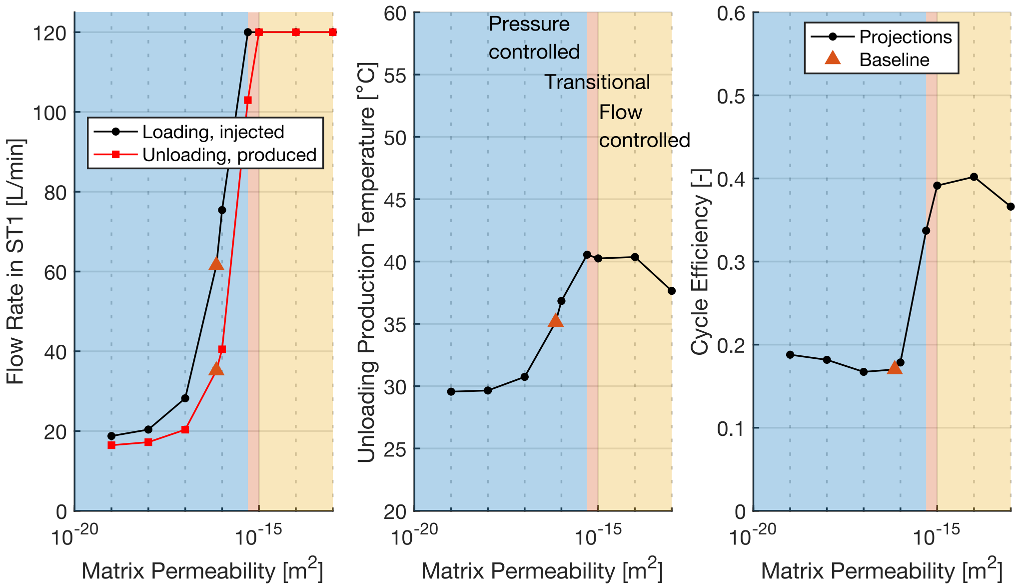

Figure 61. Production metrics at cycle $n = 4$ for changing matrix permeability.

Fracture Transmissibility

The fracture transmissibility controls the flow through the DFN and is the product of aperture and permeability, $\boldsymbol{T_{rf} = wk_f}$. The aperture affects the transmissibility as well as the storage and heat transfer to the rock mass. Thus, when scaling the fracture transmissibility, the cubic law is adopted to partition the scaling between the aperture and permeability such that $\boldsymbol{aT_{rf} = (a^{\frac{1}{3}}w)(a^{\frac{2}{3}}k_f)}$ in which $\boldsymbol{a}$ is a scaling factor. Figure 62 illustrates the effects of fracture transmissibility. Three regimes are observed once again – pressure controlled, transitional, and flow controlled. As with the matrix permeability, there is a strong correlation between the loading flow rate and the production temperature, and thus when it is restricted in the transitional regime, the production temperature decreases. Efficiency continues to increase in the transitional regime as the unloading flow rate increases, but efficiency decreases in the flow-controlled regime.

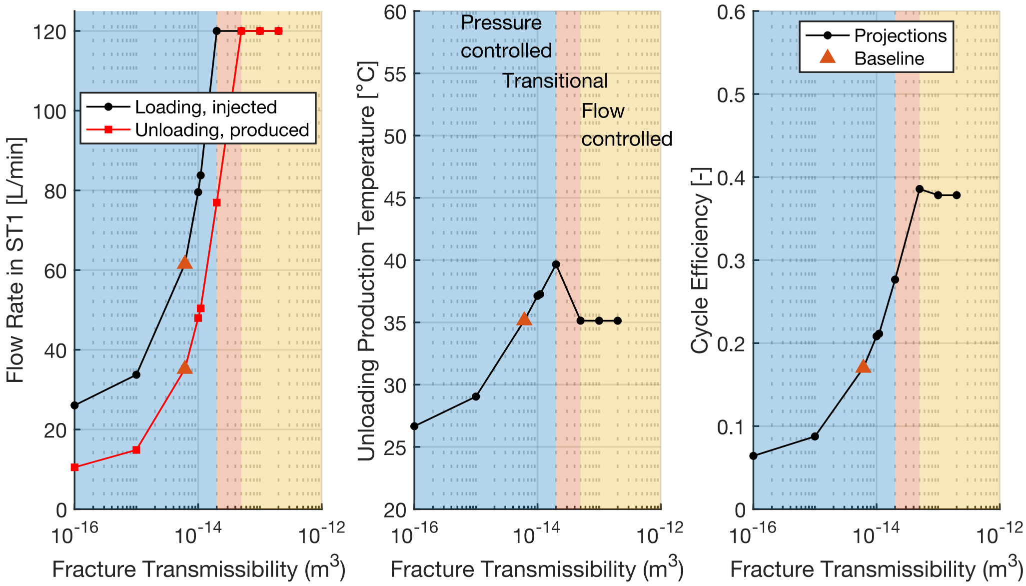

Figure 62. Production metrics at cycle $n = 4$ for changing fracture transmissibility.

Implications for FTES storage from DFN modelling projections

Across all the sensitivity analyses, we observe several consistent trends that have implications for FTES site selection and operation. First, there is a strong correlation between the flow rate in the loading phase and the production temperature during the unloading phase. Higher loading flow rates impart more energy to the rock mass and thus higher temperatures stored. Increases in the flow rate can be achieved through operational or geological means either through well placement or increasing the net reservoir transmissibility. Introducing helper wells to increase the flow rates and create crossflow is an effective method of increasing the flow rate, while also reducing the amount of input energy required. However, additional wells should be engineered to maximize connectivity with the storage well for optimal results (e.g. through placement of wells across well-connected fractures or hydraulic stimulation) .

The loading and unloading phases are asymmetric, and three regimes are generally observed: pressure-controlled (geology limitation), transitional, and flow-controlled (operational limitation). To utilize the rock mass to its full potential, the pressure-controlled and transitional regimes demonstrate better production metrics. A target flow rate of 120 L/min was identified in Phase I as potentially economically viable and is adopted as a maximum operational limit, however we observe here that the flow-controlled regime is suboptimal. The system performance is non-linear and operational restrictions on the flow rate result in reduced efficiencies. The system performance is greatest when the system is operated near its jacking limit when the flow rates are controlled by geological limitations.

Geologically, we observe a preference for systems which have a small network of high permeability fractures and minimal matrix permeability. This allows high flow rates and storage temperature but reduces the dissipation of stored energy by restricting heat transport to diffusion through the matrix. Rock masses with high matrix permeability risk the stored heat driving advection through buoyancy and pressurization.

These projections, while not optimized, demonstrate the strong influence of operational strategy and geology on the thermal storage capacity of the reservoir. Multi-well configurations can significantly improve system efficiency through enhanced pressure control in the reservoir and connectivity between the boreholes. Similar multi-well concepts are being investigated in the context of Aquifer Thermal Energy Storage, e.g., VESTA. Geological factors significantly affect the flowrates that can be achieved. There is a strong non-linearity between the production metrics of the system, the geologic conditions, and the operational strategy. This non-linearity must be accounted for in future techno-economic analysis and design of FTES.

4.3. CFD-based continuum model approach

An additional numerical model, designed to replicate the behaviour of the Bedretto Geoenergy testbed, is based on a computational fluid dynamics (CFD) approach framework aimed at investigating the thermal cyclical performance of the reservoir.. As already detailed in the Phase I report, the present model is based on a continuum approach employing porous media modelling. Once validated against experimental data, this simplified modelling approach (commonly used to simulate fluid flow and heat transfer in complex structures, e.g., packed beds, filters, foams or lattices), allows to obtain reliable results at a reasonable computational cost. With this modelling strategy, complex pore space morphologies and fault-scale structures are represented as equivalent continuous media embedded in the crystalline rock matrix, using volume averaged properties. Accordingly, fractures and faults are not explicitly represented in the model, and the fluid and solid phases are treated as overlapping continua. However, the effect of fractures and faults, on fluid flow and heat transfer, is taken into account through the integration of specifically derived porosity and permeability fields based on the real system incorporated through spatially varying porosity and permeability fields derived from the characteristics of the real system. Darcy's law is employed to determine the pressure drop exerted on the fluid flowing through the medium. Inertial effects can be neglected due to the small average fracture aperture, which results in laminar flow regime.

Furthermore, the fluid and solid phases are assumed to be in Local Thermal Equilibrium (LTE), meaning that both phases share the same temperature at any point within the domain. This assumption is supported by: (i) the relatively low flow velocities in fractured reservoirs which allow sufficient time for heat exchange between the fluid and the surrounding rock matrix, and (ii) characteristic heat transfer length scales being small compared to the overall domain size. Under the LTE assumption, a single energy equation for both phases is solved, with effective thermal properties obtained through volume averaging of the individual contributions from the solid and fluid phases.

4.3.1. Mapping of permeability

The porous medium approach requires the definition of hydraulic permeability in the simulation domain: the latter parameter is highly influenced by the local fracture network geometry (e.g. azimuth, tilt, aperture, planar extension). The bulk matrix permeability is several orders of magnitude lower than that of an open fracture or fault. For this reason, fluid flow and heat transfer are promoted along fracture planes and faults.

The present CFD modelling setup foresees the definition of an equivalent hydraulic permeability field in the computational domain capable of replicating the effect of the tortuous path water flow faces in the real case given by the complex void space in the crystalline rock: permeability would be orders of magnitude higher along fractures and faults with respect to the crystalline rock matrix.

A set of fractures, shown in the left-side of Figure 63, is used as reference to determine an equivalent continuum permeability field in the Bedretto reservoir, using an *Area Based Density* calculation:

- the reservoir domain is discretised into homogeneous voxels;
- a fracture density field is estimated by calculating the number of fracture points inside each voxel, weighted by an effective fracture area;
- The fracture density field is normalized into [0,1].

For each voxel, the fracture density field is calculated as follows:

$$\rho\,(x_i) = \sum_{k=1}^{N_f} A_k \cdot \exp\left(-\frac{d_{i,k}}{R}\right)$$

Where:

- N_f: total number of fractures.
- $A_k\,[m^2]$: total fracture area.

- $d_{i,k}[m]$: distance between voxel i and fracture k.
- $R\ [m]$: influence radius.

The distance $d_{i,k}[m]$ between each voxel i and fracture k is calculated as:

$$d_{i,k} = \min_{p \in \mathcal{F}_k} |x_i - p|$$

where p are fracture vertices $p \in \mathcal{F}_k \subset R^3$.
Normalisation is applied to the fracture density field, yielding relative permeability variation profiles along the 3 directions in the reservoir. The results of normalisation are shown on the right-hand side of Figure 63.

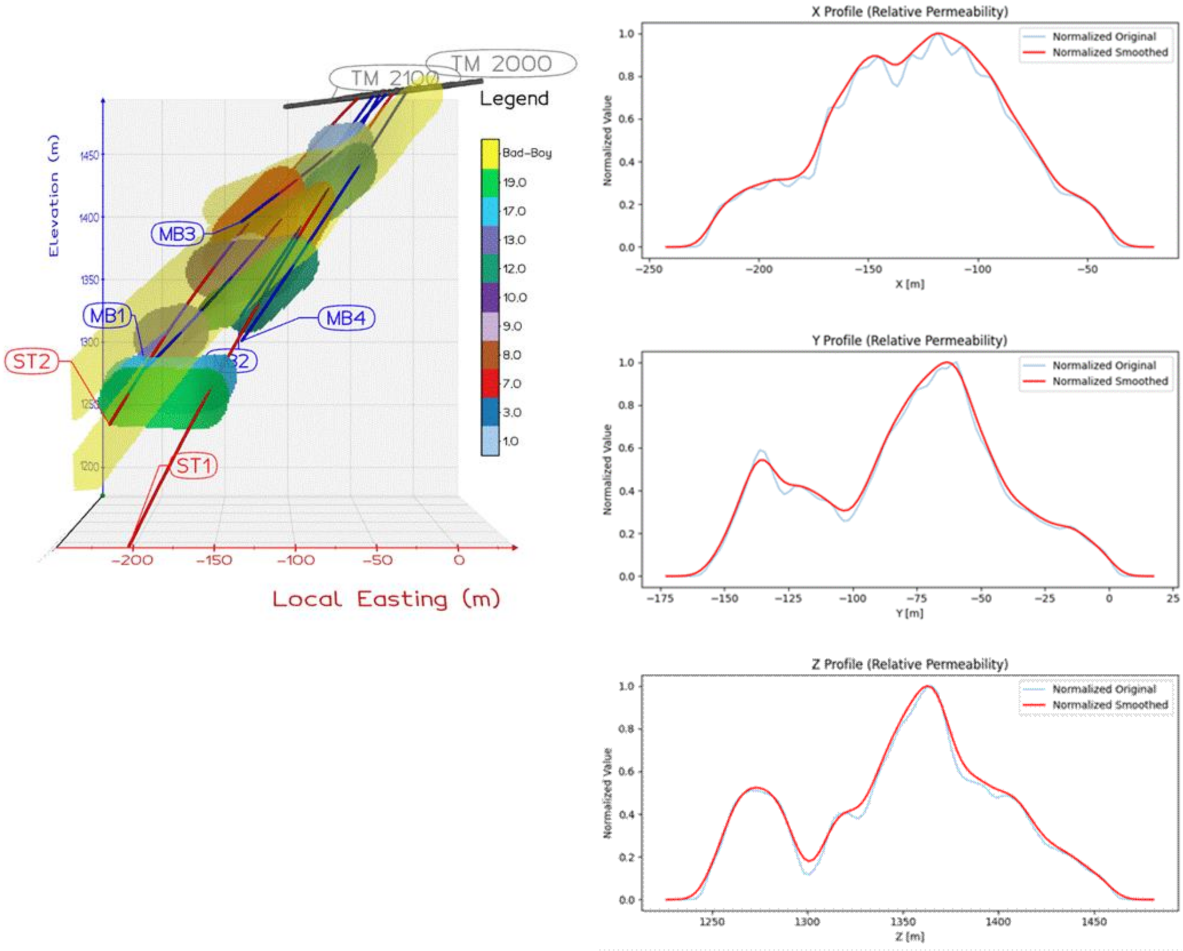

Figure 63: l.h.s) frontal view of mapped faults and fractures in the Bedretto reservoir. r.h.s) relative permeability variation profiles along the 3 directions in the reservoir domain (x , y , z , top-down).

Hydraulic permeability has been reconstructed in the domain by applying these relative variation profiles to minimum and maximum allowable scalar permeabilities in the reservoir domain:

- $k_{min} = k_{crystalline-rock} = 0.0037\, mD = 3.65E - 18\, m^2$
- $k_{\max} = k_{open-fracture} = 20\, mD = 1.97E - 14\, m^2$

Permeability is defined using log scales due to the orders of magnitude in difference between open fracture and crystalline rock matrix characteristics:

$$\log_{10} k(x,y,z) = \log_{10} k_{min} + \tilde{\rho}_{smoothened}(\log_{10} k_{max} - \log_{10} k_{min})$$

Polynomial fitting is performed using Python on the logarithmic permeability profiles to avoid ill conditioned coefficients and is implemented into the CFD software using User Defined Functions (UDFs) that allow the user to arbitrarily define hydraulic permeability in each domain's cell.

Therefore, permeability $k\ [m^2]$ and inverse absolute permeability $alpha\ [m^{-2}]$ (porous model input) are calculated directly in the UDF such as:

$$k(x,y,z) = 10^{\log_{10}(k(x,y,z))}\ [m^2]\ \ ,\ alpha = \frac{1}{k(x,y,z)}\ [m^{-2}]$$

4.3.2. Cylindrical FTES

The first approximation of the FTES reservoir has been modelled as a cylindrical domain in a multi borehole configuration: the central borehole is paired with 4 peripheral wellbores, and the cylindrical symmetry of the domain is exploited to reduce the computational effort, yielding a 45° “slice” as shown in Figure 64.

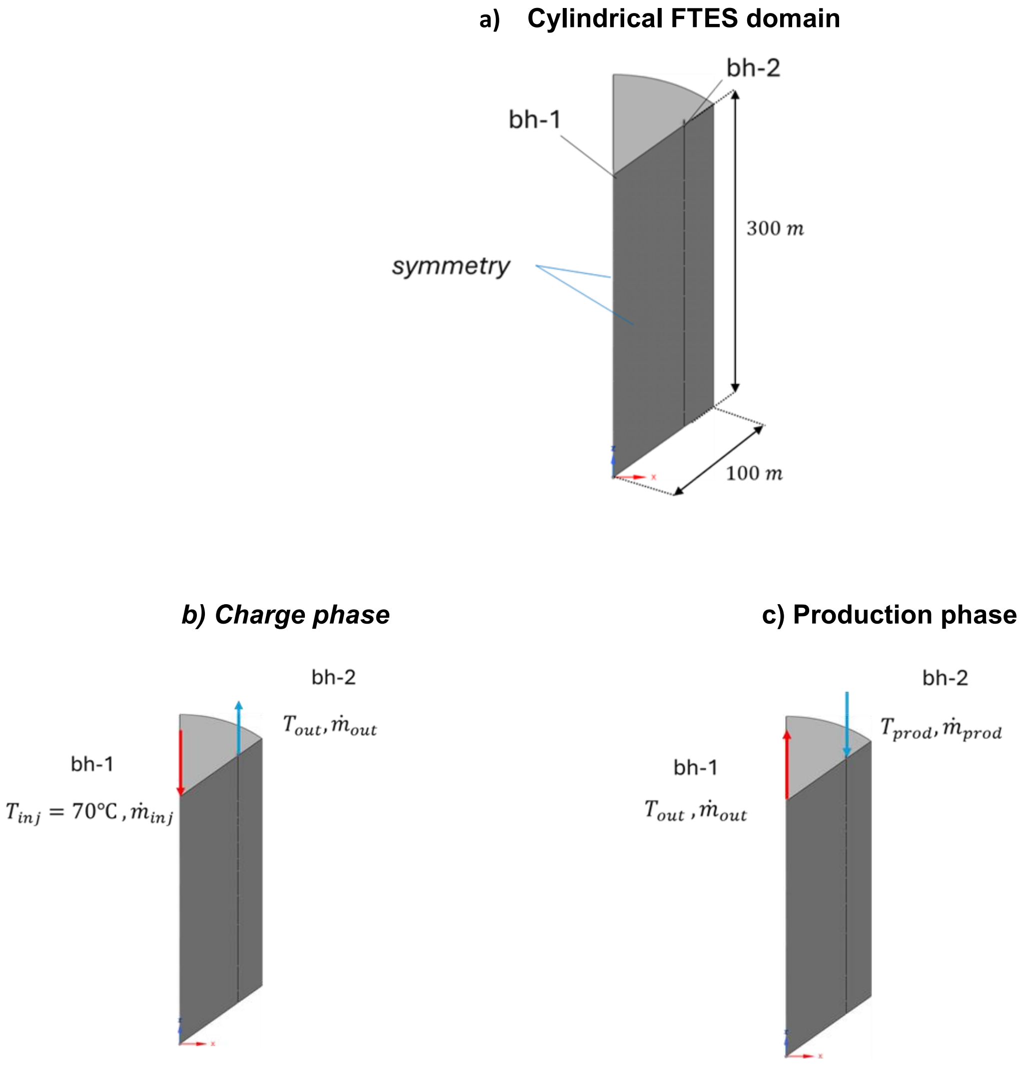

Figure 64: a) schematic representation of the cylindrical FTES domain, with shown symmetry boundary conditions and boreholes. b , c) Scheme of the charge and production phases respectively, with shown boundary conditions for both boreholes.

Considering a thermal cycling of the reservoir composed of charge (hot injection), storage/rest and production phases, the central borehole (bh1 in Figure 64a) is the one subjected to hot water injection during periods of energy surplus, whereas the peripheral boreholes (bh2 in Figure 64a) would be subjected to cold water injection during production phases.

Despite being a TES configuration different from Bedretto's facility layout, the resulting thermal performance, as well as the expected thermo-fluid dynamics behaviour, will anyway be representative of the single-borehole layout given the large extent of the computational domain considered. Including the four peripheral boreholes was necessary from a numerical standpoint to facilitate the conservation of mass and hence to obtain a smoother convergence of the iterative process.

The model's performances have been investigated by means of a sensitivity study foreseeing the identification of a proper temporal and spatial discretisation (time step and computational grid/mesh) to ensure results independency and accuracy: insights and main conclusions of the latter analysis are shown in the Appendix A2.

4.3.3. Thermal cycling results

In the following section, results referring to a hypothetical 5-year consecutive thermal cycling for the cylindrical FTES configuration will be presented in terms of temperature distribution and thermal efficiency of the reservoir.

The yearly cycle considered is composed by 4 periods lasting 91 days each:

– Charge phase (Jun-Aug): Hot water ($T_{inj} = 60°C$) is injected in bh-1.
– Storage phase (Sep-Nov): Boreholes are shut and thermal energy is diffused in the reservoir.
– Production phase (Dec-Feb): Cold water ($T_{prod} = 17°C$) is injected in bh-2.
– Rest phase (Mar-May): Boreholes are shut again.

For both charge and production phases, the total input mass flow rate is set to be $\dot{m} = 2\ kg/s$. Furthermore, it is worth to mention that all the water mass flow rate, fed through the FTES, is recovered (i.e., water leak-off = 0%).

Thermal recovery efficiency Φ is calculated as the ratio between extracted and injected thermal energies:

$$\Phi = \frac{Q_{prod}}{Q_{inj}} = \frac{\int_{t_{prod,start}}^{t_{prod,end}} \dot{m} \cdot c_{p,water} \cdot \left[T_{out,bh-1} - T_{prod,bh-2}\right] dt}{\int_{t_{charge,start}}^{t_{charge,end}} \dot{m} \cdot c_{p,water} \cdot \left[T_{charge,bh-1} - T_{out,bh-2}\right] dt}$$

Thus, this cycle will be simulated for 5 consecutive years in order to assess the cyclic performances of the reservoir. As depicted in Figure 65, for the first yearly thermal cycle, the charge phase yields a significant temperature gradient in the vicinity of the high permeability cluster; thermal diffusion during storage phase is detrimental, as the temperature gradient developed during the charge phase is almost completely dissipated: the prolonged duration of the storage phase allows for the “high” temperature thermal energy injected during the charge phase to be dissipated into the domain and the far field before being exploited with a production phase. The production phase yields an outflow temperature of almost $28°C$. The final rest phase practically restores the initial condition of the reservoir, to an almost steady state before injection temperature field; thermal recovery efficiency for the first-year cycle is 34.8 %.

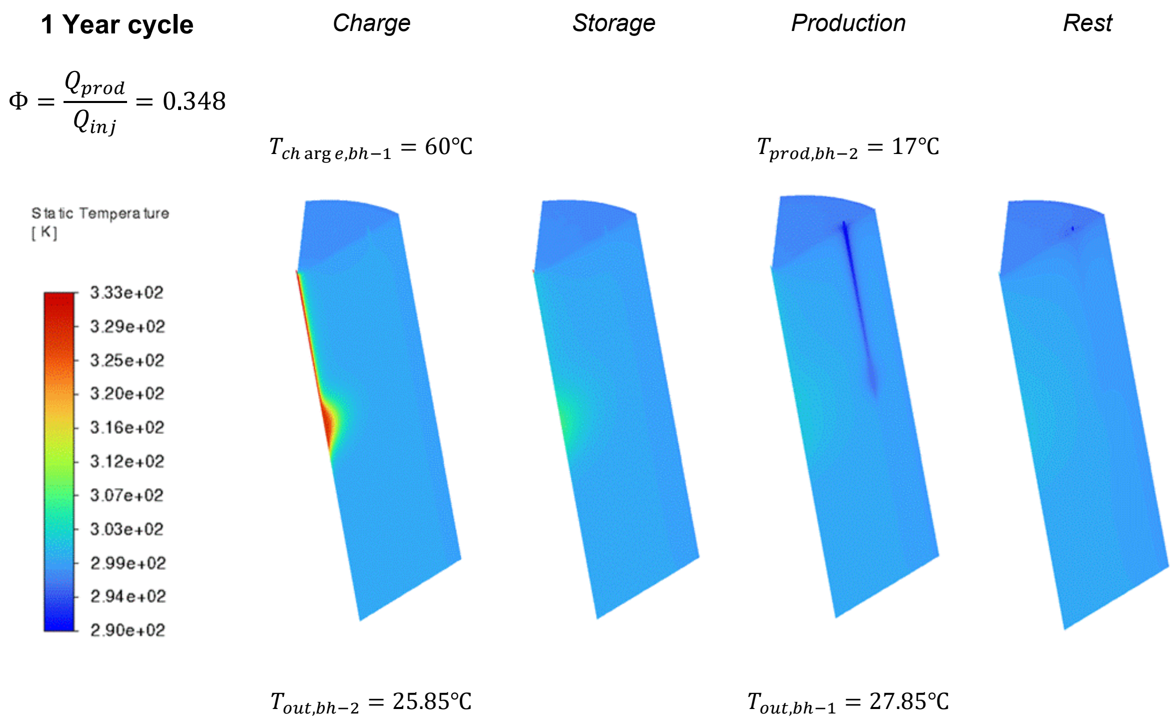

Figure 65: results after each phase of the first-year cycle in terms of temperature contours and average temperature at the wellheads. Thermal recovery efficiency is shown in the top left corner.

After 5 consecutive years of thermal cycling, as depicted in Figure 66, the behaviour of the reservoir does not change significantly: the temperature field achieved at the end of the charge phase is slowly diffused during the 3 months storage phase, while the production phase outflow temperature is increased by $1.6°C$ if compared to the first-year cycle. Overall, thermal recovery efficiency is gradually increased with each reservoir cycling as expected, and after 5 years the latter value reaches 39.5 %, which is 5% higher than the first cycle. The reason for thermal recovery efficiency being above 30% in spite of the recovery temperature being only $28°C$ could be identified in two main reasons:

1. Low production temperature: cold water injection during production phase at $17°C$ allows for the heat transfer fluid to recover the natural thermal gradient present in the reservoir.
2. Peripheral boreholes configuration: the peripheral boreholes form a sort of enclosure around bh-1, and during the production phase, the flow path of the heat transfer fluid is evenly distributed from the outer diameter of the reservoir to the central borehole.

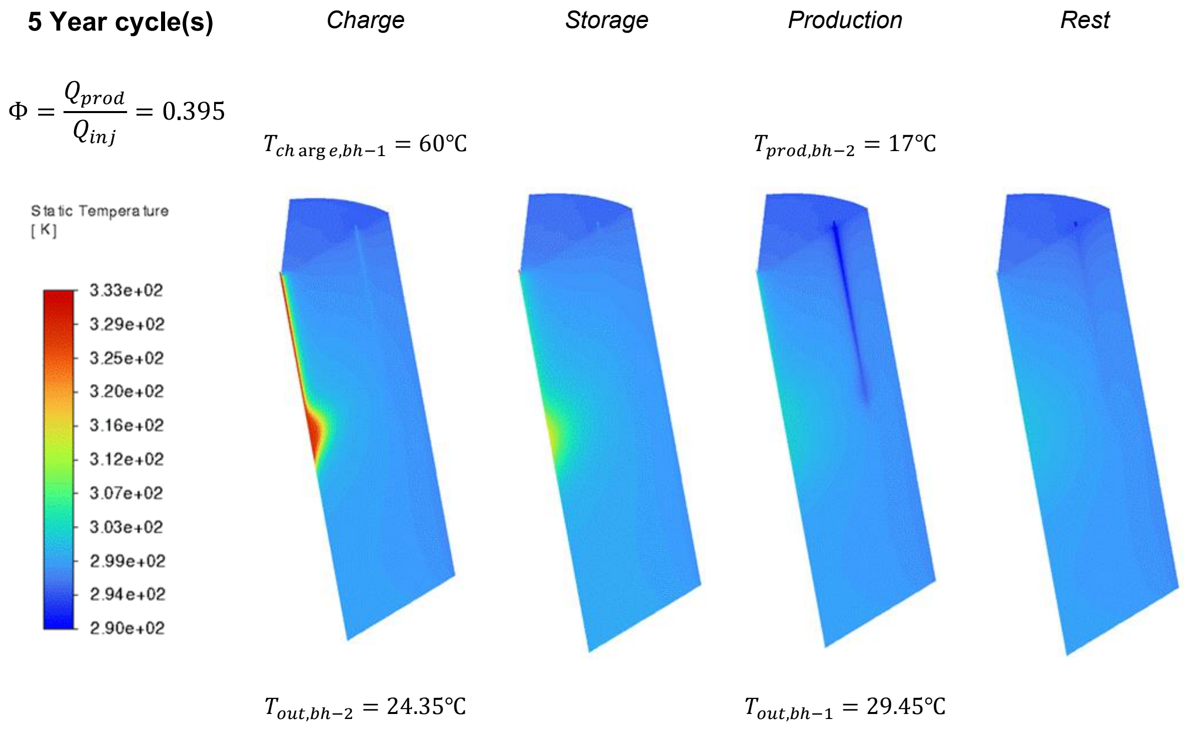

Figure 66: results after each phase of the fifth-year cycle in terms of temperature contours and average outflow temperature at the wellheads. Thermal recovery efficiency is shown in the top left corner.

4.3.4. Box shaped FTES

With the aim of validating the present modelling strategy with experimental data, a different computational domain, more comparable with the actual experimental setup in the BedrettoLab, has been developed. The latter computational domain is configured as box shaped, comprehending a volume of crystalline rock that resembles the actual elevation range of the Bedretto laboratory, between 1'200 m and 1'500 m a.s.l.. A double wellbore arrangement is considered by including ST1 and ST2 boreholes, both approximated with straight trajectories; ST1 is divided into packer intervals akin to the real setup. The boreholes geometries are also simplified by modelling them as simple tubes with no change in cross section.
Figure 67 summarizes the geometry employed for the simulation of the Bedretto reservoir: the domain spans ca. $300\,m$ in elevation, while the dimensions along the x and y directions are $333\,m$ and $346\,m$ respectively.

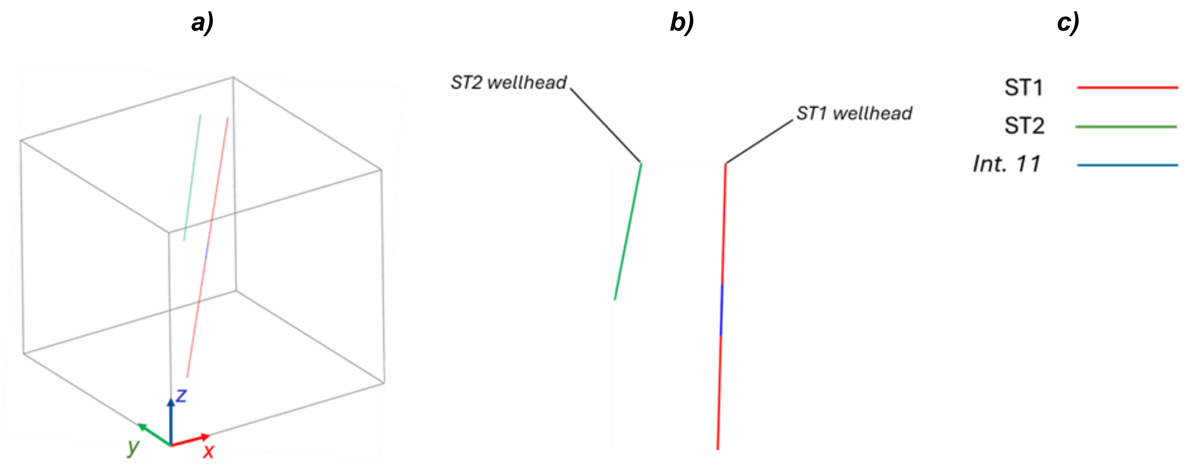

Figure 67: a) Bedretto box shaped computational domain, including wellbores. b) Magnification of ST1 and ST2 wellbores. c) Colour legend for wellbores and chosen injection interval.

During energy excess periods, when energy supply exceeds demand, hot water injections are performed into ST1, like in the real setup: the input flow will be resulting in an outflow at the ST2 wellhead. During energy excess periods, when energy supply exceeds demand, hot water injections are performed into ST1. Differently from the real setup, but necessary from the CFD model standpoint to facilitate mass conservation, the input flow will be resulting in an outflow at the ST2 wellhead. During production phases, cold water is injected into ST2 wellhead, and the outflow is completely recovered through ST1.

As for the previous investigation, continuum porous media approach is employed with imposed hydraulic permeability profiles and Local Thermal Equilibrium assumption. Furthermore, here also the entire recovery of the injected water (no water leak-off) is also assumed.

Starting from the normalized relative permeability profiles, a three-dimensional field is implemented into the domain by combining the 3 profiles along the three directions, using the following formulation:

$$k_{combined} = \sqrt[3]{k_x \cdot k_y \cdot k_z}\ [m^2]$$

Then, the de-normalized profiles (using minimum and maximum allowable values as cited in 2.1) are applied to the box shaped domain geometry, yielding the following hydraulic permeability field.

As shown in Figure 68, hydraulic permeability is highly heterogeneous in the reservoir: a high permeability cluster zone is situated, as expected, in the proximity of interval 11 depth ($z = 150\ m$).

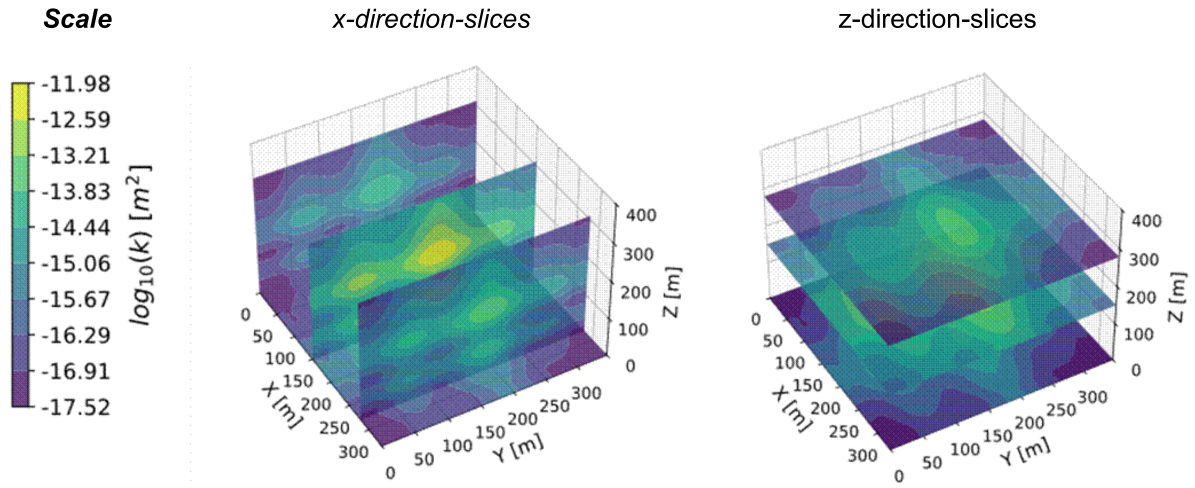

Figure 68: log-scale mapping of the hydraulic permeability field; l.h.s) reservoir sliced along x-direction; r.h.s) reservoir sliced along z-direction.

The experimental dataset of reference for the validation of the CFD model refers to the measurements and logging of hot water injections and thermal cycles gathered between 28.10.2025 and 20.12.2025. This experimental time frame includes two hot water injection phases and two production phases; the first thermal cycle includes hot water injection phase, a shut-in (rest or storage) phase and production phase, while the second does not comprehend a rest phase, i.e. production followed immediately the hot water injection.

The main objectives of this validation are to assess the model accuracy in replicating the measured temperature profile evolution at the injection interval (interval 11, ST1) and to predict the thermal recovery efficiency of the two cycles.

To fairly compare simulations results with experimental data, an initial temperature profile for ST1, sampled from measured DTS data for both charge and production phases, were imposed as fixed-temperature boundary condition along the walls of ST1. Operating conditions for all phases, namely flow rates and injection temperatures, are extracted from the same dataset, and are summarised in Table 6. Since the real configuration is operated through a single injection and production borehole (ST1), the inflow of ST2 for the production phase is not available; as a workaround, the measured outflow of ST1 is used as input flow rate for ST2 during the production phases and is sampled as constant. To represent the temperature field surrounding the crystalline rock reservoir, undisturbed temperature boundary conditions are applied at a $15\,m$ distance from the external boundaries of the domain; at the top boundary, temperature is set at $T_{top} = 16°\mathrm{C}$, while for the side and bottom boundaries is $T_{side} = 22°\mathrm{C}$ and $T_{bottom} = 26°\mathrm{C}$ respectively.

Table 6: Summary of operating conditions for charge and production phases.

Phase	*wellhead*	*Flow rate* $[\frac{L}{min}]$	*Temperature* $[°\mathrm{C}]$
Charge phase	ST1	12	70
Production phase	ST2	4	20

Resulting temperature profile at interval 11, as comparison with experimental data, and percentage error are presented in Figure 69. Along the two thermal cycles evolution, temperature profile from CFD results slightly overestimates the experimental measurements with a maximum error, in correspondence of the shut-in that occurred during the first injection phase. At the end of the latter phase the error is lowered.

The longer shut-in (storage) phase that followed caused a significant reduction in temperature at interval 11, in agreement with the model results. Thus, the recoverable thermal energy from the 1st production phase is largely affected.

Unlike the first, the second thermal cycle did not register any interruptions (see Section 3.1.3) during the injection phase, so the injection cycle profile at interval 11 was regular and continuous, reaching a maximum temperature of about 32℃; the model overpredicts this temperature with an error lower than 2%. The second production phase started right after the hot injection, and temperature at interval 11 regularly decreases down to 25℃; model results still tend to overpredict the temperature profile, yet with an error steadily decreasing from 11% to almost 4%.The second production phase started right after the hot injection, and temperature at interval 11 regularly decreases down to 25℃; model results still tend to slightly overpredict the temperature profile, yet with an error steadily decreasing from 11% to almost 4%.

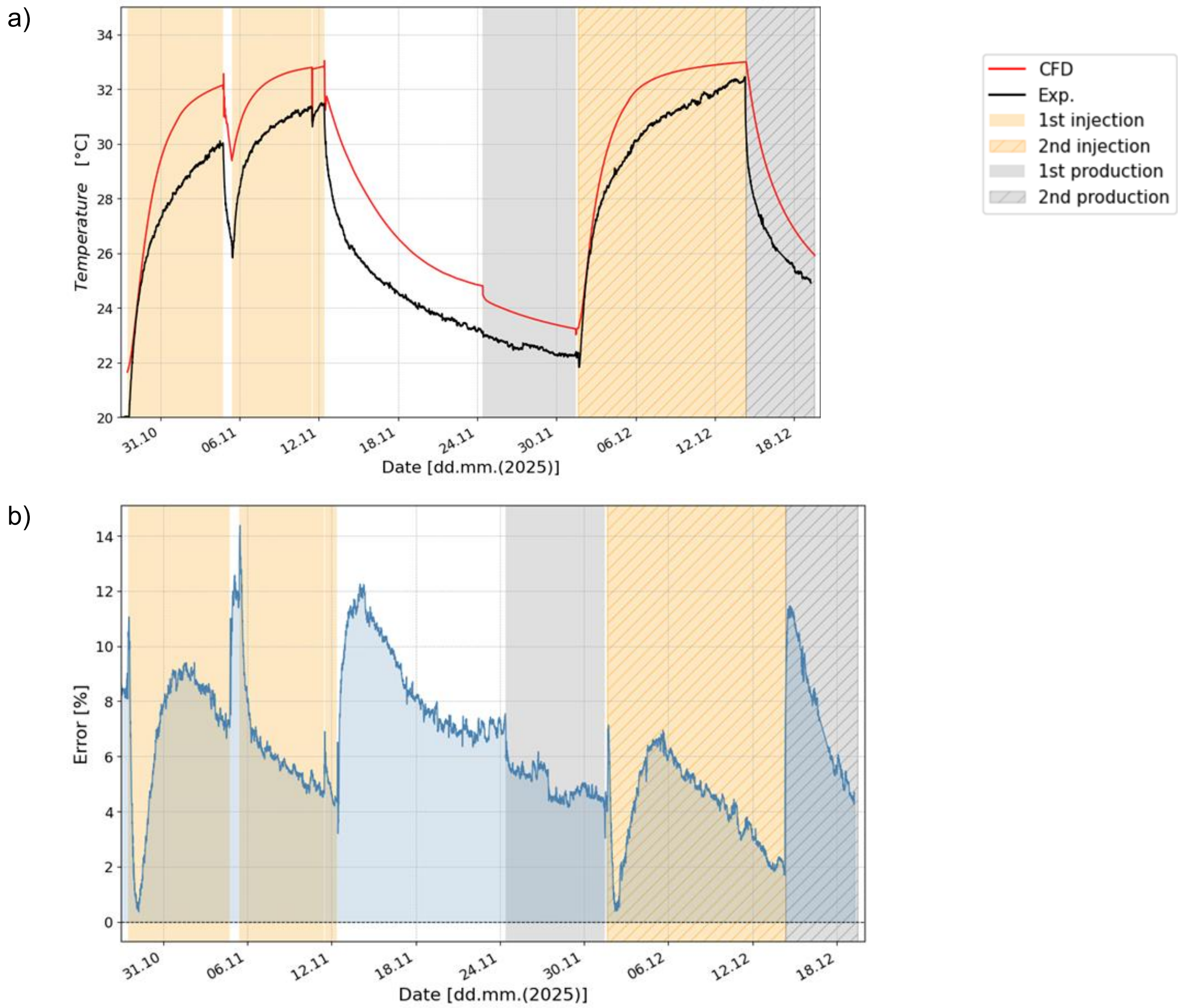

Figure 69: a) comparison of temperature profiles along interval 11 in ST1; r.h.s) colour legend, and the considered depth bounds to average the experimental temperature profile. b) Plot of percentage error between CFD and Experimental data (Interval 11 depth bounds: upper: 132.2 m, lower 150 m).

An energy balance assessment of these two cycles is presented in Table 7. For what concerns the first cycle, experimental data yields a recovery efficiency of 6.31%, while the CFD model estimates a slightly higher thermal efficiency of 8.17%. Experimental data suggests that the reservoir behaved more efficiently during the 2nd cycle, as measured recovery efficiency equals 9.70%; in this case, the recovery efficiency predicted by the CFD model was 8.28%.

Since no shut-in phase occurred after the 2nd injection, the charging front developed in the reservoir could be readily exploited during the production phase to extract a greater amount of thermal energy, which otherwise would have had time to diffuse in the rock matrix: hence, a higher recovery efficiency is registered.

Table 7: energy balance and recovery efficiency assessment of the two thermal cycles, for both experimental and CFD model results.

Cycles		*1st cycle*		*2nd cycle*	
		Exp.	**CFD**	**Exp.**	**CFD**
Injected energy	$Q_{inj}[kWh]$	3'708.66	3'193.14	3'612.56	2'874.58
Produced energy	$Q_{prod}[kWh]$	233.88	260.77	350.24	238.04
Th. recovery efficiency	$\Phi = \frac{Q_{prod}}{Q_{inj}}\ [\%]$	6.31	8.17	9.70	8.28

4.3.5. Summary of CFD models

The development and validation of the continuum, porous media CFD-based model for the simulation of a possible FTES in the BedrettoLab was presented. The continuum porous media approach, structured on a fracture density-based permeability mapping and LTE assumption, was proved capable of replicating the cyclic thermal behaviour of the reservoir, with a reasonable level of accuracy.

On a first approximation, a cylindrical representation of the FTES, considering one central and four peripheral boreholes, allowed for a sensitivity analysis to be carried out, identifying the suitable spatial and temporal discretisation to ensure acceptable accuracy and results independency.

The latter cylindrical configuration demonstrates that thermal recovery efficiency increases over consecutive cycles, reaching 39.5% after five years, with an increase of about 5% with respect to the first cycle.

A second computational domain based on the double wellbore (ST1-ST2) configuration in the Bedretto underground laboratory was developed including an anisotropic hydraulic permeability field, and its accuracy was evaluated by comparison with an experimental dataset from the hot water injection cycles, referring to October-December 2025. The box-shaped model yields a temperature evolution at the injection interval (interval 11) with errors generally below 5% at the end of each cycle phase (charge, storage, production). The maximum deviation between CFD model results and experimental data correspond to the extraordinary shut-in events during the first injection phase. Nevertheless, thermal recovery efficiency of the reservoir showed a fairly good agreement, for both cycles. The CFD model, unlike measured data, did not register a significant increase in thermal recovery efficiency between the two cycles. For the second thermal cycle, recovery efficiency is slightly underpredicted by the CFD model ($\Phi_{CFD,2nd\,cycle} = 8.28$), as experiments seem to yield more optimistic results ($\Phi_{EXP,2nd\,cycle} = 9.70$).

4.4. Summary of heat storage modelling

- Continuum (CFD) and discontinuum (DFN) models were used to reproduce experimental observations related to pressure evolution at the injection interval and temperature evolution within the fracture reservoir. Additionally, they were used to extrapolate to larger time scales (i.e., seasonal storage), to cases with insulated boreholes as well as to cross-hole and multi-borehole configurations.

- The models were able to reproduce the observed pressure and temperature evolution during the hot water injections within an accuracy of <10%.
- DFN models show that heat remains near the injection borehole and is not carried to the far-field. Fractures significantly affect the distribution of the heat injected into the rock mass. A zone of increased storage capacity exists near the borehole, which was likely caused by hydraulic stimulations within the VALTER project.
- CFD and DFN model approaches confirm the observed significant heat losses along the borehole. Clearly, the heat storage in the designated reservoir area may be improved by reducing heat losses along the borehole.
- Crosshole configurations are expected to be significantly more promising than single hole configurations for heat storage potential due to their ability to generate higher flow rates, resulting in an increase of the recovered energy. The key parameter for increasing the flow rates is the connectivity between the wells, which is a determined by the fractures. Further improvements in efficiency may be achieved by examining other intervals with higher transmissibility.
- Additional improvements of efficiency can be achieved with multi-borehole configurations, in which a central injection/production borehole is surrounded by boreholes that control pressure and temperature evolution in the reservoir around the central borehole.
- Thermal diffusion into the rock matrix, during idle phases especially, seems to be a detrimental factor reducing the temperature at which thermal energy can be recovered. Water leak-off is another limiting factor of the FTES performance.
- To date, the numerical model scenarios expanding on experimental observations towards more efficient borehole configurations and reservoir conditions are not exhaustive. Further work will be part of Part III of the project, during which cross-hole heat storage observations will become available.

5 Concept for cross-hole heat storage configurations

Building on the experience from the first FTES experiments in Phase II, we plan to expand on the experimental program to test different injection scenarios that also include borehole configurations that promise to improve the efficiency of the heat storage. A range of approaches have been mentioned in Section 3.4, which may enhance storage efficiencies. While not all approaches can be tested within the framework of this project, we will focus on the following:

- Insulation of the borehole above the injection interval.
- Combine a production and injection borehole to a crosshole configuration

Insulation of the injection borehole is done in collaboration with solexperts, who develop an approach to achieve thermal insulation in the existing injection borehole, which was not designed for heat storage originally. Two approaches are being evaluated: 1) a double packer system that is inserted into the central rod to pack off the target interval and above which the water in the annular space within the larger central rods and around the smaller double packer is replaced by air with an airlift system. 2) A smaller thermally insulated injection rod system is inserted into the larger rod system.

Additionally, a packer system that allows injection through a thermally insulated rod system is developed for new injection boreholes.

With regards to a second production/injection borehole for crosshole heat storage experiments, different options have been evaluated:

- Option 1: Remediation of the existing borehole ST2
- Option 2: Drilling of a production borehole at a location optimized for heat storage.

To evaluate the different options, it is worthwhile considering the hydrogeological situation of the different boreholes in Figure 63.

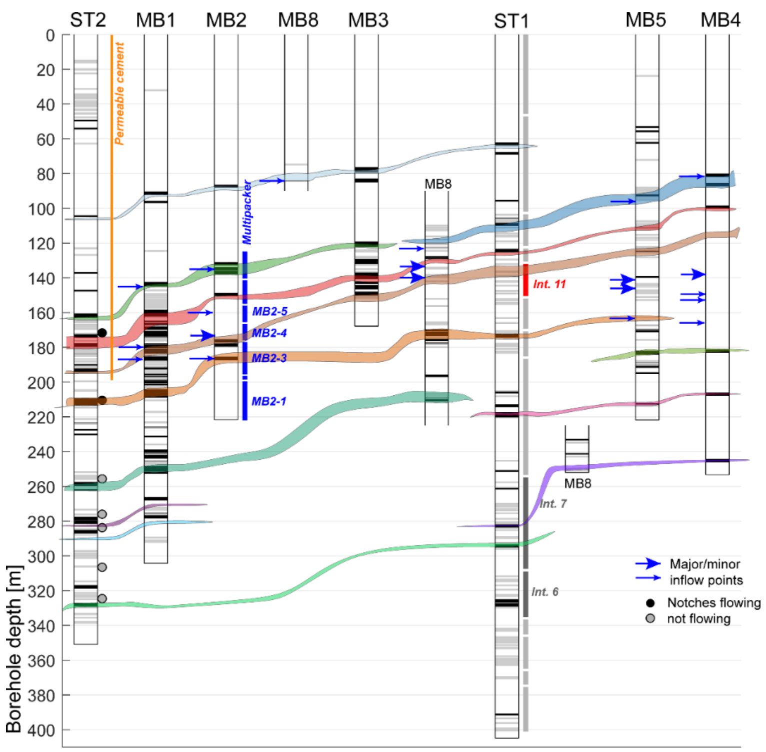

Figure 70: Borehole schematic including a geological interpretation of the ATV logs, as well as inferred hydraulic connections to the interval 11 in ST1. Vertical axis to scale, horizontal axis conceptualized.

5.1. State of borehole ST2

5.1.1. Insights from past hydrotests

Borehole ST2 is located on the northwestern side of the Geoenergy testbed, at the outer edge of the monitoring well array centred around the injection borehole ST1. The borehole has a diameter of 8.5 inches (216 mm) and reaches a depth of 350 m.

In 2020, prior to borehole completion, a series of double-packer hydraulic tests were carried out. The objective was to characterize the hydraulic properties of the intersected structures and to evaluate connectivity with nearby boreholes, in particular ST1 and MB1. The potential connection to MB1 was of special concern, as the trajectory of ST2 approaches within a few meters of MB1 at approximately 280 m depth, raising the risk of interfering with installed instrumentation.

The tests were performed using a double-packer system, enabling isolation and characterization of specific intervals. In total, 34 intervals corresponding to the principal geological structures intersected by ST2 were tested. The individual datasets were interpreted using analytical solutions to estimate transmissivity (T), storage coefficient (S), formation pressure, and steady state flow rates. The total natural outflow from ST2 during these tests averaged approximately 21 L/min. The dominant contribution (16.8 L/min) originated from interval T8 at 287 m depth, indicating a highly transmissive structure at this location.

Based on structural interpretation, the fracture system associated with Interval 11 in ST1 is most likely intersected by ST2 at interval F2a (190 m depth). This interval showed measurable hydraulic connectivity with both ST1 and MB1 (Figure 71), with an estimated transmissivity of $6.8E{-8}$ m²/s and a steady state flow rate of 0.05 L/min. At the time of testing, ST1 was not yet equipped with a multi-packer system, and therefore the observed connection could not be attributed to a specific interval within ST1.

Nevertheless, the system behaviour observed during the 2025–2026 BEACH injection campaigns is consistent with this inferred connectivity. In particular, the increase of 3 L/min at ST2 in response to a constant injection of 12 L/min in Interval 11 in ST1 provides evidence for a hydraulic link between the two boreholes. While this supports the existence of a connection, further investigation would be required to confirm whether it is specifically associated with interval F2a or with another transmissive feature intersecting ST2.

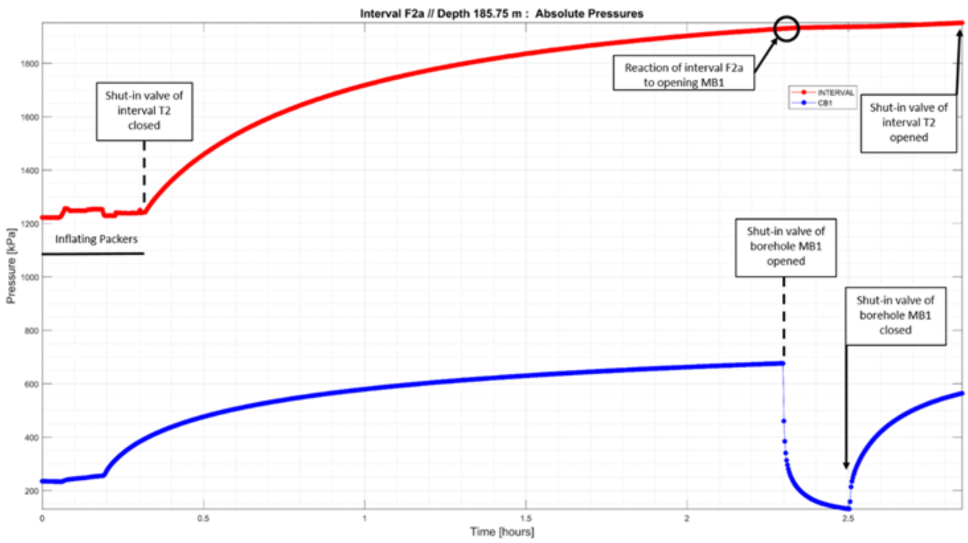

Figure 71: Pressure evolution during the double-packer test in interval F2a (185.75 m depth). The red curve shows the pressure response within the isolated interval, while the blue curve represents pressure measured in borehole MB1 (CB1 sensor). The steady pressure increase reflects injection into the interval. Opening of MB1 at ~2.3 hours induces a pressure drop in MB1 and a simultaneous change in slope in the interval response, indicating hydraulic connectivity between F2a and MB1. Subsequent closure of MB1 results in pressure recovery.

5.1.2. Results from Cement Bond Log (CBL)

Following these tests, ST2 was completed with a steel casing and subsequently cemented. However, the cementation proved to be only partially effective. In high-flow zones, the cement was diluted and failed to properly bond to the casing. Attempts to seal these leaks with cement epoxy were only partially successful. To assess the integrity of the cementation, a cement bond log (CBL) was run on June 8, 2021, using a 2SAA-1000/F sonic probe.

For the purposes of the ZoDrEx project (Christe and Meier, 2023) only a preliminary interpretation was carried out. The results (Figure 72) show a clear contrast between the upper and lower sections of the borehole. Above approximately 197 m depth, the signal suggests poor or absent cement bonding, with casing joints visible at regular intervals (~3 m). This suggests that the casing is largely decoupled from the surrounding formation in this depth range.

Below approximately 917m depth, the signal indicates sections with improved cement bonding. However, the quality remains heterogeneous and locally inconsistent. Even in these deeper sections, the cementation cannot be considered fully effective in ensuring hydraulic isolation.

As part of the ZoDrEx project, the casing was later notched at seven depths using mini-turbine drilling to establish controlled hydraulic connections between the ST2 and the surrounding formation at selected intervals. GES subsequently performed stimulations in the five deepest notched intervals. These operations, however, resulted in unintended hydraulic communication between notches through the annulus, most likely caused by partial fracturing of the cement. As a result, the notches are no longer hydraulically isolated and are effectively connected along the annular space. The shallowest two notches have been identified as active inflow zones based on DTS measurements (see Figures 6 and Figure 70).

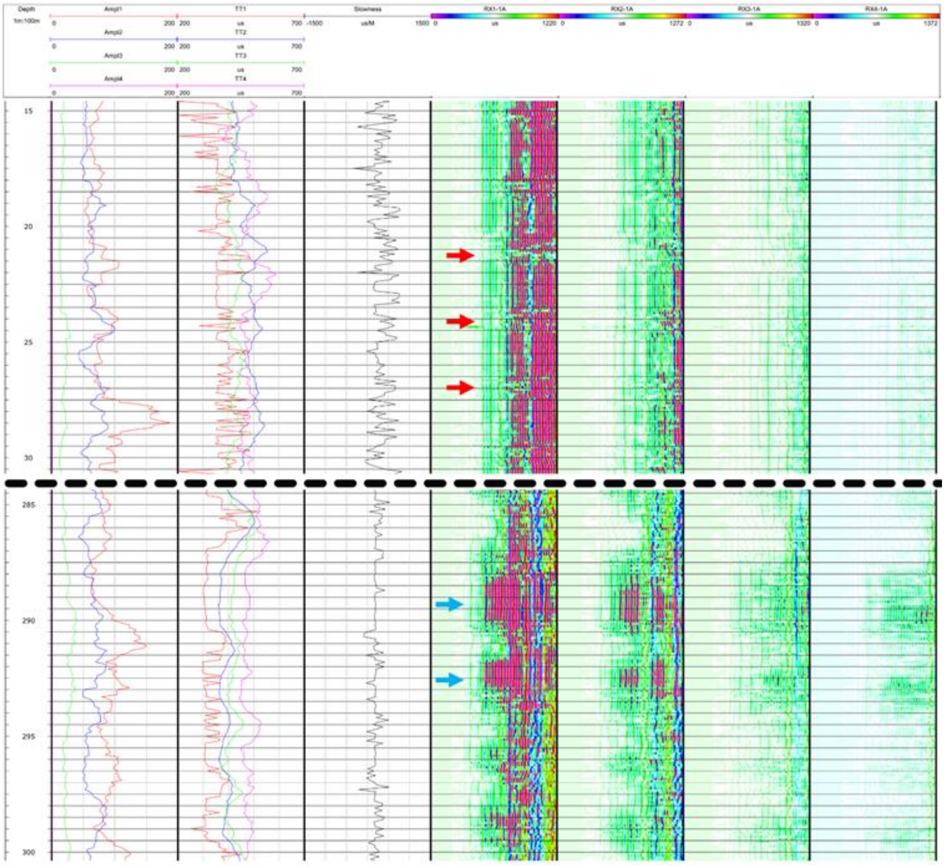

Figure 72: Cement Bond Log (CBL) results for borehole ST2, shown for two representative depth intervals separated by the dotted line. The upper panel (15 to 30 m depth) displays high-amplitude responses and regularly spaced features (red arrows) corresponding to casing joints, indicative of poor or absent cement bonding. The lower panel (295 to 300 m depth) shows localized zones of reduced amplitude (blue arrows), interpreted as intervals with improved cement-to-casing bonding. Overall, the log indicates weak cementation in the upper section and heterogeneous, locally improved bonding at depth.

5.1.3. Evaluation of ST2 as production/injection borehole

Previous operations have demonstrated a hydraulic connection between Interval 11 in ST1 and ST2. During the BEACH injection campaigns, a constant injection rate of 12 L/min in ST1 led to an increase of approximately 3 L/min at ST2 after about 15 days of continuous injection. At present, ST2 produces 19 L/min, which is comparable to the average steady state flow rate of 21 L/min measured during the 2020 hydraulic testing campaign. This suggests that most of the fractures intersecting the borehole are actively contributing to the overall flow.

A hydraulic connection is confirmed by the tracer test results described in Section 3.3.5. However, these show that the tracers arrive at the borehole strongly diluted implying that a direct connection between the borehole is relatively weak. Geochemical and microbial data (Section 3.3.7) aligns with these observations and suggest that the **connectivity from ST1 to ST2 is weak implying that ST2 may not be suitable for cross-hole injection.**

Using ST2 as a production well in Phase III of the BEACH experiment would require isolating the contribution of individual fractures, particularly those hydraulically connected to ST1. Given the current condition of the casing and annulus, this would likely necessitate removal of the existing casing and full recompletion of the borehole, and the installation of a multi-packer system similar to that in ST1, or alternatively a simpler triple-packer configuration. Such operations would require mobilization of a drilling rig, involve non-standard procedures, and pose significant technical and logistical challenges, particularly in the installation of packers in an 8.5" borehole.

For Phase III, it has been therefore decided not to remediate ST2. The required interventions would likely incur costs comparable to, or exceeding, those associated with drilling new boreholes, primarily due to mobilization and operational complexity. Retaining ST2 in its current state nevertheless provides continued value, as it enables ongoing monitoring of key processes (e.g. Section 3.2.6), including far-field hydraulic response, tracer transport, and geochemical evolution.

5.2. Project plan for Phase III

5.2.1. Phase III objectives

Our experimental results and the numerical models based on them highlight that several FTES design options would lead to higher efficiencies of the FTES:

1) Higher injection and production rates (i.e. interval transmissivities) may enhance reservoir temperature, increase heat storage efficiency and reduce heat losses around the borehole. We will address this by choosing an injection interval that has higher transmissivities or by combining several intervals for heat storage. Our current preferred choice is to **change to Interval 13**, which has higher transmissivity than interval 11. The optimal configuration will be chosen as part of Phase III.
2) Modelling results indicate that thermal insulation of the injection borehole would further enhance thermal storage efficiency. Technical solutions for **thermal insulation**, which can be retrofitted to the injection borehole ST1 are currently being developed. We foresee performing a comparable hot water injection, as done in Interval 11, using thermal insulation.
3) Clearly, the most promising way to enhance heat storage efficiency is to add multiple boreholes to the injection/production borehole – so-called helper wells – which control the flow from and to it. Provided there is a good connection between these boreholes, the flowrate in the production borehole can be enhanced by forcing flow to it from the helper wells. This addresses the limited backflow observed in ST1 after injection. We plan to **drill additional boreholes**, one of which is used as helper borehole in a cross-hole configuration. The location and orientation are part of a refined design in Phase III, but has already been discussed in the modelling studies (Section 5.2.3).

5.2.2. New borehole layout

As discussed above, a key operational aspect of Phase III will be drilling new boreholes. We foresee drilling a new ca. 200 m long injection/production borehole ST3 to investigate how a crosshole storage configuration can improve the efficiency of FTES. Additionally, monitoring boreholes will be drilled to enhance the existing monitoring system around the new borehole ST3.

A potential preliminary setup for additional boreholes is shown in Figure 73. The new injection/production borehole ST3 may be drilled from the SE end of the test niche of the GTB at least 20 – 25 m away from ST1. The borehole would be maximally 200 m long potentially shorter. The seismicity cloud shows that the borehole would be intersected by the fracture network illuminated by the seismicity between 100 and 150 m depth (the latter being the depth the seismicity takes off from interval 11). Thus, the hydraulic distance between ST1 and ST3 (i.e. the distance along the fracture that are actively flowing) is 25 – 50 m, which is deemed an ideal distance for heat storage provided there is a good hydraulic connection (Rondon and McClure, 2023). In the following Section 5.2.3, the optimal location and distance is evaluated using numerical models. At shallower depths, the borehole also intersects a very transmissive structure known from ST1 interval 13 and from its intersection at the tunnel wall at about 2000 m (GB1, Section 3.2.6), which offers an additional test interval for FTES. Further, it intersects a very tight section at the shallowest depth (<80 m), which may be used to create a new heat exchanger in near-intact rock using hydraulic fractures and proppants. The borehole diameter may be 96 mm (as in the SPINE boreholes BFE05 and BFE06, Bröker et al., 2026) or larger (as in the GTB). The borehole will be equipped with a triple packer system that allows us to flexibly isolate the target interval (two lower packers) and to control flow and pressure above the injection interval (with shallowest packer).

Additionally monitoring boreholes are required because the new borehole ST3 lies outside the existing monitoring network around ST1. As the monitoring and modelling results above show, evaluating the performance of a FTES requires at least a comprehensive temperature monitoring system based on DTS. At the same time, it requires inferring active flow paths using deformation monitoring such as DSS. Additionally, induced seismic hazard management requires that seismicity around both production/injection boreholes ST1 and ST3 are recorded. Figure 73 shows that the seismicity produced by past stimulations in interval 11 can reach easily beyond the current monitoring network. **In summary, these monitoring boreholes will host at a minimum: seismic sensors, DTS cables and DSS/DAS cables.**

Note that the borehole layout discussed here is preliminary and a final design will be done as part of Phase III, during which the borehole spacing, orientation, etc. are optimized for enhanced heat storage efficiency, and the monitoring layout is optimized to meet the monitoring requirements. Furthermore, drilling several boreholes gives us flexibility in choosing which one is more suitable as production/injection borehole or as monitoring borehole based on subsequent hydraulic testing of drilled boreholes. Thus, the ultimate design will depend on the findings during the drilling campaign.

Activities in Phase III will further be accompanied by monitoring of geochemistry, noble gases and microbiology, which give important insights into the impact of thermal energy storage on environmental parameters.

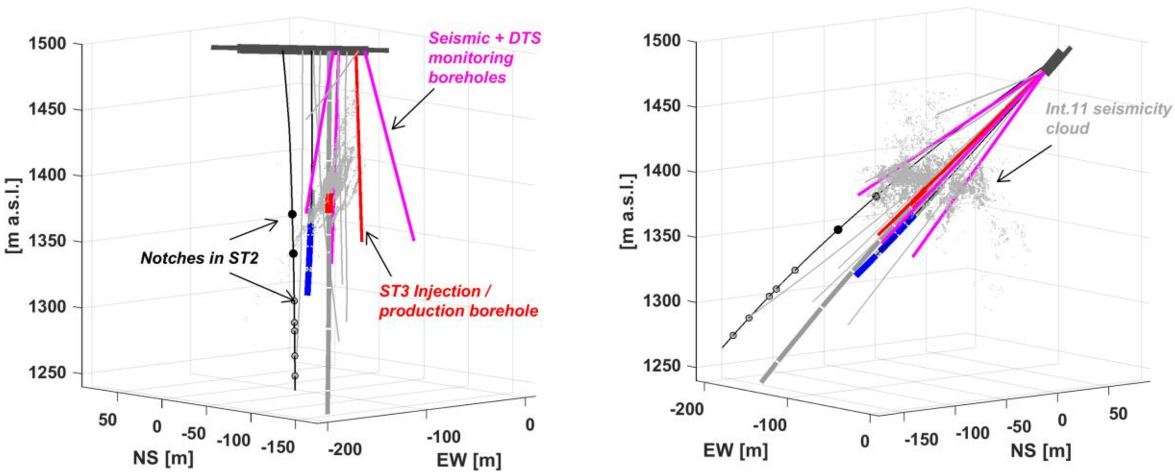

Figure 73: Geoenergy testbed (GTB) including proposed new boreholes in red (injection/production boreholes) and pink (new monitoring boreholes). Only one possible borehole configuration is shown here. More options are elaborated on in Figure 74.

5.2.3. Proposed locations for ST3 borehole

The configurations for the new ST3 injection/production borehole have been investigated by testing two different locations and sampling the permeability along them to identify possible suitable injection intervals; their permeability profiles are then compared with ST1 to assess which configuration would be likely to present the highest transmissivity.
The first explored configuration foresees positioning of the ST3 injection borehole as defined in the previous Section 5.2.2, almost parallel to the ST1 borehole and 25 meters away from the latter in SE direction. A second possible location for ST3 is investigated by positioning the borehole 50 meters away from ST1 wellhead in the NE direction, with azimuth and dip defined so that the new borehole would cross the fracture cluster almost perpendicularly with respect to the direction of the existing boreholes. Both explored configurations consider a maximum borehole depth of 200 meters.

Table 8: investigated locations for the ST3 borehole, distance in Southeast direction, azimuth and dip.

Borehole	Distance from ST1 (SE) [m]	Azimuth [°]	Dip [°]
ST3_SE	25	235	40
ST3_NE	-50	200	40

Table 8 summarizes the placement of the proposed ST3 boreholes, while a representation of the testbed comprehensive of the laboratory tunnel, the mapped fracture network, the existing boreholes and the proposed ST3 boreholes is shown in Figure 74.

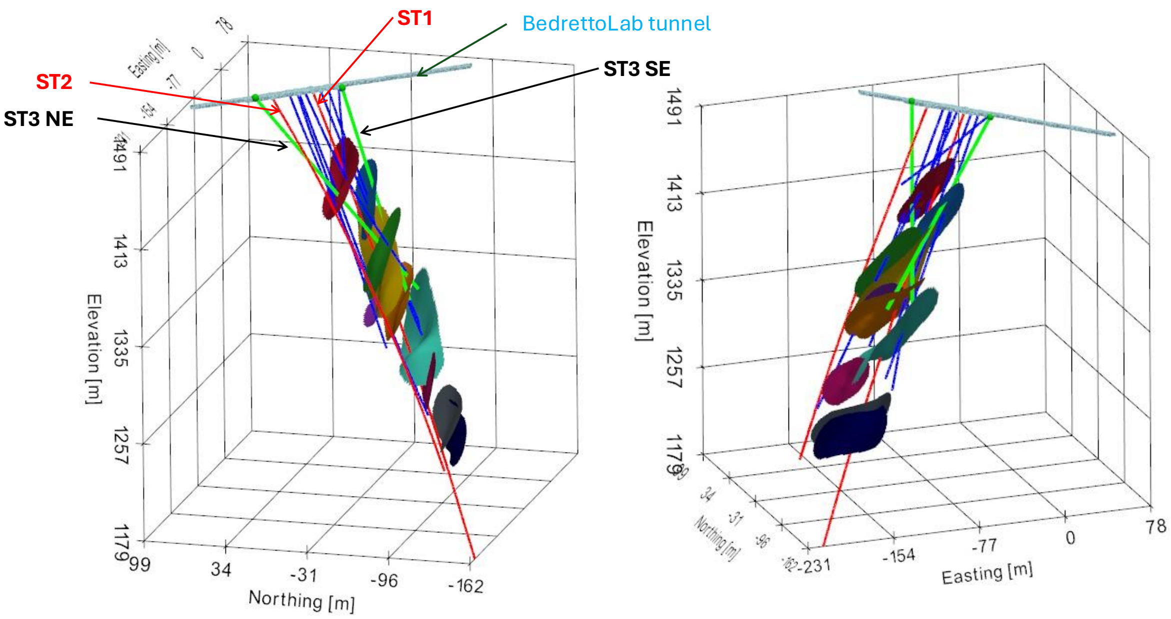

Figure 74: Test bed including the laboratory tunnel and mapped fracture zones, existing injection-production boreholes in red (ST1 and ST2) and proposed placements for the ST3 borehole in green.

The investigated placement for the ST3 borehole, considering a maximum depth of 200 m, is carried out by ensuring that each borehole would cross the mapped fracture network to maximise the possible transmissivity profiles along its depth.

Permeability is plotted against borehole depth in Figure 75 for ST1 and the proposed placements of ST3. The current high-transmissivity injection interval used for the experiments in ST1 can be identified between depths of ca. 130 and 150 meters. The SE option for ST3 seems to present the highest permeability interval between ca. 100 meters and 140 meters of depth, essentially aligning with the same high-transmissivity zones encountered and measured along ST1. Given the reduced distance between ST1 and ST3_SE (25 meters) and the coupled high permeability sampled at these depths, an injection interval between 115 and 140 meters would be suitable to reduce the flow resistance to which the water flow would be subjected during cross-hole experiments.

For what concerns the NE option for ST3, the highest permeability is sampled at ca. 150 meters in depth, with absolute values close to ST3 NE and ST1; nevertheless, this placement for the borehole does not present a high permeability zone extending for more than 20 meters, unlike the ST3 SE option.

The present analysis would suggest that the SE option for the ST3 borehole, as already presented in the previous section, could be suitable for cross-hole experiments and possibly provide more flexibility for the choice of different injection intervals, as the sampled high-permeability zone extends from about 115 m down to 140 meters in depth.

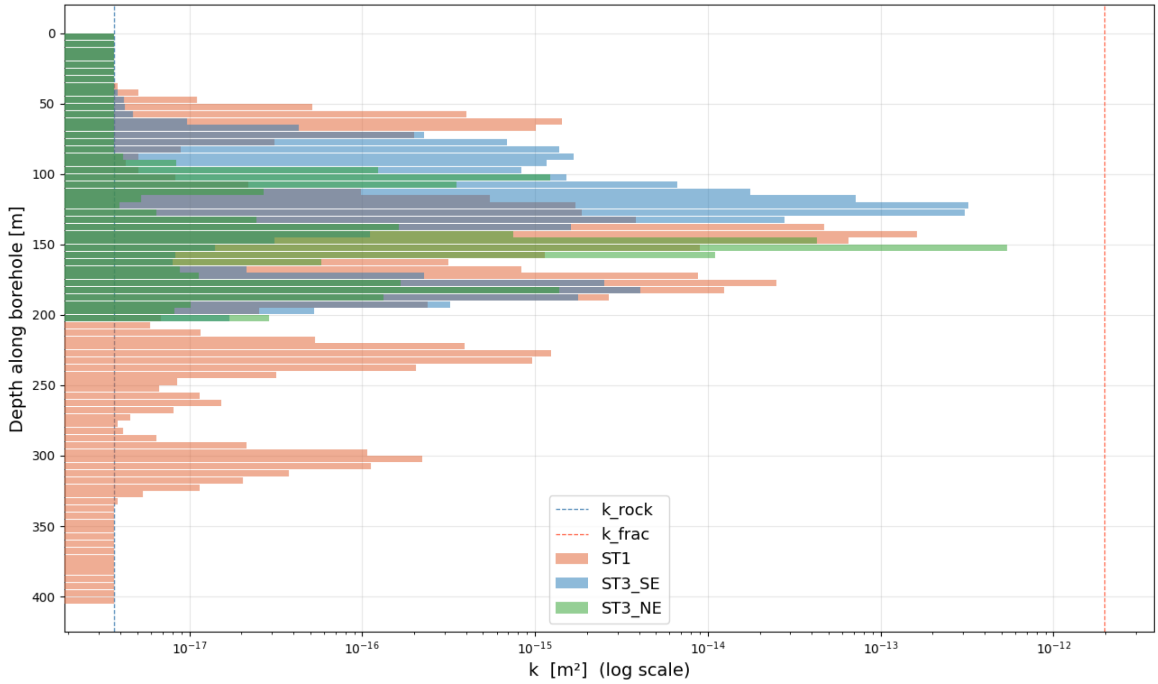

Figure 75: Plot of log-scale permeability (k $[m^2]$) along the depth of ST1 and the investigated placements for ST3 (SE and NE direction).ST1 is coloured in orange, while the south-eastern option for ST3 is coloured in blue and the north-eastern option for ST3 in green.

5.2.4. Planned heat storage experiments

Several design considerations (interval length/transmissivity, thermal insulation, multi-borehole configuration) can lead to improvements of the overall efficiency of FTES, and many of these will be implemented and tested as outlined in Section 5.2.1. To validate the potential of these design consideration as compared to our experimental finding and model predictions so far in Phase II, it is important that heat storage experiments are conducted in a comparable and reproduceable way. Thus, we will follow our current approach and conduct experiments in a down-scaled manner in terms of time (i.e., injection duration) and scale (injection rate/volume) and follow a near identical experiment procedure as in the Phase II experiments:

1) Hot water injection for 14 days
2) Shut-in for 7 days
3) Production for 7 days
4) Hot water injection for 14 days
5) Immediate production for 14 days
6) Daily cycles of hot water injection for 14 days
7) Immediate production for 14 days

While the constant rate injections of step 1 – 5 mimick storage from a constant heat source (e.g. excess heat from a waste incineration plant), the cyclic injection of step 6-7 mimick storage of intermittent energy (e.g. a power to heat case).

The procedure will be performed at least once more in a single hole configuration in another interval (likely interval 13) and with a thermally insulated injection borehole. Additionally, it will be performed in a cross-hole configuration using at least on additional helper well both for production (during heat injection) and injection (during heat production), which corresponds to the “full-use helper borehole” case modelled in Section 4.2.4. Analysis of the experimental results will inform, if more short-term (i.e. 14

days) storage cycles or longer-term (e.g. two months) are more valuable to be performed for further evaluation of the FTES concept. This also depends both on project progress and the time available.

5.2.5. Detailed time plan

Until end of June, the borehole insulation design is finalized by solexperts and implemented in July. We will then change the borehole interval. In August, we start the experimental procedure in the single-hole configuration as outline in Section 5.2.4 lasting until end of October. During this time, the design of additional injection/production boreholes is finalized supported by sensitivity analysis using numerical models. Procurement of drilling activities will be finalized in by end of October. Drilling will start in November an last until mid-February. During this phase, boreholes will be characterized including also hydraulic characterization that will inform about the connectivity to ST1. Based on these results the final design of borehole completion (i.e. which borehole is most suitable as ST3, which sections are packed-off for injection). Borehole completion of monitoring boreholes and injection borehole ST3 is finalized by end of March. This also includes the integration of data streams and visualizations into our BedrettoLab monitoring systems. Starting in April, experimental work will start. The actual hot water injection may be preceded by hydraulic stimulations, if we find that transmissivity and connection between boreholes could benefit from it.

5.2.6. Project risks

The plans, outlined in this Section, may be compromised by potential unforeseen circumstances. In Table 9, we elaborate on operational, logistic and organizational risks and what mitigation action we foresee to reduce these risks.

*Table 9: Risk associated with Phase III activities. Colors denote **low**, **medium**, **high*** probability or consequences.

Risks related to implementation	Probability	Consequence	Assessment and mitigation
No suitable drilling company avaible in the required period			Fallback options are to adopt the drilling program to the availability of companies and drill rigs or discuss project delays until availability
Available drill rigs not suitable for the tunnel			Adjust drilling program and adopt project goals
Procurement procedure too long			Discuss project extension or adopt project goals
Drilling costs too high			Reduce drilling program to shorter boreholes.
Scheduling conflicts with other projects			As a flagship project in Bedretto, we will give BEACH priority for the implementation and conduction. From experience of parallel projects in the BedrettoLab during the last years, we a used to find satisfying solutions to schedule sequentially where parallel conduction deems impossible.
Lack of personnel			The Bedretto Team is a consortium of different groups in the Departement of Earth and Planetary Sciences and has reliable partners from established companies. With this solid base of manpower, we will assign people from the larger team in case individual people from the proposed staff become unavailable.
Risks related to technical limitations or problems			
No insulation options found			An insufficient insulation of the injection and production systems may compromise the proof of efficiency. Yet, with lower temperatures measured downhole, the demonstartion of injecton, storage, and recovery will still be achieved at lower downhole temperatures. Further, modelling showed that in the upscaled case, insulation may not be mandatory.

Insulation tools stuck in ST1			Here, we see a low probability, but a high impact on the system integrity and project goals. A stuck may eventually make an injection impossible. But circulation and production from the well will most likely still be possible and projects goals can partly be fulfilled. Alternatively, the new boreholes could be used to establish a heat exchanger
Drilling targets not achieved (e.g. in terms of borehole length)			In case drilling targets can not be fully achieved due to geologial risks, the project objectives will be adopted.
Technical difficulties changing to interval 13			Sliding-sleeves may not be operational anymore because of corrosion or other reasons. In case the interval cannot be changed, we can choose other intervals or stick with interval 11. The effect of transmissivity cannot be investigated on storage efficiency may not be possible unless the new boreholes are used for storage experiments.
Failure of T monitoring system			The Bedretto Geoenergies testbed includes a comprehensive multi-sensor monitoring system. May of the sensor chains are redundant and failure only affects parts of the sensor chains. Acquisition of sufficient data to achieve teh project goals is most liek still possible.
Failure of deformation monitoring system			
Failure of seismic monitoring			
Risks related to experiment setup / geothermal testbed			
No or limited hydraulic connection between ST1 and ST3 found			From the EGS project VALTER we have all equipment on-site to conduct hydraulic stimulation to create or enhance the hydraulic connections.
No thermal break-through between bore-holes			This may be related to a limited connection between boreholes. However, it may also be related heat storage along the flow paths between the boreholes, which is desired.
Induced seismicity is higher than anticipated and even hazardous			Induced seismicity has been analysed as part of past stimulations. A traffic light system will be in placed building on the multi-layer seismic montoring network (see report).

6 FTES potential in Ticino and extrapolation methods for Switzerland

6.1. Status of current work on site characterization

The method presented here is designed as a versatile and time-efficient tool for deriving a reliable first-order estimate of heat storage potential, based on standard borehole-derived parameters and a computationally efficient numerical model.

6.1.1. Geological constraints

To evaluate the feasibility of FTES outside the Bedretto Laboratory, data collection includes all the thermal and geological information available for Canton Ticino.
For the thermal data:

- Point measurements of heat flux (mW/m²) in Canton Ticino, obtained from the Global Heat Flow Database (https://doi.org/10.5880/fidgeo.2024.014) (a).
- The Swiss geothermal map at a 1:500,000 scale, representing heat flow density (mW/m²) (Federal office of topography swisstopo, 2024), cropped to the borders of Canton Ticino (a).
- Laboratory measurements of thermal conductivity (W/m·K) for different local rock types (b,). Conductivity was measured both parallel and perpendicular to schistosity, on dry and saturated samples (Thüring, 2003).
- https://s.geo.admin.ch/yw42eygks5tf
- https://www.oasi.ti.ch/web/energia/mappatura-teleriscaldamento.html

The geological data collection includes all boreholes reaching bedrock in Canton Ticino (c, GESPOS Database, SUPSI). Given the large number of boreholes (824 wells in total), a set of filtering criteria was established, based on length, lithology and schistosity orientation.

- Length: the hole must have at least 30 meters of bedrock depth.
- Schistosity orientation: the selected sites must be representative of the regional geology of Ticino, accounting for the diversity of tectonic settings. The chosen areas, reflecting large-scale and geologically representative domains, include: (i) the vertical and (ii) horizontal foliation zones of the Lepontine Dome, both representative of northern Ticino; (iii) the Monte Ceneri area, representative of the Southern Alps; and (iv) the Centovalli sector, in the vicinity of the Ivrea–Verbano Zone.
- Lithology: based on the conductivity measurements of Thüring (2003), preferred rock types are metamorphic rocks, mainly schistose gneisses and mica schists. Figure 77 illustrates that thermal conductivity in schistose rocks is higher along their schistosity planes, with water playing a key role in facilitating heat transfer. Measurements on mica schists indicate that thermal conductivity along the schistosity planes nearly doubles in saturated samples compared to dry ones. In the case of gneisses, it rises from 2.34 to 4.38 W/m·K, highlighting the significant influence of moisture on heat transfer (Figure 77).

Seven boreholes met all the criteria (Figure 76d). Table and the following section contain all the relevant information about the selected boreholes.

Table 10: Selected boreholes for assessing the feasibility of FTES development in Canton Ticino.

	Borehole	Coordinates	Depth [m]	Average dip	Info
1	Biaschina	2709259, 1142052	650	20°-50°	Access denied
2	Chiggiogna	2706215, 1147354 (?)	301	15°-30°	Not found
3	Gnosca	2721434, 1122293	100	60°-75°	Obstructed
4	Monte Carasso	2719650, 1116485	86	40°-70°	Not found
5	Sementina	2718615, 1115565	130	45°-65°	OPTV done
6	Camedo	2690837, 1112142 (?)	32	25°-60°	Not found
7	Mezzovico	2715632, 1106090	194	30°-50°	OPTV planned

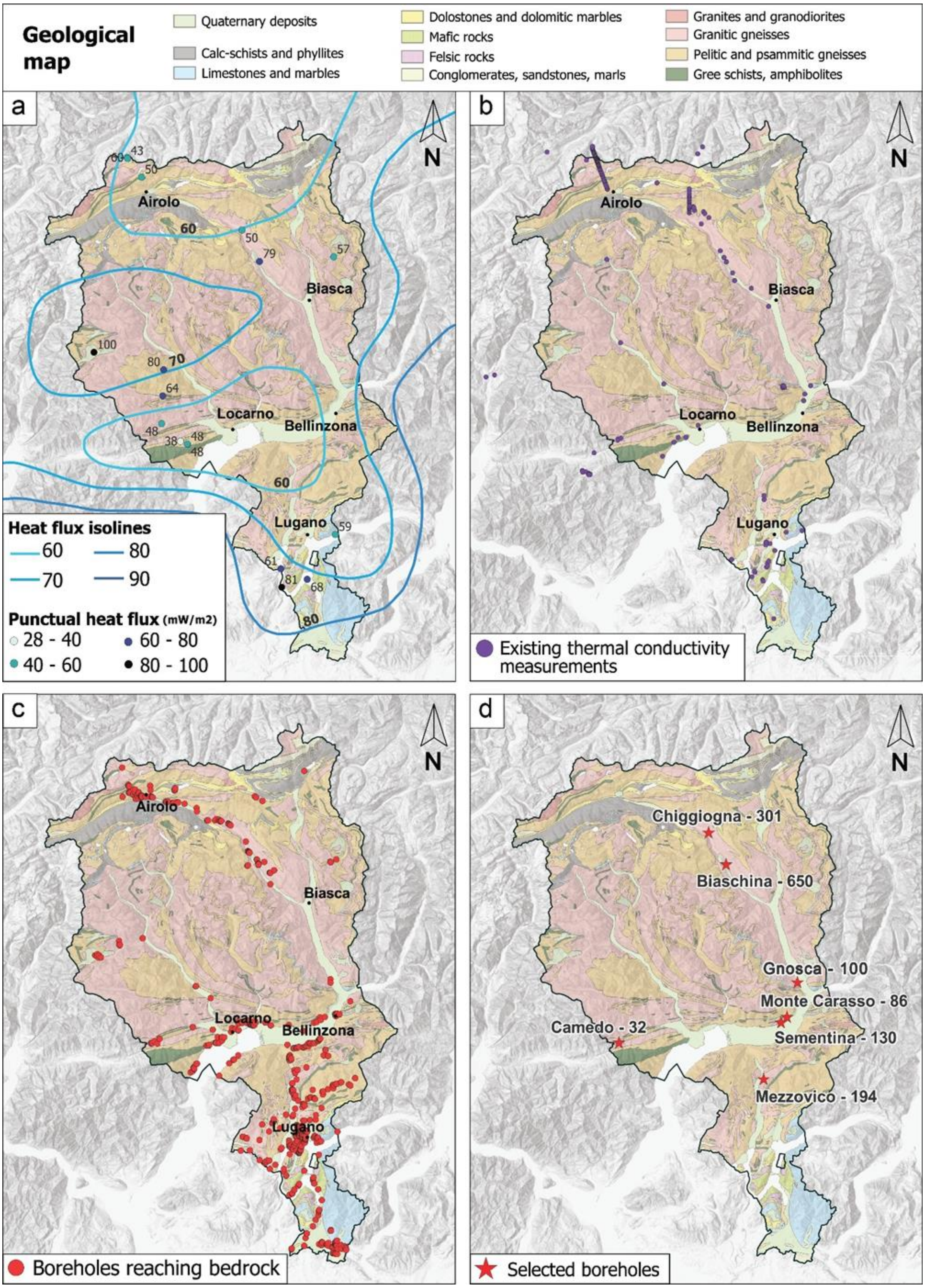

Figure 76: simplified geological map of Canton of Ticino with a) heat flux isolines and punctual heat flux data (IHFC database and swisstopo, 2024); b) existing thermal conductivity measurements from Thüring, 2003; c) boreholes reaching bedrock (GESPOS database, SUPSI); d) selected boreholes for the evaluation of FTES potential.

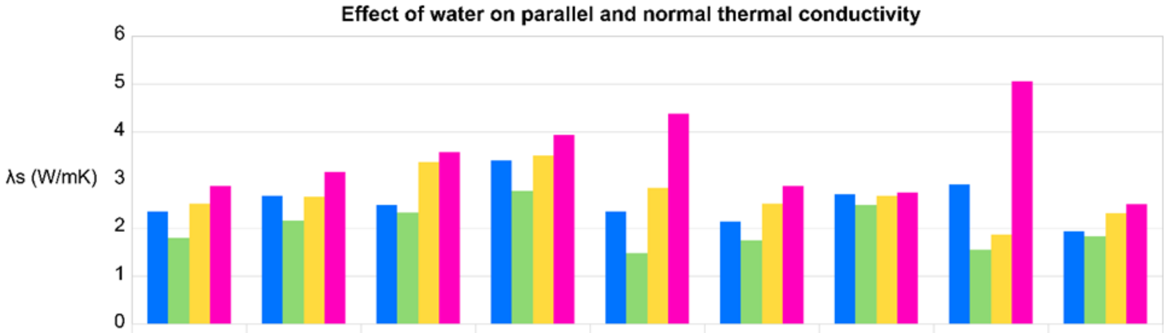

	Amphibolite	Gneiss	Granitic gneiss	Coarse-grained gneiss	Schistose gneiss	Granite	Marble	Micaschist	Hbl micaschist
Dry parallel	2.35	2.68	2.48	3.41	2.34	2.13	2.71	2.91	1.94
Dry normal	1.80	2.15	2.32	2.78	1.48	1.75	2.49	1.55	1.84
Wet normal	2.51	2.66	3.38	3.51	2.84	2.51	2.68	1.86	2.31
Wet parallel	2.88	3.17	3.59	3.94	4.38	2.88	2.75	5.06	2.50

Figure 77: laboratory measurements of thermal conductivity both parallel and normal to schistosity from different rock types (Thüring, 2003). The maximum thermal conductivity occurs in saturated mica schist samples measured parallel to the schistosity planes, with schistose gneisses exhibiting the next highest values.

Boreholes Biaschina (1) and Chiggiogna (2) were drilled between 1971 and 1973 as part of the AlpTransit project. Both required multiple field campaigns to be located, as the coordinates reported in the stratigraphic logs were only approximate. According to the available documentation, both boreholes are still open.

The Biaschina (1) borehole has been identified on site but cannot be accessed as it lies on private property. SUPSI sent a formal access request to the landowner in 2025, but the owner showed no interest in granting permission to assess the current condition of the borehole. The main lithology is the Leventina gneiss. Part of the core samples and several thin sections are stored at the Natural History Museum in Basel.

The Chiggiogna (2) borehole is located near an abandoned quarry and was approximately pinpointed through the analysis of historical aerial photographs and statements from residents. Its exact position has not yet been confirmed in the field, despite the use of ground-penetrating radar and a metal detector, because metallic waste (a boiler and old quarry equipment) located near the presumed position of the well interferes with the detection. Clearing the waste material would be feasible if the costs were covered by the relevant stakeholder, as the municipality lacks the financial resources to support its removal. As for the Biaschina borehole, the stratigraphic documentation confirms the main lithology is the Leventina gneiss.

The idea of looking for the Gana Bubaira borehole (2704069, 1154210, 1570 m length) in the field was also considered. This borehole was drilled in 1964–65 at Gana Bubaira, a mountain locality in Blenio at an altitude of 2.091 m a.s.l., to assess the extent of the Piora-Mulde, a water-saturated dolomite that had halted excavation work on the Gotthard Base Tunnel. However, SUPSI decided not to invest time in the search, as no documentation could be found to determine whether it was cemented. Additionally, the borehole bottom stops approximately 50 meters short of the top of the Gotthard Base Tunnel, so any heat flow measured in the borehole would likely be influenced by the presence of the tunnel and the heat it releases. Another consideration is the disturbance caused by topography: the subsurface heat flow pattern is distorted near topographic features, an effect that is amplified in valley areas and reduced in mountainous regions. For this reason, SUPSI opted for boreholes located near valleys to obtain thermal properties as close as possible to undisturbed conditions, such as Biaschina and Chiggiogna boreholes. Access to both boreholes would be highly valuable for characterizing the thermal behavior of the Leventina gneiss in depth. To date, no thermal conductivity measurements exist at such depths across the entire Ticino region, and Biaschina is the only borehole reaching 200 meters below sea level. Gaining access to perform an OPTV measurement would allow the integration of actual thermal properties into the ongoing numerical simulations of the project, improving their accuracy and producing results as close as possible to real conditions.

Boreholes Gnosca (3), Monte Carasso (4) and Sementina (5) were drilled in 1993 as part of the AlpTransit project, related with the Gnosca–Sementina railway tunnel. The main lithotypes are gneisses, micaschists and amphibolites of the Lepontine dome, whose foliation becomes nearly sub-vertical in this area. Gnosca borehole (100 m) has been located, but at a depth of 11 m it is intersected by a metal bar, making it impossible to perform the OPTV measurement. Monte Carasso borehole (86.25 m) could not be found despite multiple field surveys. It was likely cemented during riverbed restoration works, as suggested by historical aerial photographs. Sementina borehole (130 m) was identified and logged with OPTV in February 2026. Currently, it is the only borehole with an OPTV dataset, collected to integrate real physical parameters into the numerical models. The cores from Monte Carasso and Gnosca boreholes are now stored in the new core storage facility in Saint-Ursanne (JU), while those from Sementina were disposed of because they were not in good condition.

Camedo borehole (6) has not yet been found in the field. A new survey is planned for spring 2026 to try to locate it. The main lithologies reported in the documentation are migmatitic and anatectic gneisses.

The Centovalli area exhibits relatively higher heat flow values compared to other parts of Ticino, as it lies within the Ivrea-Verbano zone. Although the borehole is relatively shallow compared to the other selected sites, it may still provide valuable insights into the distribution of heat flow.

Mezzovico borehole (7) has been located and inspected with a borehole camera. It is in good condition, and OPTV logging is scheduled for late spring 2026. Based on the stratigraphic logs, the main lithologies consist of predominantly massive micaceous and quartzitic gneisses from the Ceneri area, with localized fractures.

6.2. Methodological approaches to evaluate the FTES potential

All relevant data from the selected boreholes must be extracted and parameterized for direct implementation in numerical simulations. The geological data includes fracture spacing, position along the borehole, thickness (aperture), and orientation.

The objective is to process rock properties and fracture density derived from borehole data and translate them into input parameters for a CFD-based continuum model (Figure 78; see also Section 4.3). In this approach, the fractured rock mass is represented through a relative permeability profile defined along the borehole axis (Z-axis) and is normalized to the [0,1] range. This profile is estimated from the spatial distribution, density, and thickness of fractures intersecting the borehole, thereby accounting for the vertical heterogeneity of hydraulic properties. Following the heat storage experiments conducted at the Bedretto Lab, the relative permeability profile was then calibrated by matching model outputs to observed pressure, temperature, and flow rate data from the hydraulic tests. The calibrated permeability profile thus provides a reference framework for constraining permeability distributions in other boreholes (Figure 78), such as *Sementina*, based on the position and characteristics of fractures along the borehole.

To this end, two complementary approaches are proposed: (i) a fracture-based approach, relying on fracture orientation and spacing, and (ii) a caliper-based calibration approach.

At present, the *Sementina* borehole provides the most comprehensive dataset and is therefore the most suitable candidate for testing numerical models on real-case conditions, beyond the Bedretto dataset. In particular, it intersects multiple fractured zones characterized by variable thickness and intensity.

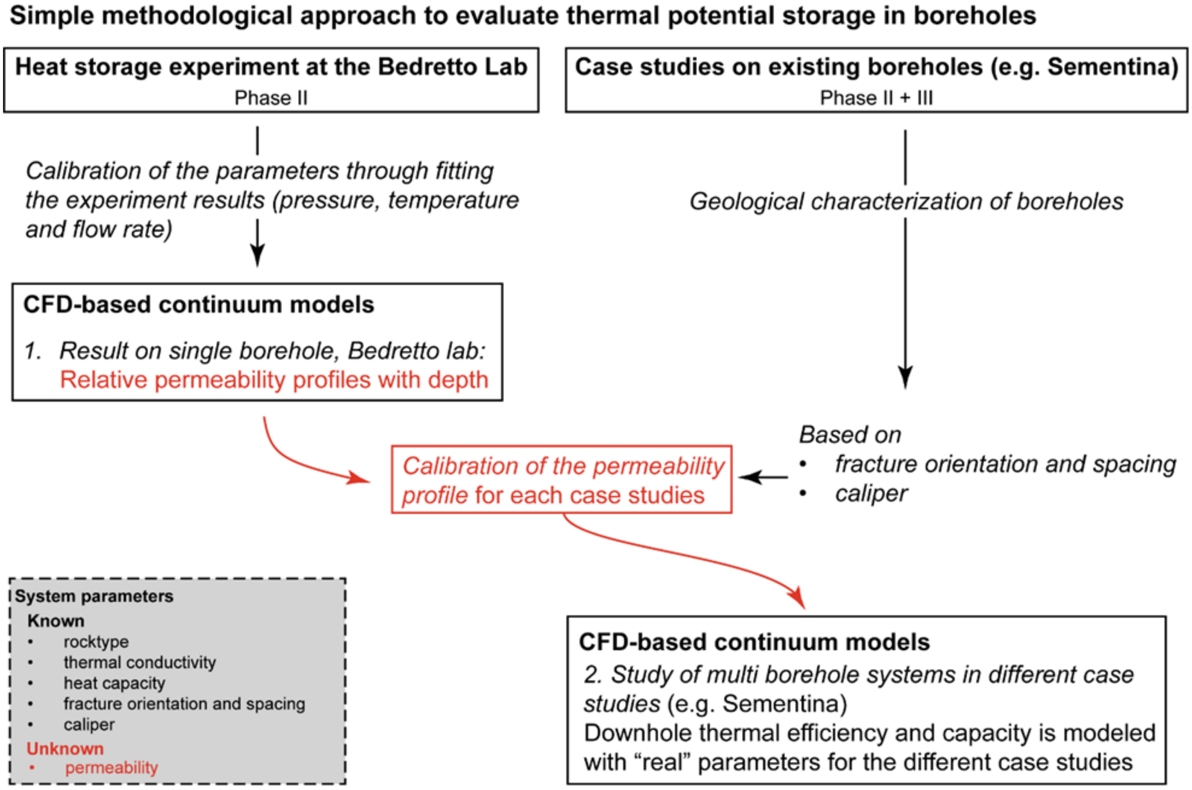

Figure 78: methodological approach to evaluate the thermal potential storage in boreholes. The main goal is to calibrate the permeability profile along hole for each case studies to evaluate the feasibility of FTES potential in other areas of Canton Ticino and in Switzerland.

6.2.1. Fracture orientation and spacing approach

The first proposed approach consists of discretizing the rock core along the Z-axis every 10 cm and estimating the fracture number and thickness (m) for each interval. The position and thickness of the fractures are extracted from core images and from stratigraphic logs. The 10 cm discretization step was defined according to 1 voxel of the CFD-based continuum model. A finer discretization would significantly increase computation time without improving the result significantly. Figure 79 represents the approach of the fracture discretization. This approach may overestimate the number of fractures, as new fractures commonly develop during the extraction of the core from the borehole.

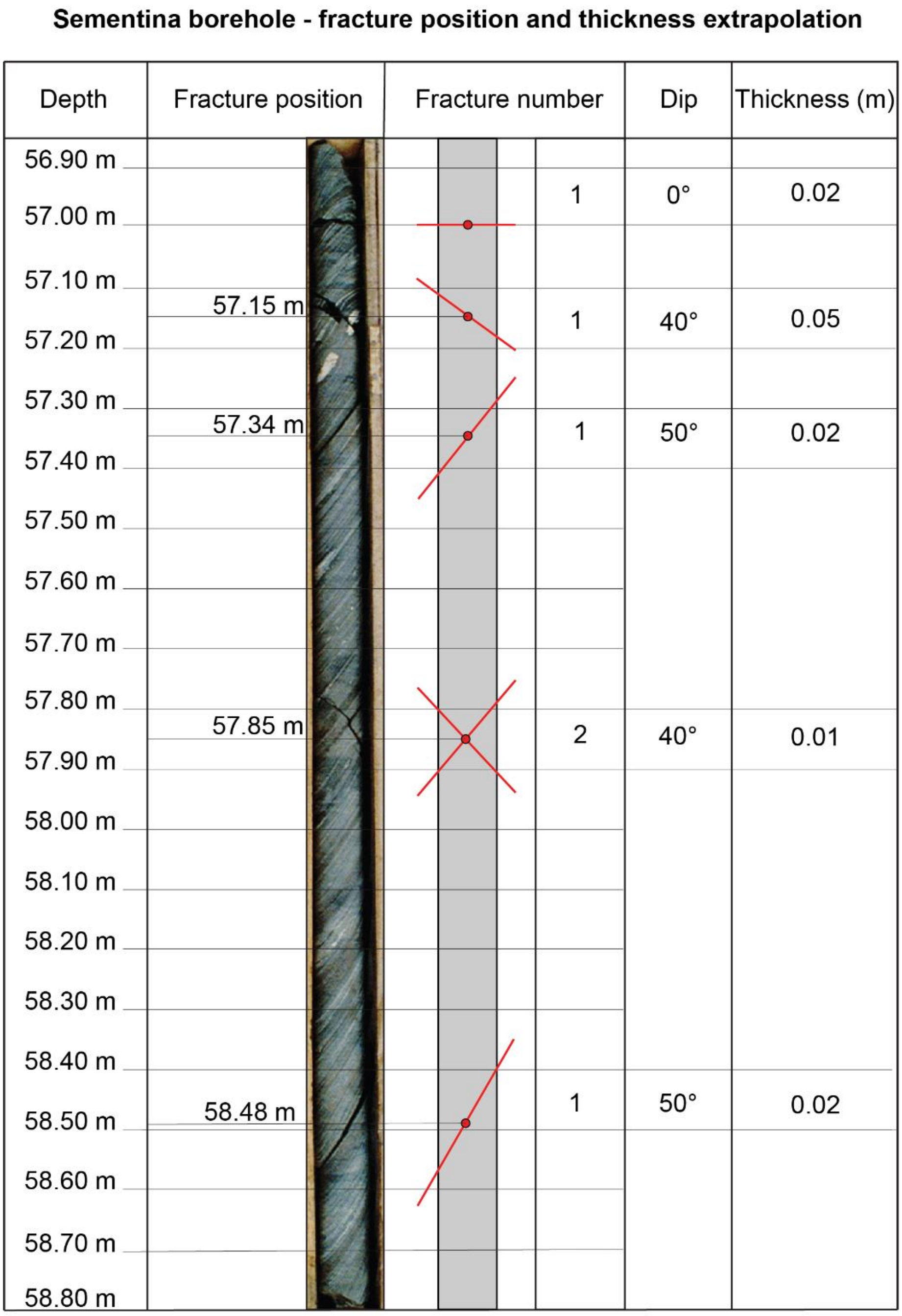

Figure 79: Example of fracture discretization approach on the Sementina core. The dip value is given from the stratigraphic log, while fracture thickness is visually estimated.

6.2.2. Caliper calibration approach

The second proposed approach, currently under development, uses caliper data from the *Sementina* OPTV survey for the location and magnitude of borehole irregularities, such as fractures and constrictions. Since we can compare the caliper profiles with those of the borehole ST1 of the Bedretto lab, this approach ensures that the profile is both representative of the specific case and comparable to a standard reference (Figure 80).

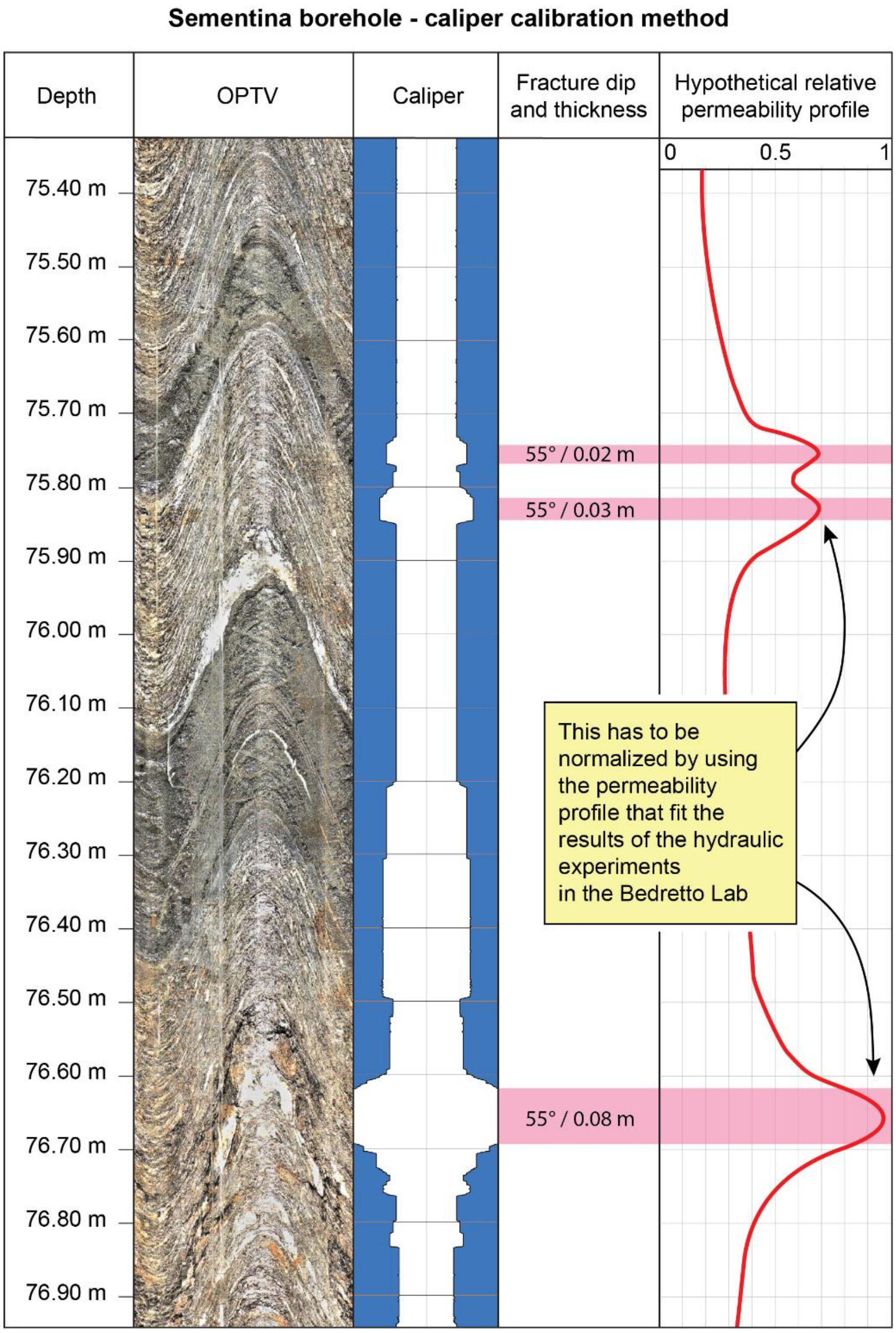

Figure 80: Fracture characterization using caliper measurements to obtain a site-specific, normalized permeability profile along the borehole, based on the position and extent of the fractures.

6.3. Energy-economic approach

Meetings with AET were conducted to define a workflow for integrating Fractured Thermal Energy Storage (FTES) into the energy market. The primary objective is to store energy in FTES systems connected to the same electrical productions as hydroelectric or photovoltaics power plants. Connection to this network would enable an optimized and balanced use of energy production.

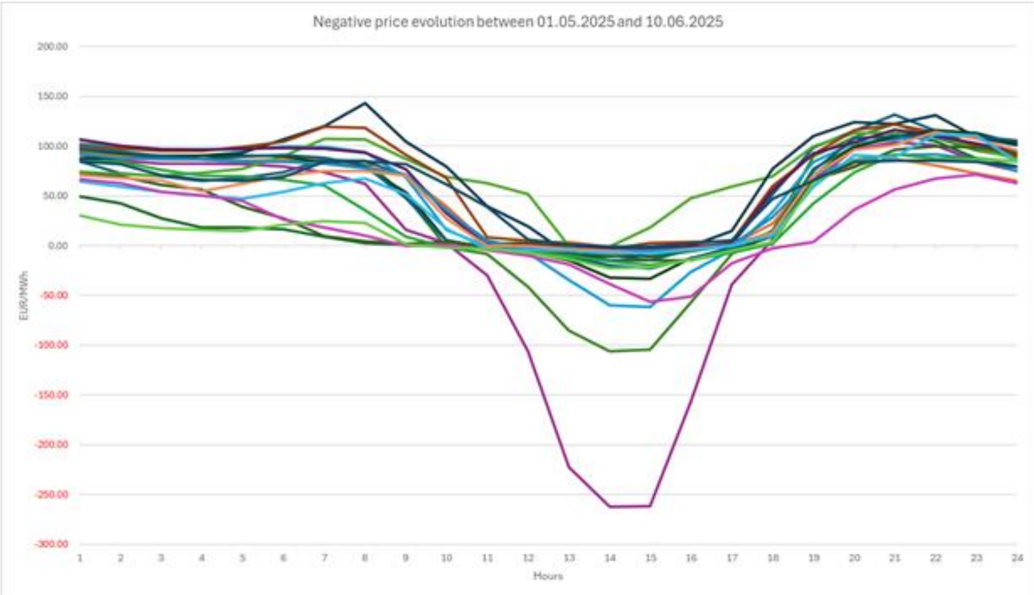

Figure 81: Hourly variation in electricity prices, illustrating the systematic decrease during periods of peak solar energy production.

Within this framework, AET considers FTES as an energy consumer. Electricity availability and pricing are independent of the geographical location of the FTES within Switzerland, as free-market prices are uniform across the national grid. Prices are determined on a day-ahead basis by the Swiss electricity market and vary hourly. Under conditions of expected overproduction, electricity prices could fall to very low levels and, in some cases, even turn negative. As illustrated in Figure 81, negative price periods occurred frequently between 01.05.2025 and 10.06.2025. During this spring period, typical daily price patterns ranged from 50–100 EUR/MWh between 19:00 and 09:00, decreasing to values as low as –250 EUR/MWh between 13:00 and 16:00. This implies that, during the daily peak production periods, FTES systems can effectively be paid to consume energy. What happens, for example, with large-scale photovoltaic systems (which therefore sell electricity on the open market) is that it is more cost-effective to switch off the inverters rather than feed electricity into the grid.

Stored thermal energy is subsequently recovered as hot water (the so-called “P2H”, power-to-heat) and later supplied to district heating networks. In this context, FTES acts as a heat producer, selling thermal energy to district heating operators, typically under long-term contractual agreements. In such a case, to minimize thermal losses along pipelines during the heat supply, the proximity between the FTES installation and the heat distribution network is critical.

For the implementation of the technology, a key parameter is the threshold electricity price below which energy storage in FTES becomes economically viable. Figure 82 outlines the proposed workflow to determine this price threshold, which depends on several factors that are currently under investigation and will be quantified during Phase III of the project:

- **Downhole efficiency and storage capacity**, particularly in realistic multi-borehole configurations.
- **Operational strategy for energy charging**, including intermittent (“opportunistic”) injection during low or negative price windows versus buffered storage (e.g., via surface boilers) enabling continuous injection.

- **Uphole efficiency and heat delivery performance**, including thermal losses and system integration with district heating networks.

These parameters are strongly site-dependent and therefore require case-by-case optimization to balance geological constraints with surface infrastructure performance. This dependency will be systematically investigated in Phase III, focusing on the site described in Section 1. In particular, the *Sementina* borehole will be used as a main and focalized reference case study, in combination with the TERIS district heating network in Bellinzona, which recovers and supplies to many users thermal energy generated from a waste-to-energy plant (Figure 83). In this case, the thermal energy stored could come from industrial waste heat, but also from surplus electricity on the grid (P2H).

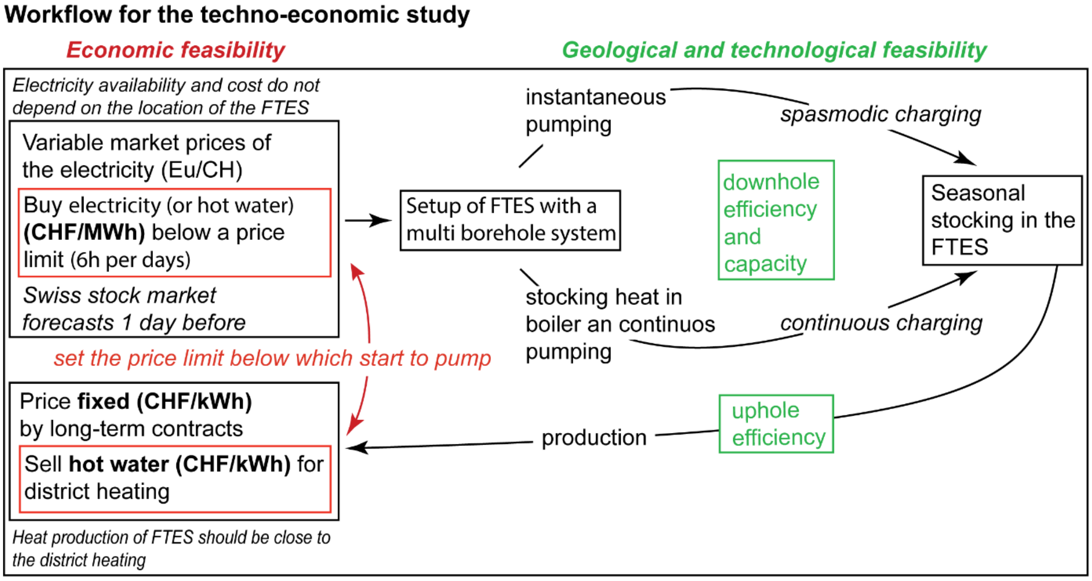

Figure 82: Framework for system analysis, developed with AET, to quantify the techno-economic feasibility of FTES implementation.

Figure 83: TERIS district heating network in Bellinzona showing the location of the Sementina borehole (source: OASI). Its proximity to the network makes it a suitable case study, analysed following the workflows presented in Figures 46 and 48.

6.3.1. Techno-economic exploratory analyses for Phase III Development

To initiate the preliminary technical and economic analyses of the project and to immediately establish benchmarks and a basis for discussion with AET, a well-established technology was adopted, both from a modelling and application perspective, namely borehole heat exchanger (BHE, i.e. closed-loop double-U) field. These initial assessments, which lay the groundwork for Phase III by testing models and methods and providing a preliminary understanding of the STES, were carried out under the assumption of hypothetical yet realistic technical and economic operating conditions.
Specifically, a seasonal cycle was assumed, consisting of a four-month summer phase for ground charging and a four-month winter phase for discharging. The system considered consists of a BHE field composed of 30 drilling, each 100 m deep, arranged to enable seasonal thermal energy storage in the subsurface. During the summer period, the field is operated in charging mode, with thermal energy injected into the ground at a rate of 250 kW and a supply temperature of 75 °C. Following a standby period, the system is operated in discharging mode during the winter season, when thermal energy is extracted from the subsurface over four months, targeting the same thermal power of 250 kW, with a delivery temperature of 40 °C. This operating condition may realistically represent, for example, a Power-to-Heat (P2H) or waste-to-heat (W2H) application during the summer period, coupled with heating in buildings or greenhouses during the winter season.
For this specific condition, it was possible to define the overall geothermal efficiency, defined as the ratio of the thermal energy extracted to the thermal energy input into the system. In particular, due to the progressive thermal saturation of the soil, it was not feasible to inject the full amount of thermal energy as planned. Similarly, during the discharge phase, it was not possible to recover all the stored energy, due to a thermal soil depletion. The amount of thermal energy that can actually be recovered therefore depends largely on the required and specified temperature levels, which in turn depend on the intended use of the heat (heating buildings, heating greenhouses, preheating processes, etc.).
Based on these energy quantities, a preliminary economic assessment was carried out, considering both capital expenditures (CAPEX) and operational expenditures (OPEX), and defining a simplified cash flow. In particular, on the one hand, a cost of electricity was assumed for the charging phase using electrical resistance (Power-to-Heat, P2H); on the other hand, the heat selling tariff required to ensure a positive Net Present Value (NPV) was identified as a key parameter. A difference of approximately 0.15 CHF/kWh between purchased electricity and sold thermal energy gave a positive NPV (dynamic energy prices were not considered).
It should be noted that the results obtained are purely preliminary: no sensitivity analyses or parametric scenarios have yet been considered, such as those related to borehole depth, spacing, or geothermal gradient. Indeed, this technology serves only as a benchmark and not as the primary focus of investigation within the BEACH project.
These results have already been presented in a technical meeting with AET, with the aim of developing an initial familiarity with the concepts of Power-to-Heat (P2H) and seasonal thermal energy storage, as well as with electricity tariffs applicable to long-term (multi-month) P2H operation. Furthermore, discussions with project partners (SUPSI-ISAAC and SUPSI-MEMTi) made it possible to identify the baseline information required to structure a more comprehensive and detailed techno-economic analysis in Phase III. This will consider and further deepen a more realistic scenarios from simulation results of FTES.

7 Conclusions

In Phase II of the BEACH project, we demonstrated that the fracture thermal energy storage concept (FTES) in a simple single-hole configuration is technically feasible. Furthermore, we employed several numerical modelling strategies, with which we could explain the data observed. Based on these two important achievements, we have established a strategy to move forward within the next phase of the project.

Our **single-hole experiments** showed that it is technically feasible to store thermal energy in fractured crystalline rock under realistic conditions. However, significant thermal losses occurred in the tunnel (33%) and injection borehole (45%) due to missing thermal insulation, thereby limiting injection temperatures at the storage interval from ~80°C to 33°C. Recovery efficiency at the injection interval improved from ~6% to over 10% between cycles, indicating progressive reservoir conditioning, while elevated outflow temperatures confirmed sustained heat storage. The comprehensive monitoring systems confirmed safe operation and heat transport, and no thermal breakthrough was encountered. Seismicity remained minimal and localized. Geochemical and microbiological impacts were minor, but longer and hotter cycles would require further studies.

The **modelling studies** showed that continuum (CFD) and discontinuum (DFN) approaches can reliably reproduce pressure and temperature evolution during hot-water injections, with deviations below 10%. The models confirm that heat remains concentrated near the injection borehole and is strongly controlled by fracture networks, with enhanced storage capacity in stimulated zones. Significant heat losses along the borehole were also reproduced, highlighting the importance of proper insulation to improve storage efficiency.

Predictive simulations indicate that cross-hole configurations outperform single-borehole systems by enabling higher flow rates and greater energy recovery. However, performance is strongly controlled by fracture connectivity and transmissivity, thereby highlighting that the placement of a second borehole needs to be carefully planned. Further gains are expected from multi-borehole setups that actively control reservoir conditions. While current simulations provide valuable insights and scaling potential, further modelling and upcoming cross-hole experiments are needed to fully evaluate optimized reservoir configurations and long-term performance.

To go forward **with cross-hole thermal energy storage field experiments**, we decided to not pursue to idea of remediating the already existing borehole ST2, because required operations are likely more expensive and complex than drilling new boreholes. Current plans foresee drilling a new injection/production borehole placed such that connectivity to ST1 is optimized for cross-hole thermal energy storage. Additional monitoring boreholes are required to record temperature changes and to ensure seismic safety during operations. Additional technical solutions towards insulating the injection/production borehole(s) must be implemented.

To **extrapolate the FTES concept beyond the BedrettoLab test site**, seven boreholes were selected in Ticino from a data base of 824 boreholes. They are described in terms of fracture geometry and thermal properties to be implemented in numerical models for assessing first-order heat storage feasibility. In collaboration with AET, FTES systems were integrated into a techno-economic framework, where they are treated both as electricity consumers and heat suppliers. Ongoing analyses will identify the electricity price conditions, under which heat injection becomes economically viable.

8 References

Alcolea A.*, Carrera J. Difusión en la matriz. Formulación integro-diferencial. VII Simposio de Hidrogeología, Murcia (Spain), 2001

Brehme, M., Hertrich, M., Onishi, T., Hefny, M., Alcolea, A. R., Schenker, F., Grinaschi, A., Zavattoni, S., BEACH - Bedretto Energy Storage and Circulation of Geothermal Energy. (Interim Report to SFOE, 31.10.2024). ETH Zürich.

Bröker, K., Guglielmi, Y., Soom, F., Cook, P., Hertrich, M., & Valley, B. In situ quantification of fracture slip induced by hydraulic injections in a deep borehole: A comparison of two different borehole techniques. *Available at SSRN 5967430*.

de La Bernardie, J., Bour, O., Le Borgne, T., Guihéneuf, N., Chatton, E., Labasque, T., ... & Gerard, M. F. (2018). Thermal attenuation and lag time in fractured rock: Theory and field measurements from joint heat and solute tracer tests. *Water Resources Research*, *54*(12), 10-053.

Carrera, J., Sánchez-Vila, X., Benet, I. *et al.* On matrix diffusion: formulations, solution methods and qualitative effects. *Hydrogeology Journal* **6**, 178–190 (1998). https://doi.org/10.1007/s100400050143

Carrera, J.*, P. Gouze, M. Willmann, Y. Méléan, M. Dentz, T. Le Borgne, A. Alcolea, X. Sànchez-Vila. Memory Functions to Represent Transport Through Heterogeneous Media: Can They Make Physical Sense?. AGU Fall Meeting 2006, San Francisco, USA, 11-15 Dece

Ebert, A., & Sutter, E. (2023). Grosstechnischer Erdspeicher Flughafen Zürich in quartärer Rinne, Bericht zu Phase 1 geophysikalische Erkundung und Phase 2 Sondierbohrungen (Interim Report to SFOE, 02.10.2023). Zürich: C+P Sieber Cassina + Partner AG, Zürich.

Gholizadeh Doonechaly, N., Halter, T., Shakas, A., Hefny, M., Brehme, M., Hertrich, M., & Giardini, D. (2024). Thermal Energy Storage and Recovery in Fractured Granite Reservoirs: Numerical Modeling and Efficiency Analysis. *Geosciences*, *14*(12), 357.

Hibbard L, et al. Preliminary observations from a decameter-scale field test of fracture thermal energy storage: initial and induced in-situ stress and its impact on fluid flow. https://ssrn. com/abstract=5518007 (2025)

Klepikova, M., Méheust, Y., Roques, C., & Linde, N. (2021). Heat transport by flow through rough rock fractures: a numerical investigation. *Advances in Water Resources*, *156*, 104042.

Knobloch, K., Ulrich, T., Bahl, C., & Engelbrecht, K. (2022). Degradation of a rock bed thermal energy storage system. *Applied Thermal Engineering*, *214*, 118823.

Miller R.T., Delin G.N. (1994). Cyclic injection, storage, and withdrawal of heated water in a sandstone aquifer at St. Paul, Minnesota: Analysis of thermal data and non-isothermal modeling of short-term test cycles. U.S. Geological Survey, Open-File Report 93-435.

Meier, P., & Christe, F. (2023). ZoDrEx. Zonal Isolation, Drilling and Exploitation of EGS Projects (Final Report to SFOE). Zürich: Geo-Energie Suisse.

Nussbicker J., Mangold D., Heidemann W., Müller-Steinhagen H. (2003). Solar assisted district heating with duct heat store in Neckarsulm-Amorbach (Germany). ISES SOlar World Congress, Göteborg, Sweden.

Rondon, J., & McClure, M. (2023). Thermal heat storage in fractured reservoirs Geothermal energy storage systems (Final Report to SFOE, 02 March 2023). ResFrac Corporation, USA.

Schmidt Th., Müller-Steinhagen H. (2004). The central solar heating plant with Aquifer Thermal Energy Storage in Rostock. Results after four years of operation. EuroSun 2004, 5th ISES Europe Solar Conference, Freiburg, Germany.

Silva O., Carrera J., Kumar S., Dentz M., Alcolea A., Willmann M. (2009): A general real-time formulation for multi-rate mass transfer problems, Hydrol. Earth Syst. Sci., 13, 1399-1411

Zhou, R., Zhan, H., & Wang, Y. (2022). On the role of rock matrix to heat transfer in a fracture-rock matrix system. *Journal of contaminant hydrology*, *245*, 103950

Appendix

A1 - Complete DTS measurements

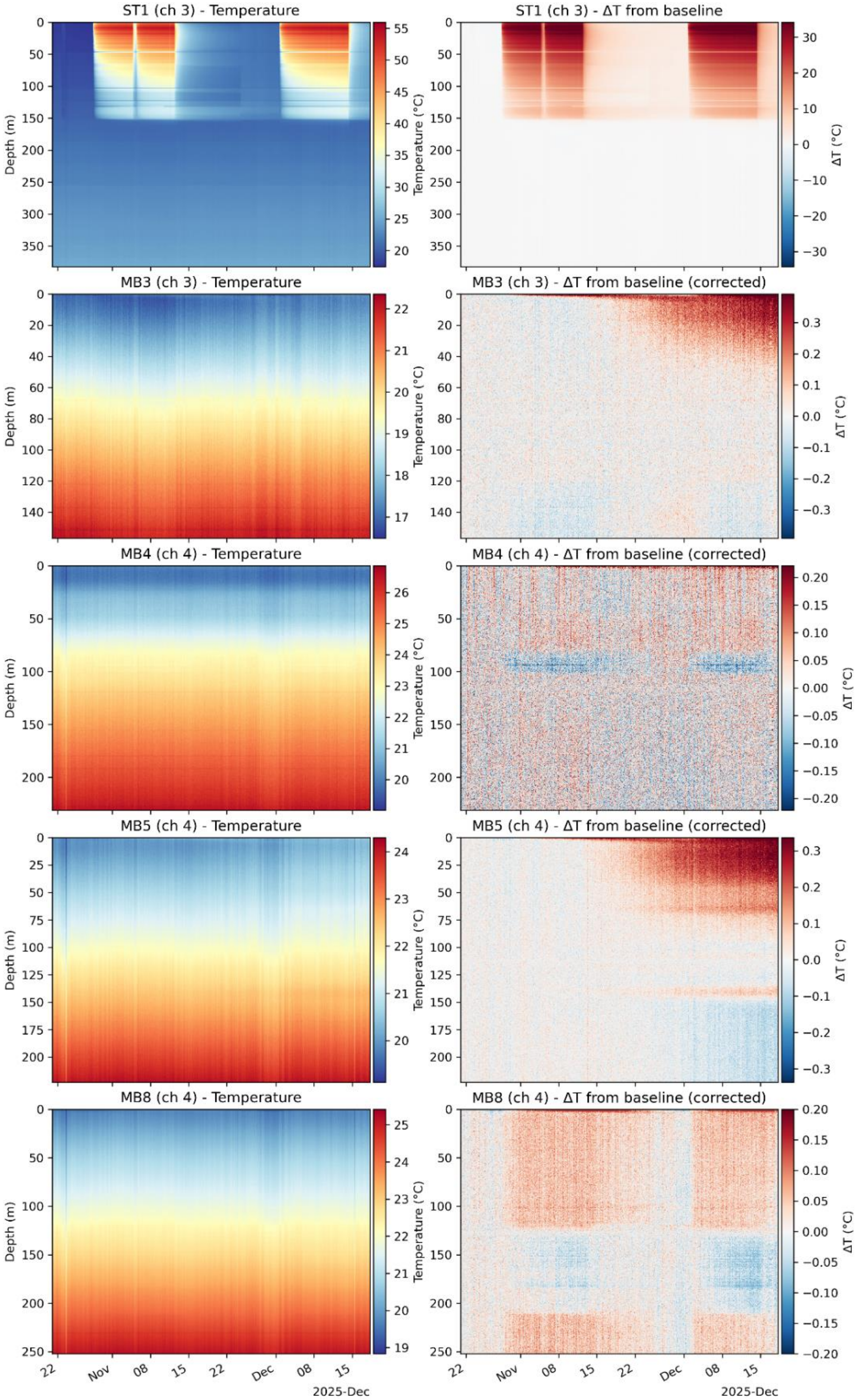

Figure 84: Complete DTS data from the two hot water injection cycles including absolute temperature as well as temperature change with respect to the beginning of the time window.

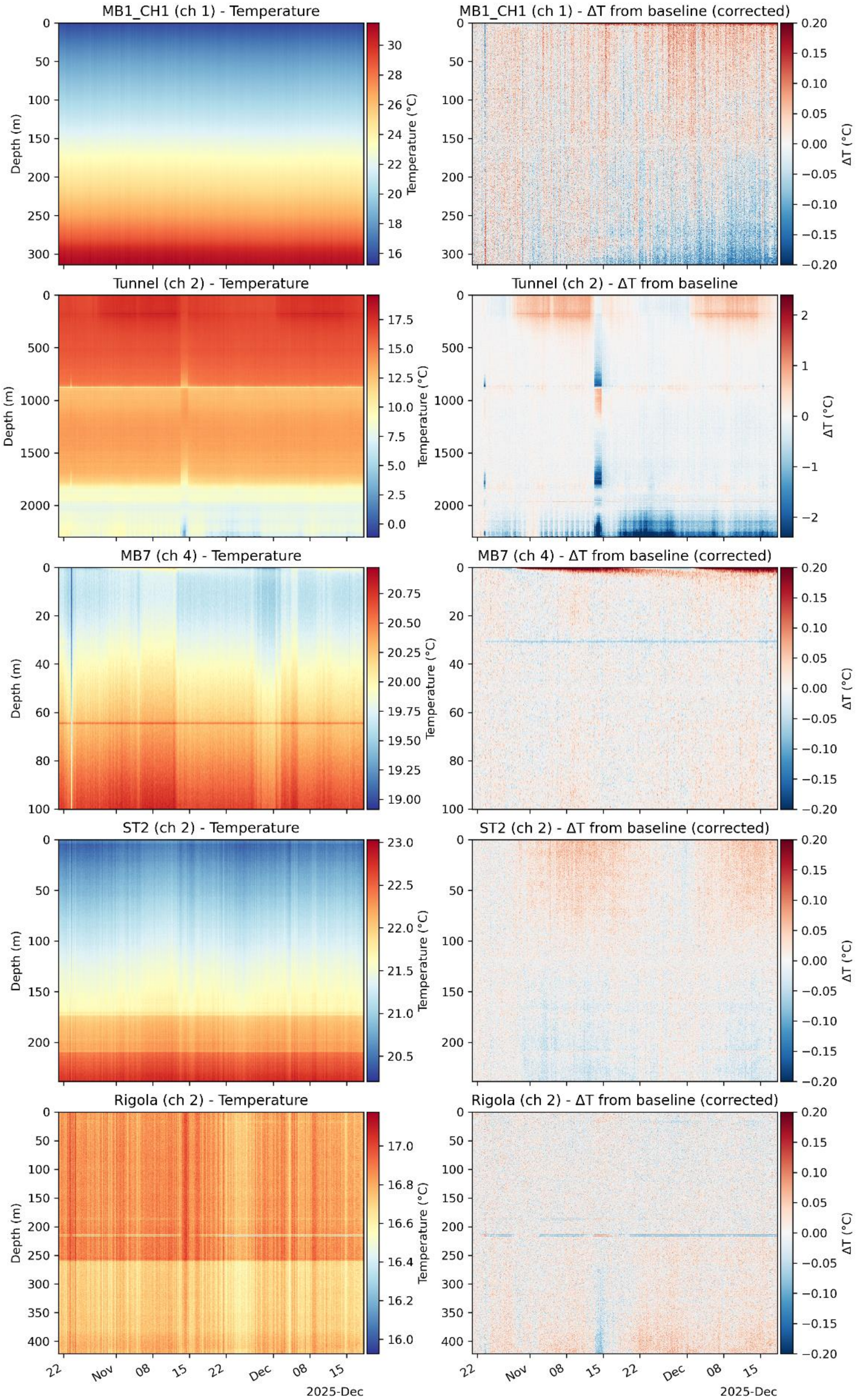

Figure 85: Complete DTS data from the two hot water injection cycles including absolute temperature as well as temperature change with respect to the beginning of the time window.

A2 - Continuum model – Spatial and temporal discretisation sensitivity analysis

To assess the model's performances, the influence of simulation time step and spatial discretisation are investigated with a sensitivity study, which is based on a case that refers to a continuous 120-day hot water injection. The sensitivity study foresees the identification of a proper temporal and spatial discretisation to ensure results independency.
For this sensitivity study, hydraulic permeability will be defined solely along the z-direction, which refers to elevation, in agreement with the profile presented in Figure 64 ("Z-profile").
Results will be evaluated calculating the error norms between temperature profiles along three "line" monitors, which span along the z-direction in the reservoir, as shown in Figure 86.

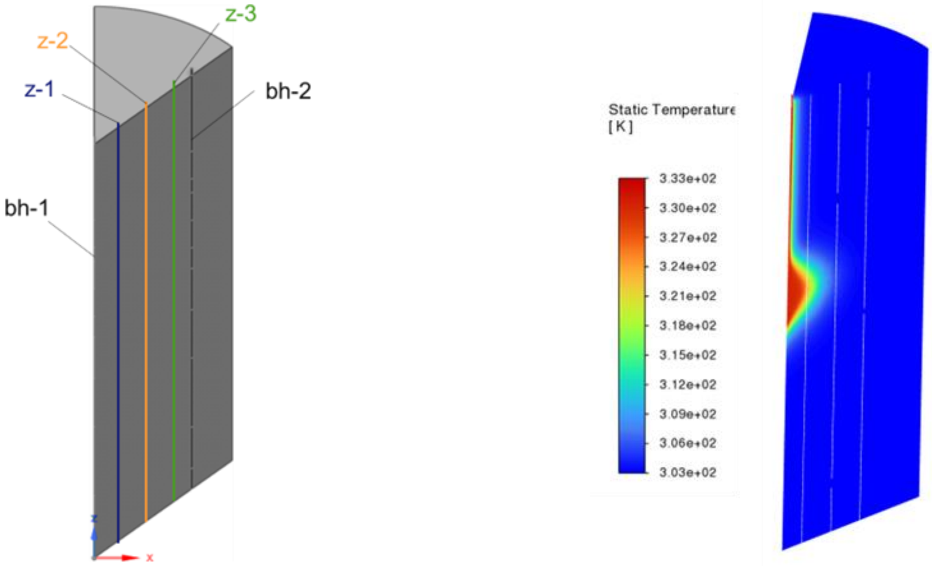

Figure 86: l.h.s) Cylindrical FTES domain with shown line monitors (z-1, z-2, z-3). r.h.s) Static temperature contour in the reservoir after a continuous 120-day charge phase.

The first step of the sensitivity study foresees the comparison between different time steps with fixed grid: the results presented below (see Figure 87) are related to a mesh with about ten million elements, while the transient solver is setup as a fixed CFL condition at 0.7, with imposed maximum timestep.
As shown in Figure 86, injection temperature from bh-1 slowly decreases until ca. 150 meters in depth (z-position), where it encounters the high permeability cluster already identified in the permeability estimation phase. This depth corresponds to the lower end of the injection interval 11 in ST1 in the BedrettoLab. At this depth, thermal energy diffuses through the reservoir along its radius; nevertheless, only the first z-line monitor (z-1), which is the foremost in vicinity with respect to the injection borehole, sees a significant increase in temperature, up until a maximum of $T_{max,z-1} = 325.7\ K = 52.55\ °C$.

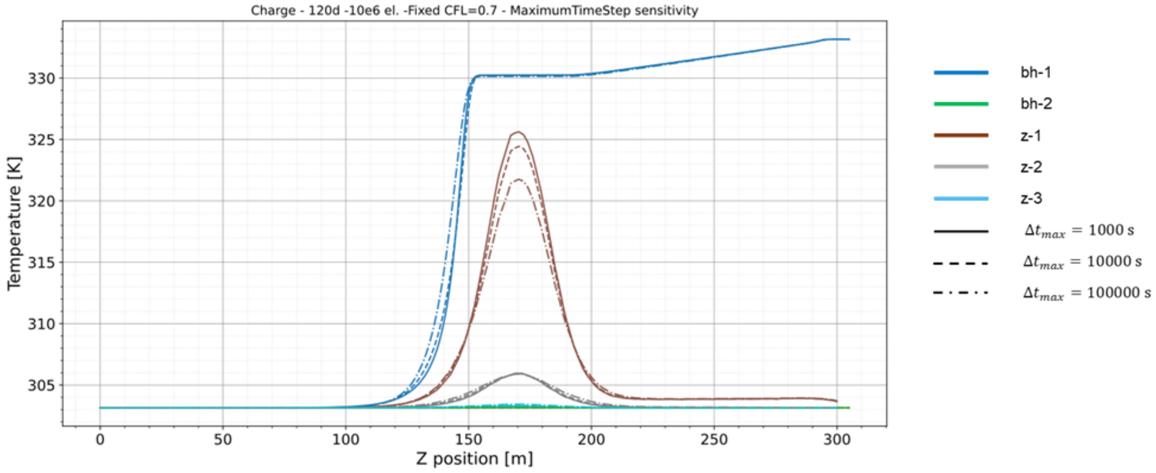

Figure 87: comparison of temperature profiles along bh-1, bh-2 and z-line monitors, for different maximum timesteps (1000 s, 10000 s, 100000 s) (Z-position of 300 m indicate the upper part of the computational domain).

Therefore, maximum timestep seems to have a much bigger influence on the z-1 line monitor where the "peak" temperature presents a difference of about $3\ K$ between $\Delta t_{max} = 1000\ s$ and $\Delta t_{max} = 10000\ s$: thus, for the next analysis, an intermediate timestep of $10000\ s$ $(2.7\ hours)$ is chosen.

With a fixed time step, now the computational grid has been increasingly refined up to the finest mesh sized 10 million elements, and results have been compared in terms of temperature profiles along bh-1, z-1 and z-2. Conversely, bh-2 and z-3 have been discarded from the analysis since almost no temperature gradient has been observed on them.

From Figure 88 it is possible to deduce that the spatial discretisation has a much lower effect on the temperature profiles in the reservoir if compared to the time step: in fact, temperature along z-1 presents a maximum difference of about $2\ K$ between the coarsest and the finest mesh. No significant differences have been noted for the different meshes, in terms of temperature, along both bh-1 and z-2 monitors.

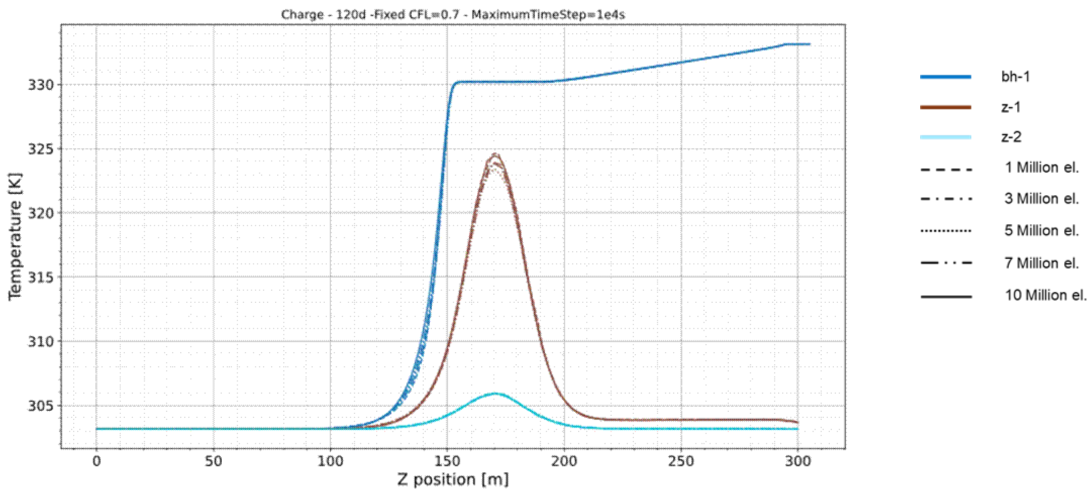

Figure 88: comparison of temperature profiles along bh-1 and z-line monitors, for different meshes, differentiated by number of elements in the grid. Maximum timestep is fixed at $\Delta t_{max} = 10000\ s$.

For a more detailed error analysis, L_2 and L_∞ relative error norms are calculated along z-line monitors.

In Figure 89 and Figure 90, relative error norms are plotted against number of grid elements and time step respectively.

For what concerns spatial discretisation, an acceptable relative error in the order of 10^{-2} is achieved with the grid composed of 5 million elements; further refining of the grid does not yield a significant reduction of relative error, while computational effort in terms of time would be much higher. Therefore, the mesh composed of 5 million elements is chosen for the following analysis of the cylindrical FTES.

Relative error behaves much differently for time discretisation. As shown in Figure 90, relative error is lowest for the smallest time step ($2.7\ hours$) for all z-line monitors. Further reductions in time step size do not result in significant changes of relative error: the maximum error magnitude is for z-1 line monitor, in the order of 10^{-2}.

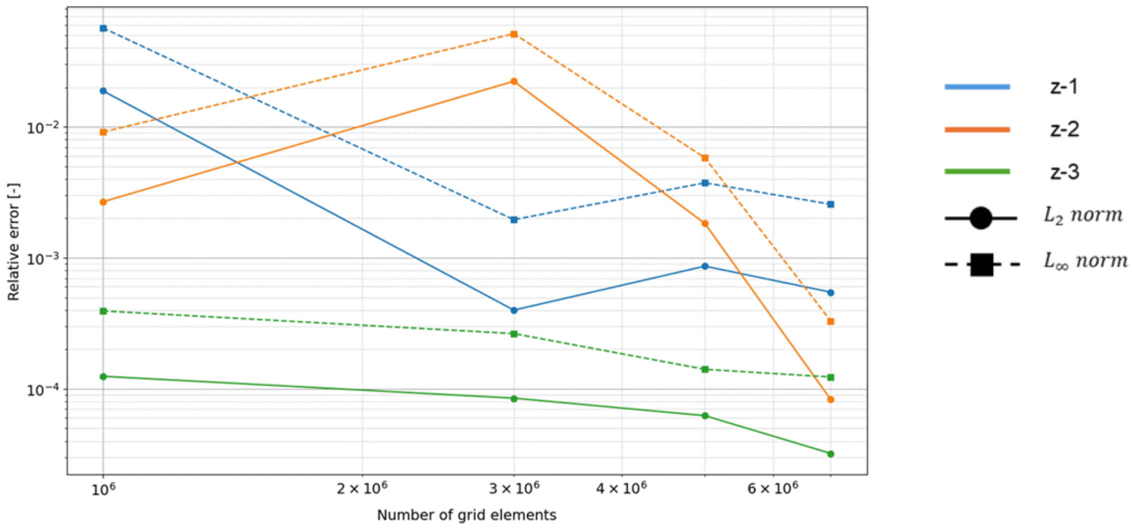

Figure 89: relative error plot of norms L_2 and L_∞ for different spatial discretisation, up to 7 million elements mesh; the 10 million elements grid has been exploited as reference for norms calculation.

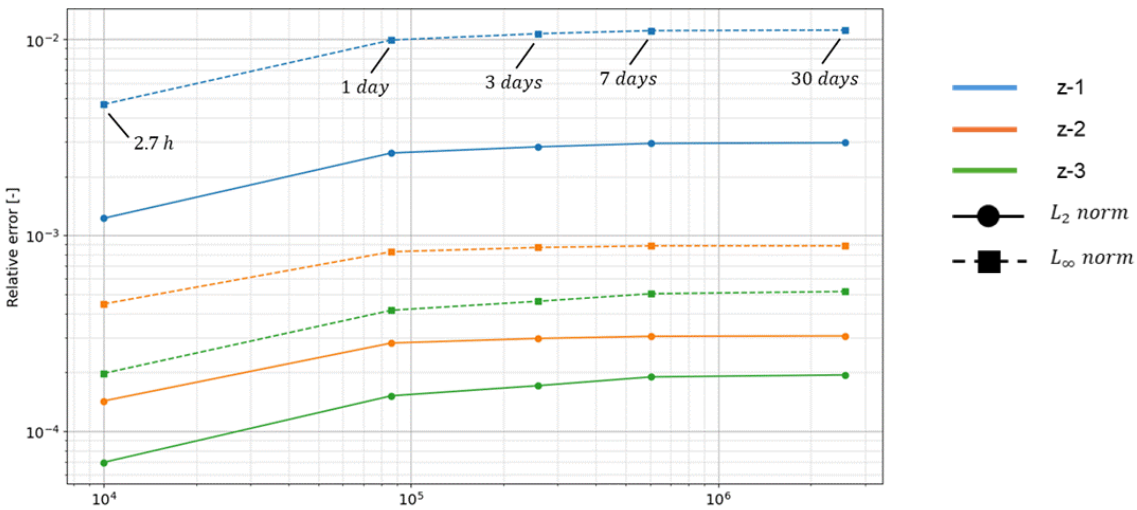

Figure 90: relative error plot of norms L_2 and L_∞ for different time steps, up to 30 days duration; time steps are shown more comprehensively as callouts, while the horizontal axis units are seconds. A time step of $1000\ s$ ($0.27\ h$) has been used as reference for norms calculation.